



Survey Protocol for Geometric SAR Sensor Analysis

DLR-FRM₄SAR-TN-200

Issue 1.4 2018-04-26

ESA Contract No. 4000119113/16/I-EF



University of
Zurich^{UZH}



Authors: Ulrich Balss¹, Christoph Gisinger², Michael Eineder¹,
Helko Breit¹, Adrian Schubert³, David Small³

¹German Aerospace Center, Germany

²Technical University of Munich, Germany

³Remote Sensing Laboratories – University of Zurich, Switzerland

Document Properties

Title	Survey Protocol for Geometric SAR Sensor Analysis
Subject	Subject of this document is a description of all procedures required to analyze, calibrate and validate geometric SAR measurements and to achieve an absolute geometric accuracy of SAR images at the centimeter level. It provides examples and describes standard procedures so that an experienced SAR user can achieve centimeter accuracy calibration in SAR imagery with modern SAR systems such as Sentinel-1 or TerraSAR-X. Demonstration examples for Sentinel-1 and TerraSAR-X are given in chapter 4 of the document.
Institutes	Remote Sensing Technology Institute – German Aerospace Center (DLR-IMF), Chair of Astronomical and Physical Geodesy – Technical University Munich (TUM-APG), Remote Sensing Laboratories – University of Zurich (UZH-RSL)
Compiled by	Ulrich Balss (DLR-IMF)
Authors	Ulrich Balss (DLR-IMF), Christoph Gisinger (TUM-APG), Michael Eineder (DLR-IMF), Helko Breit (DLR-IMF), Adrian Schubert (UZH-RSL), David Small (UZH-RSL)
Checked by	Nuno Miranda (ESA-ERSIN), Adrian Schubert (UZH-RSL), David Small (UZH-RSL)
Released by	Ulrich Balss (DLR-IMF)
Date	2018-04-26
Version	1.4 Revised Version

Document Change Log

<i>Issue</i>	<i>Date</i>	<i>Page(s)</i>	<i>Description of the Change</i>
1.0	2017-08-09	All	First version delivered to ESA.
1.1	2017-12-15	All	<p>Revision and modifications following comments and suggestions by UZH-RSL and ESA-ESRIN.</p> <ul style="list-style-type: none"> • Section 2.2: Update of Figure 2 • Section 2.4: details on Sentinel-1 processing strategy • Section 2.5.2: added discussion on satellite center of mass offset • Section 2.5.3.1: updated discussion on processor conventions • Section 2.5.5: clarification of point target analysis implementation; refinement of Table 2 peak power description. Incidence angle removed from parameter Table 2 • Section 2.6.2: clarification on higher order ionospheric modelling and importance of ionospheric corrections n X-band • Section 2.7: added transformation equation local to global; new reference for Love-numbers • Section 2.7.3: cross reference to newly added discussion on center of mass offset • Chapter 3: clarification of introduction on stacks and image geometries; Figure 28 stable periods marked • Chapter 4: Figures 29 and 30 refined, discussion of processor impact revised; latest Sentinel-1 results added by UZH-RSL, Figure 33 caption expanded; added information of obtaining the Australian CR coordinates; clarification on the selection of CRs for the TerraSAR-X example of the Australian CR array • Appendix 1: details added to the transformation equations. <p>Updates throughout the document on formatting, cross-references and minor corrections</p>
1.2	2018-01-19	61-62, 88-90, 94-96	<p>Revisions made by UZH based on comments/suggestions by DLR.</p> <ul style="list-style-type: none"> • Language editing; • Added recent ALE results by UZH over Australian CR site; • Updated text to take earlier changes into account (e.g. description of Australian CR site removed from this section)
1.3	2018-03-20	106-109	Typos in list of references corrected.
1.4	2018-04-26	17, 100-103, 113	Appendix 2 with sample calculation for Sentinel-1 introduced and referred to in the introduction; corresponding sources added to list of citations

Reference Documents:

- [RD1] Schubert A., Small D., Gisinger C., Balss U., Eineder M., *Corner Reflector Deployment for SAR Geometric Calibration and Performance Assessment*, UZH, TUM, DLR, Technical Note, Ref. UZH-FRM₄SAR-TN-100, July 2017.

Table of Contents

Document Properties	3
Document Change Log	4
List of Acronyms	8
List of Symbols and Variables	10
1. Introduction	11
2. Protocol Description	13
2.1. General Concept.....	13
2.2. Protocol Procedures	14
2.3. Acquisition Geometry and the Concept of Zero Doppler	18
2.4. Geodetic Reference Frames.....	21
2.5. Measurement of SAR Image (Time) Coordinates.....	24
2.5.1. SAR Sensor.....	24
2.5.2. Orbit and Timing on the SAR Platform	28
2.5.3. SAR Processing.....	29
2.5.3.1. Zero Doppler Processing.....	30
2.5.3.2. Stop-Go-Approximation and Related Corrections	31
2.5.3.2.1. Satellite Motion from Pulse Transmission until Echo Reception.....	33
2.5.3.2.2. Satellite Motion during Echo Reception.....	34
2.5.3.2.3. Satellite Motion during Pulse Duration	35
2.5.3.2.4. Increase of Signal Travel Distance.....	37
2.5.3.3. Relativistic Effects	37
2.5.4. Sensor Internal Delays.....	38
2.5.5. Point Target Analysis.....	39
2.6. Signal Path Delay Correction	47
2.6.1. Troposphere	49
2.6.1.1. Path delays based on ECMWF.....	50
2.6.1.2. Path delays based on VMF1	51
2.6.1.3. Path delays based on GNSS	55
2.6.2. Ionosphere	59
2.7. Modelling of Expected Image Coordinates	65
2.7.1. Geodynamics.....	65
2.7.1.1. Solid Earth Tides.....	66
2.7.1.2. Other Geodynamic Effects.....	69
2.7.1.2.1. Ocean loading.....	69
2.7.1.2.2. Atmospheric tidal loading	70
2.7.1.2.3. Pole tides	71
2.7.1.2.4. Ocean pole tide loading	71
2.7.1.2.5. Atmospheric non-tidal loading.....	72
2.7.1.2.6. Secular trends.....	73
2.7.2. Definition of Object Position in ITRF.....	74
2.7.3. Definition of SAR Sensor in ITRF.....	75
2.7.4. Estimation of Expected Radar Times	77
3. Comparison and Analysis	78

4. Examples	85
4.1. Sentinel-1 Examples	85
4.2. TerraSAR-X Examples	91
Appendix 1: Fundamental Geometric Relationships	97
Appendix 2: Sentinel-1 Sample Calculation	100
List of Figures	104
List of Tables	108
References	110

List of Acronyms

A

ALE **Absolute Location Error**
 APG..... Lehrstuhl für **Astronomische und Physikalische Geodäsie**
 (Chair for Astronomical and Physical Geodesy)

C

CODE **Center for Orbit Determination in Europe**
 CR **Corner Reflector**

D

DLR..... **Deutsches Zentrum für Luft- und Raumfahrt** (German Aerospace Center)
 DORIS **Doppler Orbitography and Radio-positioning Integrated by Satellite**

E

ECMWF **European Centre for Medium-Range Weather Forecasts**
 ESA **European Space Agency**
 ESRIN..... **European Space Research Institute**
 EUREF..... **European Reference Network**
 EW **Extended Wide Swath**(S-1 acquisition mode)

F

FFT **Fast Fourier Transform**
 FRM₄SAR..... **Fiducial Reference Measurements for SAR**

G

GA..... **Geoscience Australia**
 GIM **Global Ionospheric Map**
 GNSS **Global Navigation Satellite System**
 GPS..... **Global Positioning System**

H

HS **High Resolution Spotlight** (TSX acquisition mode)

I

ICRF **International Celestial Reference Frame**
 ICRS **International Celestial Reference System**
 IERS **International Earth Rotation and Reference Systems Service**
 IGS **International GNSS Service**
 IMF..... **Institut für Methodik der Fernerkundung** (Remote Sensing Technology Institute)
 IPF..... **Instrument Processing Facility**, i.e. the Sentinel 1 SAR processor
 ITRF_{xx}/ITRF_{20yy} **International Terrestrial Reference Frame 19xx/20yy**
 ITRS **International Terrestrial Reference System**
 IW **Interferometric Wide Swath** (S-1 acquisition mode)

P

PTA..... **Point Target Analysis**

R

RCS **R**adar **C**ross **S**ection
 RSL **R**emote **S**ensing **L**aboratories

S

S-1..... **S**entinel-**1** (mission)
 S-1A/B..... **S**entinel-**1A**/**S**entinel-**1B** (satellites)
 SAR..... **S**ynthetic **A**perture **R**adar
 SC **S**can**SAR** (TSX acquisition mode)
 SET **S**olid **E**arth **T**ide
 SLC **S**ingle **L**ook **C**omplex
 SCR **S**ignal to **C**lutter **R**atio
 SLR **S**atellite **L**aser **R**anging
 SM **S**tripmap(either S-1 or TSX acquisition mode)
 SPD **S**lant **P**ath **D**elay (=extension) in [m]
 SSC **S**ingle **L**ook **S**lant **R**ange **C**omplex
 ST..... **S**taring **S**potlight (TSX acquisition mode)
 SWST..... **S**ampling **W**indow **S**tart **T**ime

T

TMSP **T**erra**SAR-X** **M**ultimode **SAR** **P**rocessor
 TSX **T**erra**SAR-X** (mission)
 TSX-1 **T**erra**SAR-X 1** (satellite)
 TDX-1..... **T**an**DEM-X 1** (satellite)
 TOPS **T**errain **O**bservation with **P**rogressive **S**cans
 TN..... **T**echnical **N**ote
 TUM..... **T**echnische **U**niversität **M**ünchen (Technical University Munich)

U

USNO..... **U**S **N**aval **O**bservatory
 USO **U**ltra **S**table **O**scillator
 UZH **U**niversity of **Z**urich

V

VLBI **V**ery **L**arge **B**aseline **I**nterferometry
 VMF **V**ienna **M**apping **F**unction

W

WS **W**ide **S**can**SAR** (TSX acquisition mode)

Z

ZPD **Z**enit **P**ath **D**elay (=extension) in [m]

List of Symbols and Variables

$\Delta Azimuth$	Azimuth absolute location error
$\Delta Range$	Range absolute location error
t	"Slow" time, generally used in flight (azimuth) direction
τ	"Fast" time, generally used in radar look (range) direction
$(t_{m,CR}, \tau_{m,CR})$	Measured time coordinates of the CR in the SAR image
$(t_{e,CR}, \tau_{e,CR})$	Expected coordinates of the CR in SAR image
v	Scalar velocity of SAR antenna in Earth fixed coordinate system
v_{beam}	Velocity of the zero Doppler plane on ground (beam velocity for Stripmap)
r_0	Range of closest approach
t_0	Time of closest approach to a SAR target
B	Equivalent velocity parameter of SAR in Earth fixed coordinate system
$\gamma_{velocity}$	Relativistic Lorentz factor
τ_{img0}	Zero Doppler travel time of first range sample in SAR image
t_{img0}	Zero Doppler time of first azimuth sample in SAR image
zpd	Zenith path extension ("delay") e.g. of the troposphere in [m]
$\Delta\tau_{SPD}$	Slant path propagation delay time to be subtracted from radar time annotation
Δr_{SPD}	Slant path propagation pseudo excess range to be subtracted
X_{CR}	Corner reflector position vector (regularized = tide-free) in ITRF at dedicated frame epoch, e.g. 1.1.2005
\dot{X}_{ITRF}	Secular linear velocity in ITRF (mostly horizontal tectonics)
\hat{X}_{CR}	Instantaneous corner reflector position vector (with geodynamics, e.g. tides) in ITRF
$X_S(t), \dot{X}_S(t)$	Position and Velocity of Satellite in earth fixed coordinate system ITRF

1. Introduction

The geometric location accuracy of a pixel in a SAR image is the difference between the true position of an object and its position derived from the image, which may be summarized by the term Absolute Location Error (ALE). It can be specified in 3-D object space or in the 2-D image geometry of the SAR system. The specified numbers for different SAR systems have improved considerably since the times of ERS-1, not only because of improved technology, but mainly due to improvements in SAR processing algorithms, calibration algorithms, and recently, geodetic correction techniques. While the first ERS-1 products had a specified accuracy on the order of hundreds of meters [1], Sentinel-1 Stripmap products have a specified accuracy of 2.5 m (SLC, NRT orbit) [2] in the image coordinate system. This accuracy, on the order of the single-look SAR pixel resolution, is today a typical specification and it is good enough to support most applications of SAR imagery. However, it has been shown [3][4][5][6] that SAR can do much better if properly processed, calibrated and corrected for well-known effects such as wave propagation and earth dynamics, as it is done in geodesy. Then, if SAR systems are handled like GNSS, a whole new range of geodetic applications become feasible.

This technical note describes a protocol to calibrate and validate SAR systems with the goal to achieve low centimeter accuracy. The protocol involves artificial targets with well-known reflection properties, preferably point-like targets, which are deployed as calibration (or validation) targets, preferably at well-known geodetic reference sites. The most common types of point-like radar targets are (passive) corner reflectors (CRs) and (active) transponders. Appreciated features of CRs are that they are purely passive elements that neither need any power supply nor introduce any (possibly unknown) additional delays to the signal round trip time. The position of their phase center is derivable purely by geometric considerations. However, the protocol is – with little extensions – as well applicable to transponders, provided that their technical parameters like the position of the (virtual) phase center or the internal delay time are precisely characterized.

Selecting appropriate point targets such as trihedral CRs and how to establish a dedicated SAR test site is not covered by this document. These topics are described in detail in the document *Corner Reflector Deployment for SAR Geometric Calibration and Performance Assessment* [RD1], generated under the same ESA contract. We assume that the targets have been firmly installed and correctly aligned, and that their reference coordinates have been determined in the global International Terrestrial Reference Frame (ITRF). The sites may be summarized in *reference station protocols* as shown in [RD1], Figure 14, which along with the SAR scenes provide the fundamental input for the calibration and validation procedure.

The remainder of this document is structured as follows. Chapter 2 will first introduce the protocol and then describe all the technical details to implement the protocol. Chapter 3 discusses the methods for generating and analyzing ALE results. Chapter 4 demonstrates the validity of the protocol by applying it to TerraSAR-X and Sentinel-1 at different test sites.

This document is written within the framework of the FRM₄SAR (Fiducial Reference Measurements for SAR) project, induced and founded by ESA-ESRIN (ESA Contract No. 4000119113/16/I-EF). The document is strongly related to the document [RD₁], generated under the same contract.

2. Protocol Description

The purpose of the proposed protocol is to provide a step-by-step procedure allowing stakeholders to perform an accurate geometric characterization of a SAR satellite mission (with emphasis on Sentinel-1) and to verify its validity. The results of this procedure shall be generated and documented in a consistent way, so that they can be cross-compared between different ground sites, between different missions and used for long term monitoring.

2.1. General Concept

The basic idea of the proposed protocol is that CRs whose position is precisely known in 3-D space can be uniquely and accurately projected into the 2-D image space of the SAR as sketched in Figure 1. The image space is spanned by the fast time τ , i.e. the two-way round trip time of the radar signal, and the slow time t along the sensor's movement path, which may be defined as the time of closest approach. The difference vector between the measured position $(t_{m,CR}, \tau_{m,CR})$ of the CR in the SAR image and its expected position $(t_{e,CR}, \tau_{e,CR})$ is the location error in the image (time) coordinate system which can be converted to an equivalent absolute location error (ALE) in units of lengths. While this straightforward procedure looks simple on the first glance, its realization requires meticulous care during all processing steps if centimeter or even millimeter accuracy is the goal. Therefore, the key steps and the possible pitfalls are described in this document.

By performing many of such measurements in time (multiple images), in space (CRs at different image positions) and with different imaging conditions (polarization, incidence angle, ascending/descending orbits), the SAR imaging system can be very accurately geometrically calibrated and verified. Moreover, error estimates can be given and residual systematic errors can be characterized.

2.2. Protocol Procedures

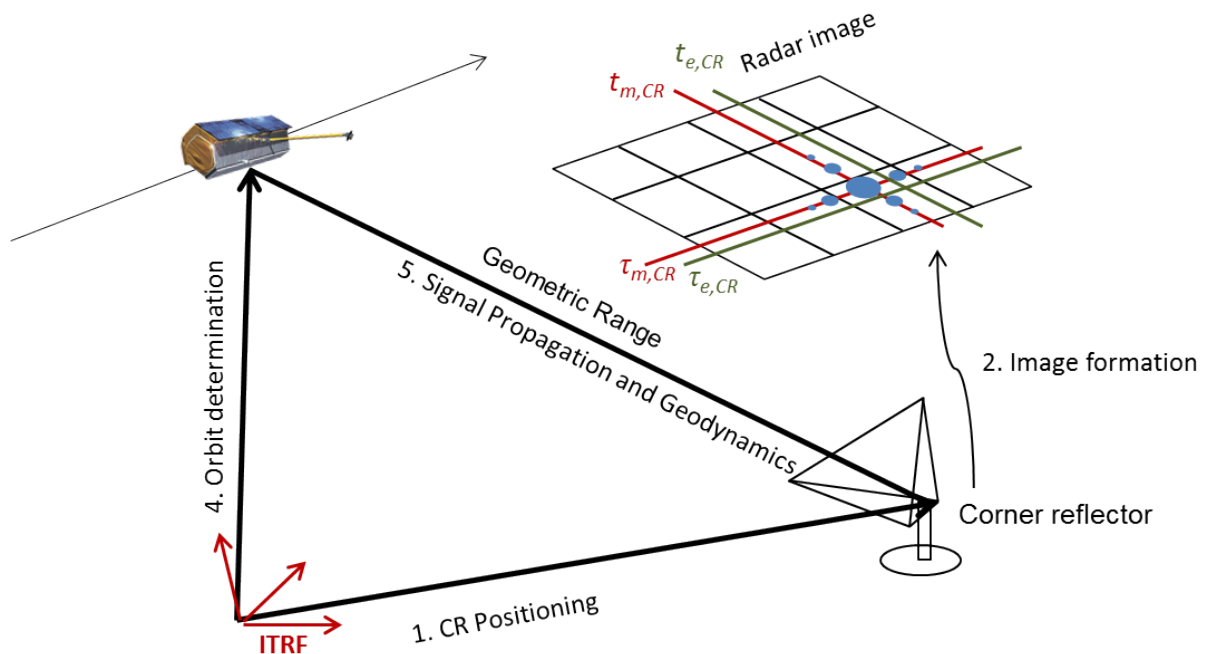


Figure 1: Brief sketch of measurement arrangement and procedures

In the following, we provide a short overview of the defined protocol, while the technical and algorithmic details are described in the subsequent chapters. Figure 2 shows an overview of the protocol procedures.

- a) Select test site and CRs: A geologically stable test site which allows for the survey of global reference coordinates shall be selected. Geodetic fundamental stations with installations of the global geodetic observing system (GNSS, VLBI, SLR, DORIS) are ideal for this purpose, but other test sites may be established at suitable locations and surveyed by GNSS; see details in [RD1]. For the placement of the CRs, locations with low background backscatter shall be selected, e.g. concrete or grass. Other strongly reflecting objects should be avoided in the vicinity of about 30-times the SAR pixel resolution as this is a typical window size for the point target analysis (see 2.5.5). The size of the reflectors shall be selected based on the SAR system parameters and the pursued accuracy as described in [RD1].

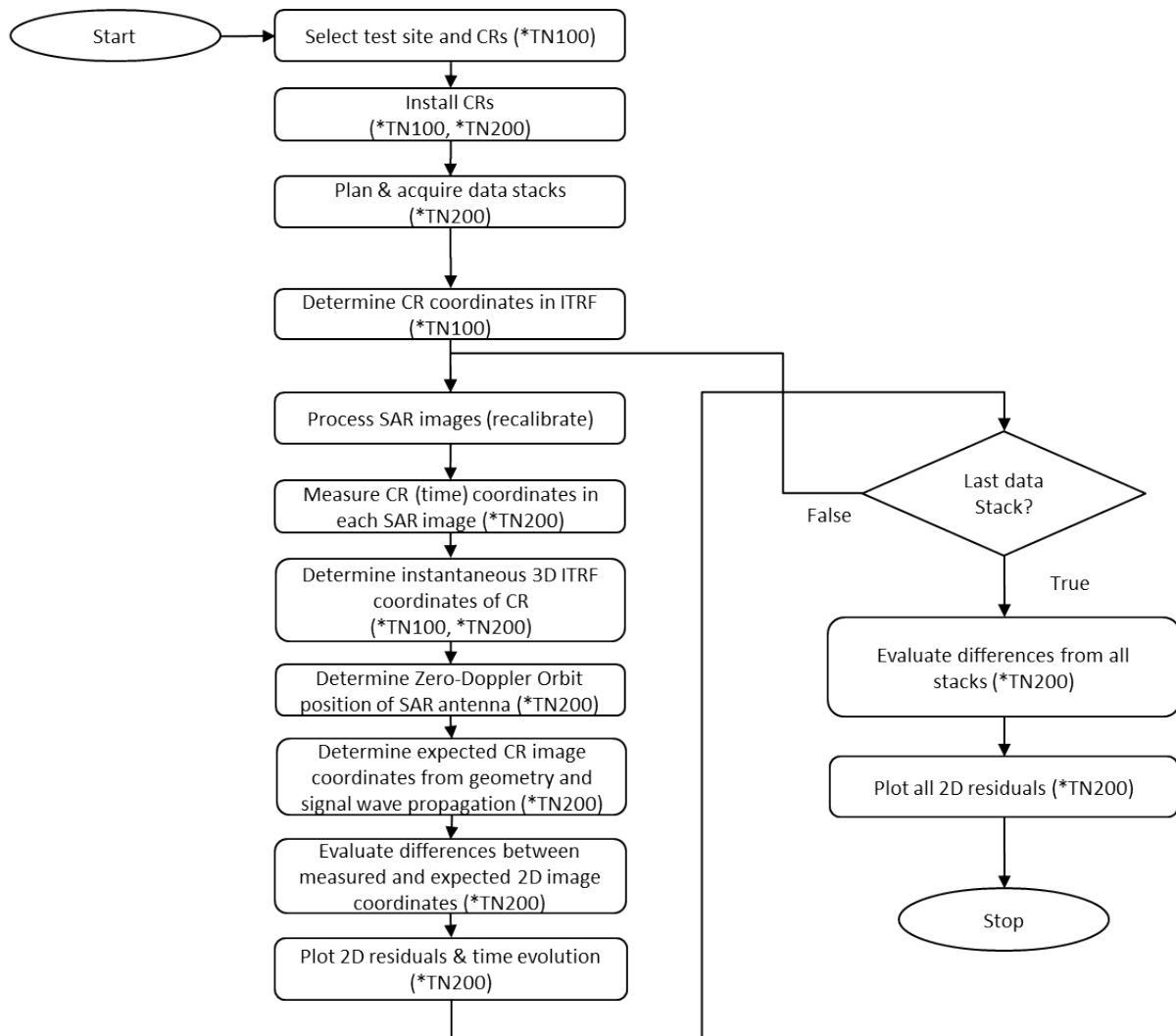


Figure 2: Flow chart of the protocol described in this note. Documents *TN100 and *TN200 refer to [RD1] and this document, respectively.

- b) Install CRs as described in [RD1].
- c) Plan and acquire as many data stacks as feasible and necessary. Each data stack shall capture the CRs under different incidence angles and, possibly different imaging parameters such as polarization, resolution, SAR-mode etc. At least 10 sequential observations are recommended to determine the mean offset with an accuracy of $1/3$ rd of the single observation standard deviation (100 for $1/10^{\text{th}}$). More observations (20-60) are strongly recommended to determine more reliable error standard deviations or to discover obvious outliers and deal with long term trends in the observations.

- d) Measure and determine the CRs' reference coordinates X_{CR} in ITRF as described in [RD1] and in this document. Repeat the measurements at least once after the campaign to verify the mechanical stability of the arrangement.

For each acquired data stack the following steps shall be performed separately:

- e) Process each SAR image acquired at time t_{img0} with a consistent SAR processor (constant version and processing parameters) as described in section 2.5.3. Sensor/mode-specific calibrations or corrections of factory-calibration may be required at this stage, e.g. the removal of a standard atmosphere annotated in the product or a pseudo electronic delay that also contains excess atmospheric path delays. The goal is to calibrate the SAR as a true time measurement system which is exactly synchronized with the orbit. If such parameters are not known a-priori, they will show up as biases during the final evaluation stage. The topic will be discussed for Sentinel-1 in section 4.1
- f) Determine the SAR image (time) coordinates $(t_{m,CR}, \tau_{m,CR})$ of the CR by point target analysis as described in section 2.5.5.
- g) Calculate the instantaneous position $\hat{X}_{CR}(t_{img0})$ of the CR at the time of SAR imaging in ITRF as described in section 2.7.2.
- h) Calculate the expected geometric azimuth position $\hat{X}_s(t_0)$ of the SAR antenna phase center (not the satellite center of mass) in Zero-Doppler (space) coordinates and the range distance $r_0 = |\hat{X}_{CR}(t_{img0}) - \hat{X}_s(t_0)|$ between SAR antenna and CR.
- i) Convert Zero-Doppler azimuth position $\hat{X}_s(t_0)$ and range distance r_0 into the SAR time coordinates $(t_{e,CR}, \tau_{e,CR})$ as described in section 2.7.4.
- j) Evaluate the residuals $(t_{m,CR} - t_{e,CR}, \tau_{m,CR} - \tau_{e,CR})$ between measured and expected coordinates of the CR in the image taking into account the wave propagation corrections. Convert the times to distances using vacuum¹ light velocity and the speed of the footprint as described in chapter 3.
- k) For the evaluation:
- Calculate mean and standard deviation of range and azimuth residuals.
 - Plot the range residuals versus the azimuth residuals in a reasonable scale as shown in ch. 4.
 - Plot the time series of range and azimuth residuals.

Finally, for all stacks together:

¹ Assuming vacuum velocity is sufficiently accurate for small distances.

- l) Calculate mean and standard deviation of range and azimuth residuals and their estimation errors.
- m) Plot the range deviation versus the azimuth deviation in a reasonable scale.
- n) For system calibration: Determine or refine the SAR system calibration parameters removed from the products in step (e) (i.e. internal electronic delays and azimuth timing offsets) from the residual differences. Ideally these are independent of instrument or acquisition configuration like incidence angles, beams, polarizations, etc. If this is not achieved, they might represent processing artifacts or instrument characterization errors.

Note that the above protocol is following the physics and the logic of the SAR measurement process. It is only one variant of many. For example, one could also transform SAR range times to range distances using vacuum light velocity and then correct with scaled atmospheric zenith delays, or, transform geodynamics (e.g. solid earth tides) to SAR range times and correct for it.

For a consistent comparison of results with other systems and procedures we recommend the proposed protocol. A detailed step-by-step example for above procedure based on Sentinel-1 can be found in the Appendix 2.

2.3. Acquisition Geometry and the Concept of Zero Doppler

The most appropriate coordinate system for SAR is the zero Doppler geometry which is shortly introduced in the following.

During the SAR data acquisition the distance between sensor and a target on ground decreases till the instant of closest approach t_0 and increases afterwards. Consequently, the signal travel time decreases from echo event to echo event while the sensor is approaching, and increases when the sensor is receding. The time dependent range vector $\vec{r}(t)$ is obtained as the difference of the corner reflector coordinates $\hat{X}_{CR}(t)$ and the satellite position $X_S(t)$. Figure 3 sketches the acquisition geometry during a single SAR pass.

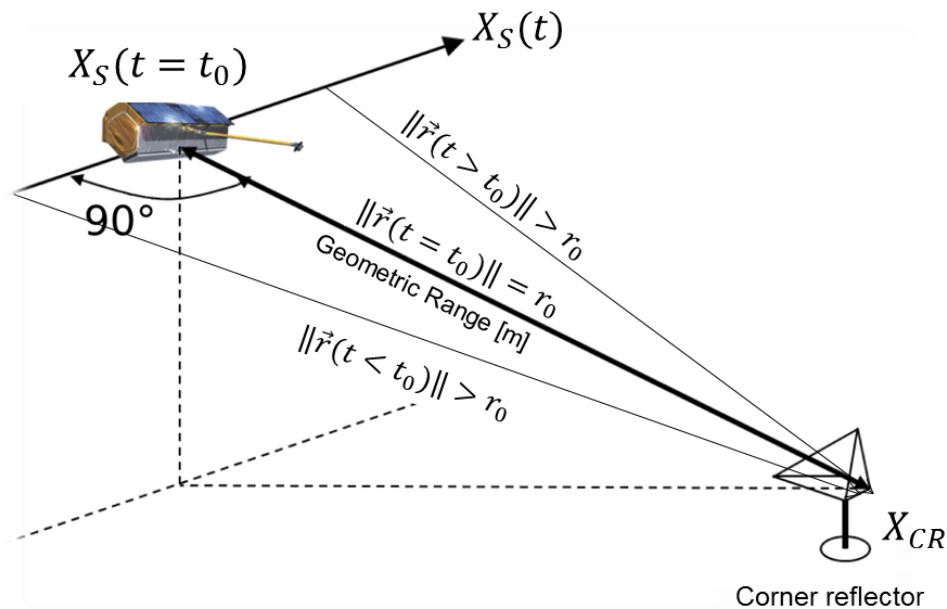


Figure 3: SAR acquisition geometry. The distance $r = \|\vec{r}\|$ between sensor and target is minimum at $t=t_0$. At this instant, the range vector \vec{r} is perpendicular to the flight path.

Approximating the sensor's flight path by a straight line and assuming constant velocity, the temporal progression of the distance $r(t)$ between sensor and target, the so-called range history, can be approximated in first order by

$$r(t) = \sqrt{r_0^2 + v^2 \cdot (t - t_0)^2} \quad \text{Eq. 1}$$

where t_0 and r_0 denote the instant of closest approach and the distance at this instant, respectively. v is the velocity of the sensor. Figure 4 illustrates the functional relation described by Eq. 1 for different targets at different ranges.

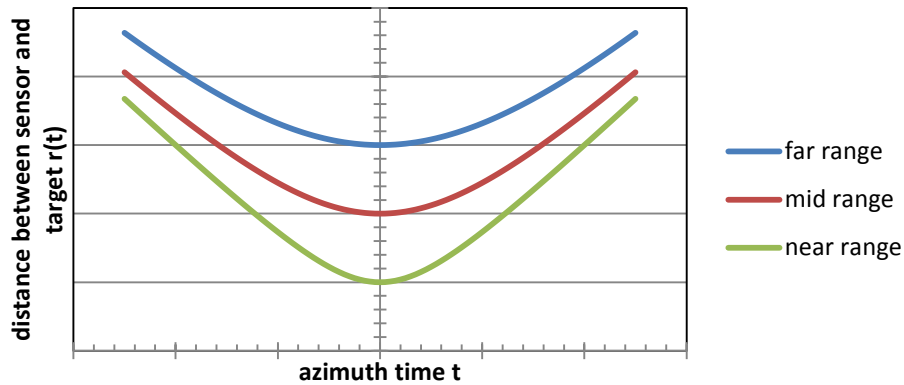


Figure 4: Range history, i.e. temporal progression of the distance between sensor and target during data take acquisition. Plotted for three targets: at near, mid and far range (schematic diagram).

An accelerated motion, as it results in particular for a curved flight path like a satellite orbit, can be considered by the modified, more exact formula

$$r(t) = \sqrt{r_0^2 + B \cdot (t - t_0)^2}. \quad \text{Eq. 2}$$

where the factor v^2 of Eq. 1 is replaced by the so-called equivalent velocity parameter

$$B = \|\dot{\vec{r}}\|^2 - \vec{r}\ddot{\vec{r}} \quad \text{Eq. 3}$$

with $\dot{\vec{r}}$ and $\ddot{\vec{r}}$ being the range velocity and acceleration vector, respectively. For a static CR this is equivalent to the satellites motion and acceleration vector. Using this parameterization is state of the art in current SAR processors.

A consequence of the varying distance between sensor and target is a time variant Doppler shift of the echoes in the spectral domain. At the instant of closest approach, the velocity vector of the sensor is perpendicular to the line of sight between sensor and target and consequently, the Doppler shift at this instant is zero.

$$\frac{\dot{\vec{r}}(t_0) \cdot \vec{r}(t_0)}{\|\dot{\vec{r}}(t_0)\| \cdot \|\vec{r}(t_0)\|} = 0 \quad \text{Eq. 4}$$

For this reason, the terms *closest approach* and *zero Doppler* refer to the same constellation of sensor and target and are synonymous in this context. Consequently Eq. 4 is called *zero Doppler equation* [7].

The range time (signal round trip time), compensated for sensor internal delay and for signal propagation delays (see section 2.6), and the distance between sensor and target are interconnected by

factor $c/2$ where c stands for the vacuum velocity of light. Thus, the possible target position is reduced to the surface of a sphere

$$r = \frac{c}{2} \tau \quad \text{Eq. 5}$$

centered on the sensor. For this simplified geometry we ignore spatial variations of signal wave propagation which might deform the sphere. Merging the information from both equations the intersection of zero Doppler plane and range sphere results in a circle which is oriented in space perpendicular to the satellite's flight path (see Figure 5).

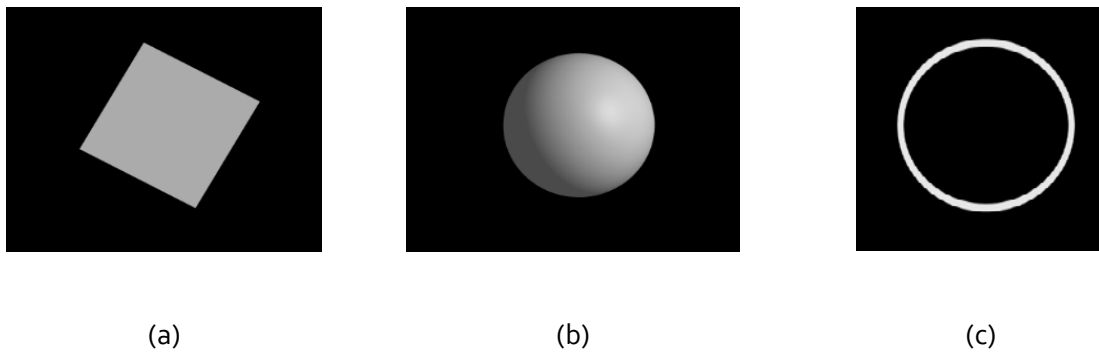


Figure 5: Information on the location of a point scatterer, derivable from radar coordinates. a: Azimuth defines the zero Doppler plane. b: Range defines the surface of a sphere centered on the sensor. c: The intersection of both surfaces results in a circle line which is perpendicularly oriented to the satellite's flight path in space.

Eq. 4 and Eq. 5 are the basis for the transformation between radar and spatial coordinates. However, as radar time coordinates are 2-D, there remains a degree of freedom (because of the inaccessible cross-range coordinate) when transforming radar times to spatial coordinates. In order to solve this degree of freedom, additional information, e.g. a reference surface (ellipsoid, digital terrain model), is required. In contrast, the transformation from spatial to radar coordinates is unique. Therefore, this transformation direction is preferable for the verification of the localization accuracy of a SAR system against an independent reference (e.g. GNSS) and compare measured and expected coordinates in radar coordinate representation. Because azimuth time t occurs just as parameter of the orbit interpolation in both equations, a closed solution of the equation system for t and τ is impossible. Iterative methods (e.g. Gauss-Newton interpolation) are necessary to determine t from Eq. 4. Once t is numerically determined in this way, τ results immediately from Eq. 5.

For the purpose of ALE calculation the zero-Doppler beam velocity v_{beam} is required. It can be calculated by solving the zero-Doppler equations for one point on ground and for another one separated by a small time interval (at the same range).

2.4. Geodetic Reference Frames

In order to compare the imaged CR positions with the predicted image location based on the surveyed coordinates and the annotated orbit product, all coordinates have to refer to the same global reference frame. In this section, we briefly discuss different frames that are involved when applying the ALE protocol, and we clarify the importance of using the International Terrestrial Reference Frame (ITRF) as the fundamental reference in the processing.

For SAR satellites orbiting the Earth, two basic frames are involved: a quasi-inertial reference frame for the orbit determination and a reference frame attached to the rotating Earth to define the ground position. In addition, one requires parameters to perform the transformation between these two frames. Only then the fundamental equations connecting a satellite state vector (position & velocity) with terrestrial station coordinates through geometric observations (ranges, range rates, angles, ...) can be stated in the terrestrial frame, e.g. see the range-Doppler equations in sections 2.3.

Establishing these frames along with the transformation parameters is the long-standing task of geodetic, geophysical and astronomical associations, and their collaborative efforts are documented in technical notes issued by the International Earth Rotation and Reference Systems Service (IERS), namely the IERS conventions (latest version 2010) [8]. A fundamental concept for establishing the frames is the idea of *systems* and *frames*. The *system* holds the theoretical definitions and the conventions (origin definition, axes definition, numerical standards ...) whereas the *frame* is the physical realization of such a definition by sets of coordinates which have to be inferred from observations. The realization is updated on a regular basis to take into account the ever growing number of observation as well as the potential refinements in the processing strategies. The consistency is maintained throughout all realizations, and the transformation between different realizations is readily possible because of their common system definition and the full re-processing of all data when generating a new solution.

Currently, the most precise realizations of the two Earth related frames are the International Terrestrial Reference Frame (ITRF), release 2014 [33], and the International Celestial Reference Frame (ICRF), release ICRF2 [34]. The former consists of a global set of regularized² Cartesian station coordinates, while the latter is defined through celestial coordinates (declination, right ascension) of extragalactic radio sources. Note that the optical realization of the ICRF is given through the alignment of

² The term “regularized” refers to coordinates of a hypothetical mean crust, which are reduced for periodic geodynamic deformations. One may also call them “tide-free” but this is somewhat incomplete, see details in section 2.7.1)

fundamental star catalogues. According to the discussion stated above, the theoretical definitions are specified in the ITRS and the ICRS, respectively [8].

As a result of this discussion and regarding the application of SAR ALE assessment, two aspects are vital: first the orbit determination has to comply with the specifications of the ICRS/ITRS, in particular the transformation to the Earth fixed frame defined by the Earth Orientation Parameters (EOPs), which allows for ITRF-based state vectors annotated to a SAR product. Second, the CR reference coordinates have to be determined and stated in the ITRF to make use of its conventions to define the instantaneous position of the CR for the very epoch of the SAR observations. How to measure the CR and process the survey for ITRF reference coordinates, i.e. position, linear displacement and frame epoch, was already covered in [RD1].

The subject of precise orbit determination (POD) is out of scope of this document, but some important elements have to be addressed here. When determined by star trackers, the attitude is bound to the star catalogues and one has to ensure that the final attitude product complies with the ICRF. Also the employed force models and the a-priori data sets (e.g. GNSS orbits, GNSS clocks) have to match the ICRF. The required data depend on the strategy of orbit determination: dynamic, kinematic, or reduced-dynamic. For purely kinematic or reduced-dynamic orbits using geodetic observation techniques (GNSS, Doppler Orbitography and Radiopositioning Integrated by Satellite - DORIS, Satellite Laser Ranging - SLR), it is advised to use the products of the corresponding geodetic services (IGS³, International Laser Ranging Service – ILRS⁴, International DORIS Service - IDS⁵), which contribute to the ITRF solution and the EOPs, and thus ensure the best possible consistency between ICRF and ITRF. The transformation based on the EOPs is covered in chapter 5 of the IERS convention [8]. Two SAR missions for which the POD is carried out according to the stated methods are Sentinel-1 and TerraSAR-X.

For the TerraSAR-X mission, the latest details on the reduced-dynamic orbit determination using the on-board GPS are given in [35]. The operational science orbit product and thus the state vectors distributed with the TerraSAR-X SAR products have a qualified 3-D accuracy of 4.2 cm, but recent SLR analysis and our practical ALE tests indicate an even better accuracy around 1-2 cm [35]. Regarding Sentinel-1, the standards used in orbit determination and first results of the orbit quality are published in [36]. Unfortunately there is no possibility for external validation by e.g. SLR, but the cross comparison of different analysis centers (ACs) confirms that the goal of 5 cm RMS was achieved. Further refinements are in discussion, but for now one has to assume the orbit limit in the Sentinel-1 ALE

³ <http://www.igs.org/>

⁴ <https://ilrs.cddis.eosdis.nasa.gov/>

⁵ <https://ids-doris.org/>

analysis to be at a level of 4-5 cm when using the Precise Orbit Ephemeris auxiliary product⁶. Due to the systematic processing strategy in less than 24h (FAST-24h), the precise orbit product is not included in the S1 image products and becomes available some 3-weeks after the product acquisition. Most of the S-1 FAST-24h products are generated using the restituted orbit achieving an accuracy of 5cm (2D RMS)

In summary, the SAR ALE analysis should be based on the ICRF and ITRF. This involves the task of orbit determination and its post processing for the ITRF to be applicable to the SAR product. Hence, we consider this the responsibility of the SAR satellite mission provider. For the user conducting the ALE processing, consistency is maintained by properly determining the CR reference in the ITRF, as well as by considering the geodynamic effects according to IERS standards, see section 2.7.1. The geodynamic effects are addressed in the following sections. Complying with the standards ensures the correct prediction of range and azimuth from the range-Doppler equations, as well as a valid comparison with the observed range and azimuth stemming from the SAR image.

⁶ https://qc.sentinel1.eo.esa.int/aux_poeorb/

2.5. Measurement of SAR Image (Time) Coordinates

This section describes the measurement process of SAR image time coordinates. It points out the crucial factors influencing the accuracy of the resulting time coordinates. Therefore we look into the SAR image acquisition, the image generation process (SAR focusing), and explain the subsequent point target analysis (PTA), where we extract time coordinates of corner reflectors from a SAR image

The first subsection introduces the SAR sensor concept. It briefly explains the prominent SAR imaging modes, and stresses the importance of precise timing for the measurement process. The next subsection addresses the orbit determination and orbit accuracy of the SAR platform. This is followed by a detailed subsection on SAR processing which covers the aspects of image time annotation and concepts to overcome the effects of widely employed processor approximations, in particular the so called Stop-Go-Approximation. Furthermore, we discuss the limits of direct use of the annotated instrument delays. In the final subsection our approach for point target analysis at image sub-pixel level is presented which generates the image coordinates times $t_{m,CR}$ and $\tau_{m,CR}$.

2.5.1. SAR Sensor

Synthetic Aperture Radar (SAR) is an imaging method based on a side looking radar system. While the sensor, mounted on a satellite or aircraft, is passing the area of interest, it scans the area by short-period radar pulses. A finally processed SAR SLC/SSC image with columns and rows oriented along and across the flight track may mislead to the assumption that the underlying data acquisition was performed by a sensor with an ability to receive backscatter signals as a function of two independent variables, range r (across track) and time t (along track), respectively. In reality, the SAR instrument continuously transmits short pulses and receives echoes in between. The received signal is registered as a function a single variable, i.e. the time t , as depicted in Figure 6.

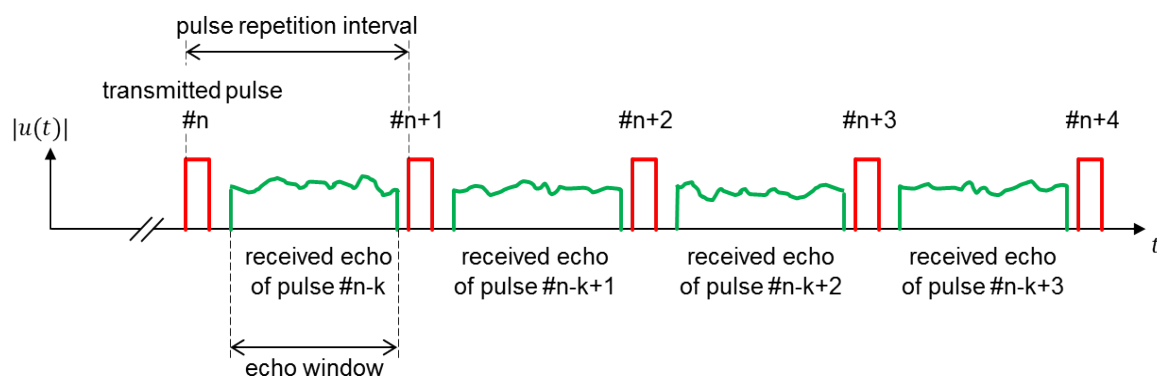


Figure 6: A SAR instrument registers radar echoes as a function of time t . The offset k indicates the number of travelling pulses accounting for the fact, that the signal round trip delay is larger than a pulse repetition interval.

Only in the course of the subsequent SAR processing a second time axis, range time τ , is introduced, leading to a 2-D representation of the SAR signal. Therefore range time τ and azimuth time t , also termed fast time and slow time, respectively, are directly coupled and form the axes of the (t, τ) coordinate system. They are neither independent nor orthogonal to each other, as depicted in Figure 7. Ignoring this interrelation is equivalent to adopting the Stop-Go-Approximation during SAR processing which is further explained in 2.5.3.2. In this case, the generated SAR images are geometrically distorted w.r.t. the range Doppler equation, Eq. 4.

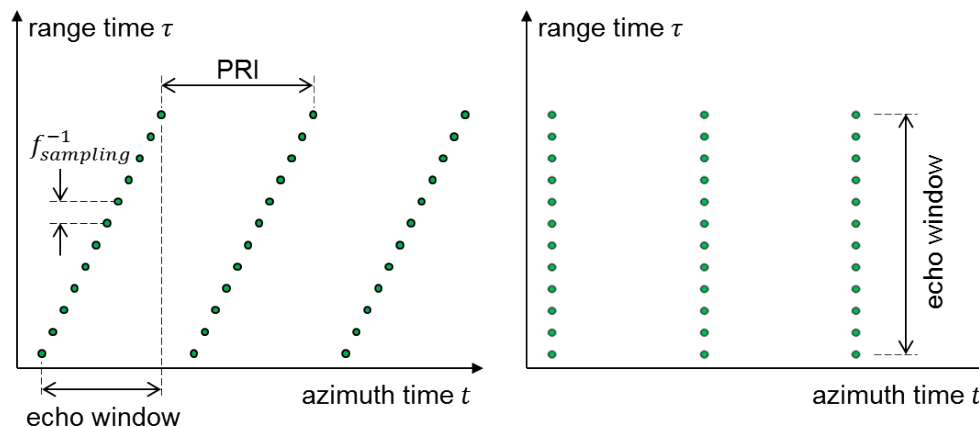


Figure 7: The plot on the left depicts the true timing of the received SAR echo sample matrix, while the plot on the right illustrates the timing as it is assumed by the Stop-Go-Approximation. This mismatch directly affects the time coordinates of the final SAR image.

A SAR processor which takes into account the true coupled timing annotation of the received SAR signal thus overcoming the Stop-Go-Assumption and providing SAR images in a final (t, τ) coordinate system. Only in this case, the τ is fully decoupled and directly related to a range axis orthogonal to the flight path according to the range Doppler equation, Eq. 4. Still, the transition from a measured signal round trip delay τ to a range measurement r requires further corrections like the path delay in atmosphere pointed out in section 2.6.

Due to the azimuth beam width of the SAR antenna in flight direction, a target on ground is illuminated by a sequence of pulses. As a consequence the response of one target is accordingly spread over a sequence of received echoes whereas a single echo contains the energy contributions of several targets. By means of signal processing (SAR focusing), synthetic apertures are formed in the direction of the sensor's flight pass and thus, the radar echoes received from different objects on ground can be separated with significantly higher resolution than possible using the natural resolution. The latter is defined by the azimuth beam width of the antenna, which is inversely proportional to the antenna length. The attainable resolution of space-borne SAR varies from several meters down to sub-meter level, depending on system parameters like antenna length, radar bandwidth, sampling rate and imaging mode. Accounting for the geometrical properties of the different imaging modes in the SAR processor is crucial for high-quality SAR calibration. Common imaging modes used by modern SAR sensors are:

- **Stripmap** is the most basic imaging mode of SAR. The radar beam is fixed and oriented perpendicular to flight direction, see Figure 8. A degree of freedom exists in the choice of the radar beam elevation pointing. In current SAR missions it is selected at the start of a datatake and is kept constant throughout. The antenna elevation beam width and the elevation pointing define the illuminated ground swath and the receiver timings are adjusted to receive the echoes from this swath.
- A better resolution in azimuth direction is obtained in **Spotlight** mode. During datatake acquisition, the radar beam is panned w.r.t. azimuth direction continuously or stepwise from forward to backward looking, cf. Figure 8. Consequently, an increased synthetic aperture time and azimuth resolution results – as the aperture time rules the azimuth resolution. For TerraSAR-X the Spotlight mode exists in different “flavors”. In the **Staring Spotlight** mode, the beam center almost follows a fixed point on ground while the sensor overflies the scene. In this way, the aperture time of the targets in the scene equals the entire datatake duration leading to the best possible resolution, however at the cost of scene extension. In the **High Resolution** and **Sliding Spotlight** modes the beam is steered slower from forward to backward. Thus, the beam slides over the targets reducing their illumination time compared to a staring beam. This steering law results in a resolution in between Stripmap and Staring Spotlight, and in a scene extent superior to Staring Spotlight.
- The **ScanSAR** mode is designed for scanning wide image swathes at the price of a lower azimuth resolution. This is realized by periodically leaping between several (maybe 3, 4, 5 or 6⁷) elevation beams which illuminate adjacent sub-swathes on ground. In consequence, each sub-swath is illuminated by a sequence of short bursts, and each of the bursts is a sequence of sequential pulses. In order to save illumination time for the other elevation beams, the targets in a single burst are illuminated for a much shorter time than the geometrically given maximum aperture time. A side effect of this procedure is that each target is illuminated by another part of the entire antenna diagram. Therefore, the Doppler centroid of the targets varies from lower frequencies at early azimuth to higher frequencies at late azimuth. The choice of an adequate burst repetition rate guarantees continuity between the consecutive bursts of same elevation beam, i.e. the late azimuth edge of one burst fits (ideally with some small overlap) to the early azimuth edge of its successor. The totality of all focused bursts of all beams ensures continuous coverage, as shown in Figure 8.

⁷ These are typical values for Sentinel-1 (IW: 3 beams; EW: 5 beams) and TerraSAR-X (SC: 4 beams; WS: 6 beams)

- In a sense, the **TOPS** mode can be considered as an improved variant of ScanSAR. Within each burst, an azimuth steering from backward to forward looking results in a more homogeneous radiometry of the acquired SAR image. While the geometric features of ScanSAR and TOPS are comparable, i.e. both modes are burst modes with a swath width superior to Stripmap and an azimuth resolution inferior to Stripmap. There are differences in the spectral properties of the focused targets. In particular, the Doppler centroid in TOPS varies to a much larger amount from early to late azimuth targets of a burst.

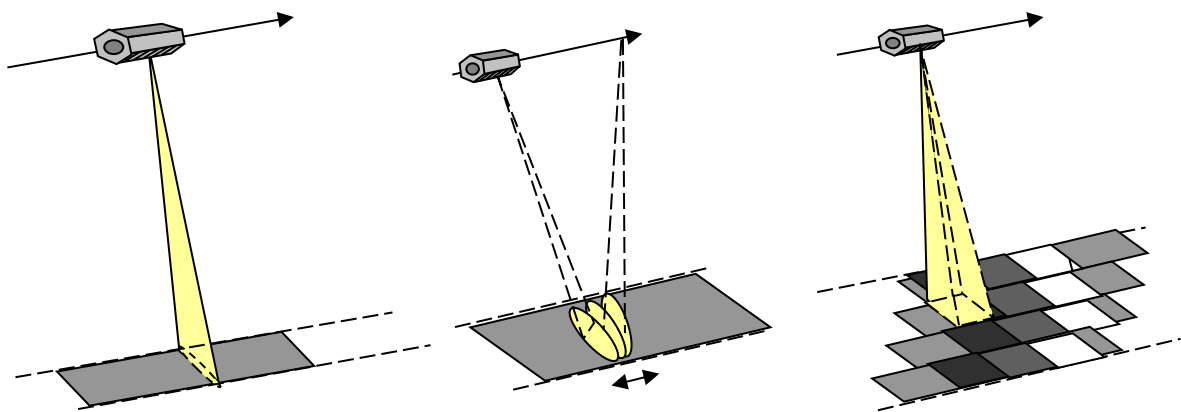


Figure 8: Schematic sketch of the TerraSAR-X imaging modes Stripmap, Spotlight and ScanSAR [9].

A consequence of the measurement principle of SAR - measuring positions indirectly by two time coordinates - is that a high timing accuracy is essential for precise location measurements. In the process, the challenges of precise range and azimuth timing refer to different aspects. In range, very short time intervals have to be measured based on an ultra-stable oscillator (USO) of well-characterized clock-rate. In the case of the TerraSAR-X mission, the oscillator frequency is regularly monitored by comparing it against an even more precise external reference (GPS) during very long system datatakes (each lasting several minutes). The ratio of both measurements of the datatake duration yields a correction factor for the nominal USO frequency annotated in the product (see [42] for algorithmic details).

In contrast to the relative range timing, azimuth localization requires precise knowledge of the absolute position (inferred from onboard GPS) of SAR echo recordings (tagged with SAR time). Thus, thorough referencing of the SAR instrument time with the GPS time is essential. Typically this can be accomplished by time correlation elements consisting of a pair of time tags of a simultaneous event and, possibly a frequency (scaling) correction factor. Furthermore, the precise timing information shall be actually forwarded throughout the entire process of datatake acquisition and processing. In this regard, the parsimonious quantization accuracy of timing annotations in echo data packages of former and ongoing SAR missions (including Sentinel-1 and TerraSAR-X) is a bottleneck to be avoided in future SAR missions. In the case of TerraSAR-X and Sentinel-1, the annotated azimuth time is quantized in steps of about 20 microseconds. However, the satellite moves by approximately 13 cen-

timeters during this time interval⁸. Future missions should be 100 times more accurate, i.e. measure time correlation with 200 nanoseconds, to be on the safe side.

A crucial point is to correctly define the reference position for the range and azimuth measurements on board. Ideally it is a well-defined SAR antenna phase center. Many current space-borne SAR sensors like Sentinel-1, TerraSAR-X, Radarsat-2, Cosmo SkyMED, ALOS-2 use phased array antennas. With this class of SAR antennas, a multitude of antenna beams in azimuth and elevation is realizable by electronic antenna steering. However, this flexibility challenges the definition of a fixed phase center for the entire antenna. In the end, a slight beam-dependent offset of the assumed antenna phase center from the geometrical centroid of the antenna surface remains and is one of several residual effects to be quantified by geometric calibration. The sum of these residual effects in azimuth and range can be characterized in two calibration constants, one per dimension (see section 2.5.4 for more details).

2.5.2. Orbit and Timing on the SAR Platform

Synthetic Aperture Radar focusing and accurate pixel geolocation requires by definition the accurate knowledge of the satellite flight-track. Early systems like ERS-1/2 used the S-band telemetry signals for ranging and Doppler tracking. Together with radar altimeter data this provides good boundary conditions for an orbit determination which is good enough for SAR image focusing and an absolute knowledge of 1 meter to some tens of meters. The orbit knowledge accuracy can be further refined by using satellite laser tracking (SLR), dedicated instruments such as Precise Range and Range-rate Equipment (PRARE, installed on board of ERS-2) or the Doppler Orbitography and Radio-positioning Integrated by Satellite instrument (DORIS, installed on ENVISAT).

With the referred instruments, the absolute orbital trajectory can be determined with centimeter accuracy, but until recently, the required time correlation between orbit determination and SAR instrument was not always available with the desired accuracy, reducing the azimuth localization error to some meters.

Recent satellites such as Radarsat-2 using GPS or even Dual-frequency GPS (TerraSAR-X, Sentinel-1) can achieve centimeter level orbit accuracy without the need of additional instruments. Having an on-board GNSS receiver next to the SAR instrument obviously simplifies the generation of accurate time correlation elements for the SAR acquisitions.

⁸ In the TerraSAR-X multimode SAR processor (TMSP), the effect of coarse azimuth time quantization is relaxed by an approach to reconstruct hidden digits of time annotation based on cross-information between adjacent time tags. The method, applied during SAR processing but hardly feasible in post-processing, is described in [42].

It is well known that the orbital trajectory derived with dynamic models refers to the satellite center of mass and not to the position of the GNSS or SAR antenna. Therefore, the offset vectors of both antennas in the satellite coordinate system and the orientation (attitude) of the platform must be taken into account when using GNSS for precise orbit determination or annotating the sensor's trajectory to SAR measurements.

This fact is not always accurately implemented in current missions. While TerraSAR-X products are annotated with the SAR antenna flight track, Sentinel-1 orbit annotation the products still refers to the satellite center of mass. The distance is approximately 2 m and will lead to elevation angle dependent range offsets in the ALE analysis. While the average range offset contributes to the range calibration constant and is in this way implicitly compensated, the remaining, uncompensated variation across elevation angles is at the centimeter level. This is illustrated in Figure 9 for the Sentinel-1 satellite and the SAR antenna mounted at the bottom of the bus. Using the bus dimension [56] and taking into account the mechanical roll steering of about 29.5° [57], we obtain a difference of 29 mm between near range and far range for IW TOPS (25° to 42° incidence angle) due to the difference of the CoM and the SAR antenna. For the computation, we assumed the center of mass at 2000 mm with respect to the top of the spacecraft, and the antenna reference point at the bottom of the spacecraft, see Figure 9.

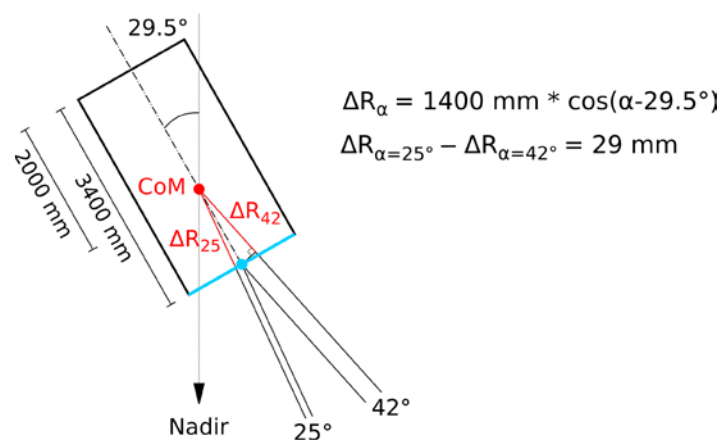


Figure 9: Impact of the difference between center of mass (red) and a geometrical SAR antenna reference (blue) on range observations. The effect is shown for the Sentinel-1 spacecraft having an average roll steering of 29.5° and the near range to far range coverage for the IW TOPS of 25° to 42°.

2.5.3. SAR Processing

SAR processing is a quite complicated 2D space-variant problem. In all recent missions, increasing accuracy needs and system aspects such as aging oscillators or failing transmit/receive modules require updates of the SAR processor software. In ongoing SAR missions, practical constraints with regard to the consistency between already existing and future data takes may restrict the scope for

redesigns of the SAR processor. In particular when a huge amount of data is already acquired and processed, as it is true for the Sentinel-1 mission, a complete reprocessing of all data with an improved algorithm is hardly performable. In this case, new scientific findings or increased demands from users' side have to be considered in an alternative way. In this situation, providing the image users with a guideline for offline corrections is the only applicable way-out.

The task of SAR processing is to integrate or focus the received backscatter energy originating from individual ground scatterers to pixel locations which correspond to the scatterers' location on ground. In an ideal case, the coordinate axes of the two dimensional output image represent the minimum distance r_0 and the corresponding instant in time t_0 , respectively. On that basis a geolocation is straightforward: Describe a circle with radius r_0 perpendicular to the tangent of the flight trajectory at time instant t_0 and intersect it with the earth surface (see zero Doppler equations in section 2.3). In practice, the coordinate axes of the focused image are defined in a different way and, to complicate things even more, these definitions may be reached only approximatively since the instrument moves in-between and during pulse transmission and reception. Furthermore, different SAR missions handle this differently. Common to all missions is the fact that they do not provide absolute range measurements r_0 . Instead, a further time measurement axis is established which annotates the shortest round trip delay for a given target. The difficulty to deduce from pulse delay measurements to exact ranges is addressed in section 2.6, along with practical solutions. The definition of the azimuth time annotation t_0 is closely related to the approximations introduced by the respective SAR processor. In order to obtain an azimuth time annotation t_0 which explicitly represents the time instant along the flight trajectory where the satellite reaches the position of closest – perpendicular – range to a given target in a strict geometrical sense, the azimuth time annotations of SAR products from different missions have to be individually corrected according to implied approximations and conventions. After an introduction to the concept of Zero Doppler Processing in, section 2.5.3.1, commonly used approximations and their impact on azimuth time are addressed in the subsequent sections.

2.5.3.1. Zero Doppler Processing

Due to the transmitted chirp signal and the large azimuth beam width, each point on the ground is spread over millions of raw data pixels in range and azimuth. Signal processing techniques are required to separate the signal contributions from different targets and to focus the contributions from a single target at one location in the processed SAR image. Fundamental signal theoretical relations and constraints in affordable computation time define some limits on how precisely both tasks can be accomplished. There exist different focusing algorithms, e.g. chirp scaling, range Doppler or omega-k and back-projection, the slowest but most accurate method. Even a coarse introduction would go beyond the scope of this document. With this regard, we refer to further reading, in particular standard works like [7].

A fundamental signal processing operation applied several of times in these algorithms is the multiplication of the SAR signal with different linear or quadratic phase terms in the 2-D spectral domain,

2-D time domain or in a mixed domain like the range- Doppler domain (i.e. time w.r.t. range dimension but spectrum w.r.t. azimuth dimension). Even higher order terms occur in some modern variants of these algorithms in order to model the acquisition geometry more precisely. Sometimes, limits for the focusing accuracy are reached where slightly deviating phase operations are required by different targets but are not separately applicable in any of these domains. Thus, processor approximations are to a certain extent unavoidable. Further approximations might be intended to reduce computational effort, e.g. for near-real-time processing.

In SAR processor design, there is the choice between two conventions for the location, where a focused target shall occur in the processed SAR image: either at the target's beam center time or at its zero Doppler time. Sentinel-1 as well as TerraSAR-X opted for Zero Doppler processing. This convention is appealing because zero Doppler refers to an intrinsic signal property and avoids in this way a dependency of the focused target's position on a signal feature like the Doppler centroid, which needs to be estimated from the data. By applying only such spectral phase terms where the first derivative is zero at zero frequency, signal contributions with zero Doppler remain at the target's closest approach. All other spectral contributions are shifted relative to this particular position by adequate choice of the phase functions to be applied.

2.5.3.2. Stop-Go-Approximation and Related Corrections

Precise target location measurements pose high demands on the geometric accuracy of the underlying SAR algorithms. Considering the archived performance of current SAR sensors and the abilities of advanced analysis techniques on such location measurements, the applicability of processor approximations in SAR focusing – once introduced for the sake of algorithmic manageability and computational efficiency – has to be reassessed. In particular, the so-called Stop-Go-Approximation is questionable because the satellite motion during a single echo event is no longer negligible at the aspired accuracy level. This section will discuss the following aspects in detail:

1. Satellite motion from pulse transmission until echo reception
2. Satellite motion during echo reception
3. Satellite motion during pulse duration
4. Increase of signal travel distance

The underlying idea of the Stop-Go-Approximation is that the sensor moves very slowly compared to light velocity of the radar signal. As long as this approximation is applicable, the satellite position at the instant of radar pulse transmission and its position at the instant of echo reception can be assumed to be almost equal. Consequently, the sensor motion can be modeled in such a way that the sensor assumingly remains at the same place from pulse transmission until echo reception ("stop") and thereafter moves to the next place ("go") for transmitting the next pulse and receiving the corresponding echo. This approximation is appealing, as it minimizes the computational effort in SAR focusing. An assumingly constant azimuth time for an entire echo event implies that rows and columns

of the raw data matrix correspond to perpendicular azimuth and range axis respectively – a desired feature that simplifies many processing steps in SAR focusing.

However when demanding location accuracy at subpixel level, the motion of the sensor between the instants of pulse transmission and echo reception cannot be neglected anymore. As a consequence of this slight motion, even the acquisition geometry of a single antenna SAR system is strictly speaking bistatic. To estimate the amount of this effect: In the case of space-borne SAR sensors Sentinel-1 or TerraSAR-X, the satellite moves about 30-40 meters⁹ between pulse transmission and the echo reception and some meters during pulse transmission and reception. In the following, we analyze the effect of this position change on SAR data at different levels of detail. At each level, another aspect of the bistatic effect becomes significant. We deduce methods to consider the particular aspects (to be applied most appropriately during SAR focusing, otherwise in post-processing of location measurement results). In consequence, we can define several stages of bistatic corrections where location accuracy but also the computational effort increases from stage to stage. Finally, there is a tradeoff between the requirements on location accuracy and the effort to be invested in.

With regard to the design of future SAR products, a data provider should disburden his users as far as possible from the task to apply corrections in a post-processing of location measurement results. Some corrections would request detailed knowledge about the SAR instrument or about the used SAR focusing algorithms and only a few expert users are able to apply those correctly. Therefore, SAR products should be designed to be as simple-to-use as possible and all possible corrections should be performed already in the SAR processor. If this is not possible, e.g. in order to maintain consistency with existing archive products, very clear instructions should be provided to the user in order to perform these corrections, i.e. to achieve highest possible geometric accuracy and to maintain consistency with older products and SAR processor versions.

The approximate amounts of the satellite motion effects for Sentinel-1 and TerraSAR-X are listed in Table 1. Depending on the required accuracy, Table 1 gives a guideline what effects a user has to consider by post-processing in his ALE analysis, provided that the SAR processor does not already compensate for these effects.

⁹ based on typical values of about 7.5 km/s for the satellite velocity and about 4-6 ms for the signal round trip time

Table 1: Approximate amounts of satellite motion effects for Sentinel-1 and TerraSAR-X. The exact amount depends on parameters like imaging mode and acquisition geometry. Thus, the table gives just a coarse orientation on the effects' order of magnitude. Values in braces refer to effects, the operational SAR processor (IPF for Sentinel-1 data or TMSP for TerraSAR-X data) already compensates for.

Effect	Sentinel-1 azimuth	Sentinel-1 range	TerraSAR-X azimuth	TerraSAR-X Range
Motion from pulse transmission to echo reception	(30 – 40 m)	–	(30 – 40 m)	–
Motion during echo reception	0.6 – 5.2 m	–	(0.04 – 3.8 m)	–
Motion during pulse duration	0.2 – 0.45 m	–	(0.2 – 0.45 m)	–
Increase of signal travel distance	–	0.15 – 0.25 mm	–	(0.15 – 0.25 mm)

2.5.3.2.1. Satellite Motion from Pulse Transmission until Echo Reception

Taking into account that the instants of pulse transmission and echo reception are different, the first stage of geometric correction, which is the only one being compatible to Stop-Go-Approximation, is the choice of the most appropriate azimuth time tag for the echo event. Conventionally, each SAR raw data line is labeled onboard by the time of reception of the first sample (not the pulse transmission time). Based on the acquisition geometry of the particular data take, also the number of pulse repetition intervals between pulse transmission and echo reception is determinable (if not already annotated in the raw data package). In this way, we also know the instant of pulse transmission. The reflection on ground happened sometime in between pulse transmission and echo reception.

Finally, we are interested in the zero Doppler time as the instant when the zero Doppler plane crosses the target. In case of a single sensor and small changes of along path acceleration due to nearly circular orbits, this instant is in good approximation half the time between the instants of pulse transmission and the pulse reception. As long as the Stop-Go-Approximation is kept, the instant half the time between pulse transmission and the reception of the mid-range echo sample is the most appropriate azimuth time tag for a raw data line, see Figure 10. This concept is already adopted in Sentinel-1 and in TerraSAR-X focusing, so that with regard to this correction no action is left to the image user. In contrast, this concept is challenged for bistatic constellations (e.g. in the TanDEM-X mission). Here, a numerical evaluation of zero Doppler time is unavoidable.

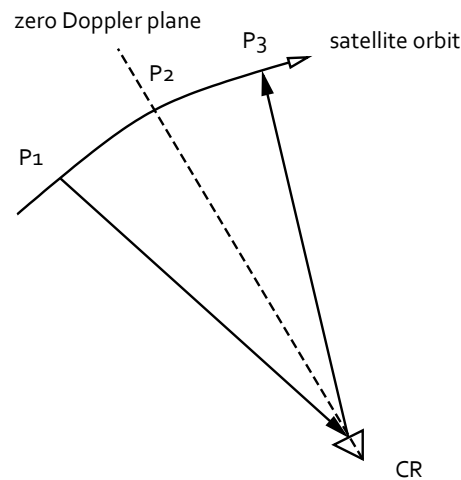


Figure 10: Satellite motion from pulse transmission until echo reception (non-scale schematic diagram). While the radar signal is traveling, the satellite moves from position P₁ (at instant of pulse transmission) via position P₂ (at instant of pulse reflection on ground) to position P₃ (at instant of echo reception).

2.5.3.2.2. Satellite Motion during Echo Reception

In the second stage, we take a closer look on the echo receive time of targets at different ranges. Obviously, the echo from a near range target is received first; the echo from a far range target is received last. However, we are interested in the zero Doppler azimuth time of the particular targets which is time shifted from the instant of pulse transmission by half of the signal travel time. Consequently, it varies from near to far range targets by half of the amount of the range time difference as shown in Figure 11. Thus, the Stop-Go-Approximation is no longer helpful, as it leads to a geometric squint in the raw data matrix. The orientation of range lines differs slightly from the exact zero-Doppler range direction and this squint has to be corrected for.

In case of TerraSAR-X datatakes, the images are already de-skewed. In contrast, in case of Sentinel-1 datatakes, this operation is left to the user. As the azimuth time at a predefined reference range is correct (in case of TOPS burst mode: separate reference ranges per beam), the user has to correct the measured azimuth time of a ground target by half of the fast time difference relative to reference range [49] by *adding*

$$\Delta t_{\text{target}} = \frac{1}{2} \cdot (\tau_{\text{ref}} - \tau_{\text{target}}). \quad \text{Eq. 6}$$

to the measured azimuth time times $t_{m,CR}$ derived from the point target analysis, see section 2.5.5. To evaluate the amount of satellite motion during pulse reception: A typical swath width of a Sentinel-1 IW datatake is in the order of 250 km, corresponding to about 1 millisecond range time difference between near and far range targets. Consequently, the zero-Doppler azimuth time varies within

the swath by 0.5 milliseconds, resulting in about 3.5 meters of skew between near and far range edge of the SAR image if the effect is not compensated.

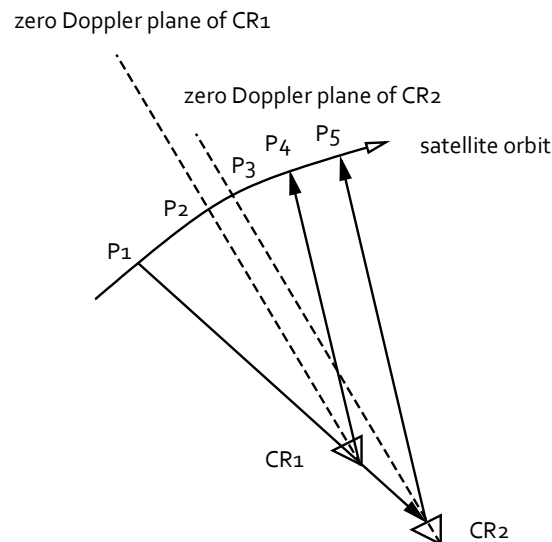


Figure 11: Satellite motion during echo reception (non-scale schematic diagram). There are two CRs: One in near range and one in far range. Both CRs reflect the radar pulse at different times and also the instants of echo reception differ. Consequently, the satellite is at different positions: P2 while pulse reflection by near range CR1, P3 while pulse reflection by far range CR2, P4 and P5 while receiving the respective echoes.

2.5.3.2.3. Satellite Motion during Pulse Duration

The third stage refers to the duration of the radar pulse. Very short pulses would require high peak transmit power which is technically not feasible. Therefore long duration phase coded pulses are usually the preferred radar pulse type. The most common pulse form for civilian SAR systems is a chirp function¹⁰ where the instantaneous frequency is either linearly increasing (up chirp) or linearly decreasing (down chirp) with time. An implication of the relatively long pulse duration on location accuracy is that even the time interval from the transmission of the leading edge of the pulse until the transmission of the trailing edge suffices for a considerable satellite motion, see Figure 12. In case of Sentinel-1, the pulse duration is typically in the order of 50–60 microseconds and the satellite moves by about 40 centimeters during this time span. The same time interval elapses while receiving the echo from a single ground target. In consequence, the range chirp is smeared out in azimuth direction too, resulting in a slight azimuth defocusing.

¹⁰ In contrast, military SAR systems prefer other, less easy detectable pulse shapes.

With the usage of chirp signals as radar pulses, the combined effect of phase coding and satellite motion is a separation of the different range frequencies in azimuth time. Depending on whether an up- or a down-chirp is sent, low range frequencies are received at earlier slow time than high range frequencies or vice versa. This coupling of range frequency and azimuth offset allows for a relatively easy compensation for the motion effect during SAR processing. In SAR focusing, a range frequency dependent azimuth shift (which corresponds to a bilinear coupling term of azimuth and range in 2-D spectral domain) can be applied. In contrast, compensation of the defocusing effect by post-processing at the user's side is cumbersome due to the limited access to the multitude of required processing parameters, and therefore hardly applicable.

While the coupling term in the 2-D frequency domain is a welcome remedy to compensate for the satellite motion effect during pulse duration in SAR focusing (so it is done there), it has an unwelcome side effect on spectrally unbalanced signals when SAR focusing does not account for this term. This applies to early and late azimuth targets within a focused ScanSAR burst (TerraSAR-X imaging modes SC and WS) or focused TOPS burst (Sentinel-1 imaging modes IW and EW), or within a focused Staring Spotlight image (TerraSAR-X imaging mode ST), as their Doppler centroid deviates significantly from zero frequency in the azimuth spectrum due to the particular acquisition geometry (see section 2.5.1). This spectral imbalance goes along with an average position offset in the range time domain and vice versa: An average frequency offset in range goes along with an average azimuth position offset. However, the latter refers to exotic special cases like split bandwidth data takes [10] that are not operational products of the Sentinel-1 or TerraSAR-X missions.

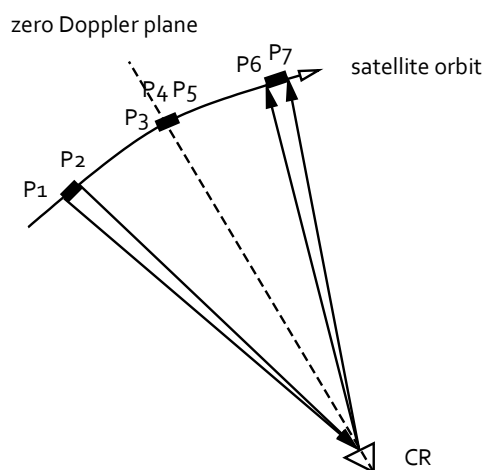


Figure 12: Satellite motion while pulse duration (non-scale schematic diagram). The satellite moves from P₁ to P₂ while transmitting the pulse. Consequently, there is an approximately equal motion (from P₆ to P₇) while receiving the echo. P₃, P₄ and P₅ denote the satellite positions at the instants when leading edge (P₃), center (P₄) and trailing edge (P₅) of the radar pulse are reflected on ground. The orbit segments the satellite passes during pulse transmission (segment P₁–P₂), pulse reflection (segment P₃–P₅) and echo reception (segment P₆–P₇) are highlighted by thick lines.

2.5.3.2.4. Increase of Signal Travel Distance

The fourth stage refers to a small range effect of the satellite motion. Because of the satellite motion, the positions and times of pulse transmission and echo reception are different and the zero-Doppler time is between both. At least at one of both instants, the signal travel distance is longer than the shortest geometrical distance, see Figure 13. In fact, the minimum realizable round trip distance (and accordingly the minimum round trip time) from sensor to ground and back to sensor results when the radar pulse is transmitted slightly (i.e. half round trip time) before the closest approach and the echo is received accordingly after the closest approach. However, the resulting slight increase in signal travel distance amounts to few tenths of a millimeter level and is negligible so far.

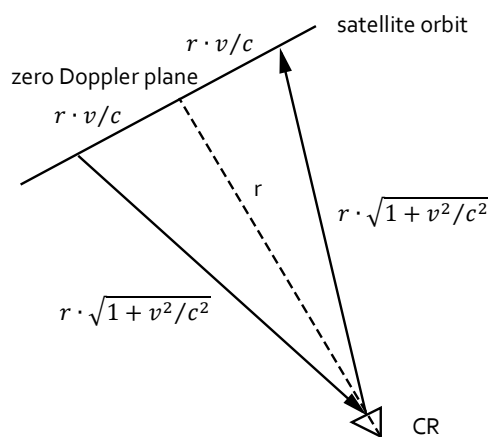


Figure 13: Increase of signal travel distance (non-scale schematic diagram). According to Pythagorean Theorem, the distance covered by a pulse, transmitted half of the signal travel time before closest approach, amounts to approximately $r \cdot \sqrt{1 + v^2/c^2}$ where r means the distance between sensor and target at closest approach, v the speed of the satellite and c the light velocity. The analogous geometric considerations are true for the echo received half of the signal travel time after the closest approach.

2.5.3.3. Relativistic Effects

Strictly speaking, location measurements by SAR are affected by relativistic effects too. There is the relative velocity effect due to the satellite motion relative to earth surface, quantified by the Lorentz factor $\gamma_{\text{velocity}} = \frac{1}{\sqrt{1-\beta^2}}$, with $\beta = \frac{v}{c}$ and the gravitational effect (factor $\gamma_{\text{gravity}} = \frac{1}{\sqrt{1+2\phi/c^2}}$) due to the different gravity potential $\phi \approx g \cdot h$ at satellite orbit and earth surface. The order of magnitude of both effects was estimated in the context of the TerraSAR-X mission and it was found that both effects are too small and may be safely neglected in present applications. Based on the acquisition geometry of two actually acquired datatakes of the same region, one with 34° incidence angle and one with 46° incidence angle, the computed relative velocity effect amounts to about 0.2 or 0.23 millimeters, respectively. The gravitational effect is even lower (by almost one order of magnitude). It amounts to -0.033 or -0.038 millimeters, respectively. Thus, one can conclude that both relativistic effects are negligible as long as more dominant effects make sub-millimeter accuracy unattainable.

2.5.4. Sensor Internal Delays

Beyond the external signal propagation delays that are discussed in section 2.6, there are also sensor internal delays and possible azimuth timing offsets. The chirp signal has to be transmitted from the signal generator to the transmit antenna. The received echo signal has to be transmitted from the antenna to the analogue to digital converter before the digitized signal is stored and time tagged. Both transmission paths require some cable lengths, increasing signal travel distance and signal travel time accordingly. These additional signal travel distances beyond the geometric distance between the phase centers of sensor antenna and target on ground have to be compensated for.

The precise actual cable lengths (most probably slightly different from the designed cable lengths due to unavoidable manufacturing tolerances) are measurable while the sensor is assembled or tested on ground. In fact, geometric calibration usually takes place not before instrument calibration in space. The reason is that at the aspired high accuracy level, a complex measurement instrument such as a SAR sensor is affected by a multitude of disturbing effects to be compensated. In the course of time since the early days of SAR, scientific progress enables to identify and model an increasing number of disturbing effects at increasing accuracy level. After all, to document the state of the art in compensating for such effects as far as they are manageable and relevant at the attainable accuracy level is the aim of this technical note. Beyond that, the only solution to handle residual disturbances, where the cause is still in need of investigation, is to measure their combined effect as an average by instrument calibration. The combined geometrical effect is annotatable in two calibration constants, an azimuth and a range offset, so that any location measurement by the sensor can be compensated for these average offsets by subtracting them from the measured values. Usually, this is already done in the context of SAR processing and the image user need not care about it.

As the sensor internal cable lengths yield the major contribution to the geometric calibration constant in range, this constant is frequently denoted by the term "sensor internal delay," notwithstanding that the constant covers other contributions too.

A drawback of the calibration approach is that the validity of the calibration constants is coupled with a fixed measurement method. As soon as a disturbing effect is modeled more precisely in the SAR measurements as it was beforehand considered in instrument calibration, a certain portion of the effect might be considered twice: once as contribution to the calibration constant that covers all the hitherto unconsidered effects, and once by the new more exact model for the effect.

For instance, the product annotation of TerraSAR-X images provides an estimate for the dry part of the tropospheric delay (see section 2.6.1) on the base of a simplified model, sufficient to attain localization accuracy below meter level. This was considered sufficient when TerraSAR-X was launched in 2007. Consequently, the geometric calibration of TerraSAR-X refers to this estimate for the dry part of tropospheric delay so that the average effect of the wet part contributed to the range calibration

constant. In contrast, this average contribution has to be omitted from the calibration constant in such measurements where the actual value of the entire tropospheric delay at the instant of the data-take acquisition is considered by the more precise models discussed in section 2.6.1.

In conclusion, any refinement of the measurement method, which might be based on new scientific findings or result from increased demands on measurement accuracy, requires a recalibration of the sensor geometrical calibration constants. In the end, a discerning user applying sophisticated measurement methods might be faced by the situation to evaluate new recalibration constants for himself to be applied in his measurements.

2.5.5. Point Target Analysis

The primary objective of the point target analysis (PTA) is the evaluation of the location of point scatterers like CR's in terms of azimuth time $t_{m,CR}$ and range time $\tau_{m,CR}$. Single look complex (SLC) images in slant range geometry (the most simple image products from SAR sensors) are the most appropriate image representation for PTA because any error related to resampling as it is performed in GRD (ground range, detected) products are avoided. Beside the point scatterer' location, the PTA shall also provide meta-information that may be required later on in the analysis of the measurement results, as there are:

- Peak resolution
- Peak power
- Signal energy
- Signal to clutter ratio
- Sidelobe ratios

In case of burst mode data (ScanSAR or TOPS), also the relative pixel position of the peak within a burst is a useful information for further analyses. An overview on the determination and the scope of these parameters is given at the end of this section.

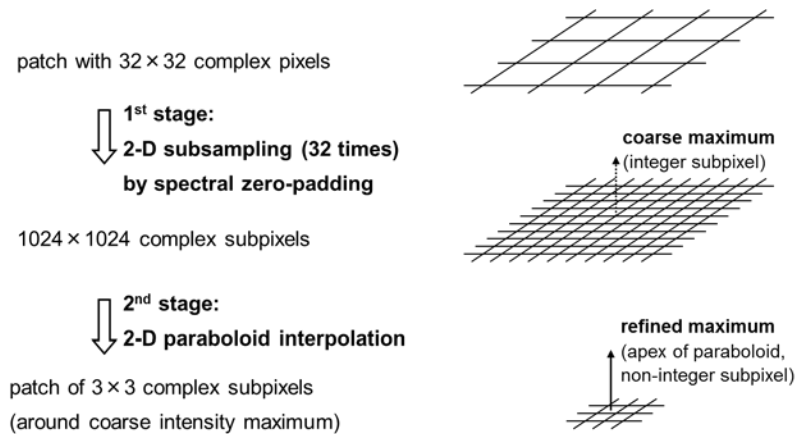


Figure 14: Schematic diagram of the proposed two-stage method [44.]

Precise measurements of the radar times $t_{m,CR}$ and $\tau_{m,CR}$ for a CR – at centimeter level or even below – require PTA at sub-pixel level. To understand, why subpixel accuracy is attainable, it requires a closer look on the pulse shape of a corner reflector’s impulse response. At first glance, one might expect that the signal energy is concentrated in a sole point because the triple bounce reflection geometry of a trihedral corner reflector (oriented toward the sensor according to [RD1]) guaranties that all of those echo contributions receivable by the sensor coincide in their round trip distance and in their zero Doppler time. However, the band limitation of the SAR signal in range and azimuth widens the impulse response to a 2-D sinc pulse. In consequence, the signal energy is spread over some pixels¹¹ while the signal shape is well defined and analytically describable. Therefore, we can interpolate subpixels of the point target response and consequently, we can find the subpixel peak position in the interpolated image patch.

A commonly used interpolation technique is spectral zero padding. As the signal is band-limited, its 2-D spectrum (computed by Fast Fourier Transform (FFT)) can be continued by introducing additional zeros outside the signal’s waveband. The increase in the number of FFT bins results in a finer sampling when transforming the 2-D spectrum back to 2-D time domain. In the oversampled image patch, the peak location is detectable as position of the intensity maximum with an accuracy of one pixel in the new finer sampling grid. Thus, the choice of the oversampling factors in azimuth and range controls the attainable peak localization accuracy.

Restrictions for the oversampling factor are given because of the memory consumption of the oversampled patch and by the computational effort for the inverse 2-D FFT. Thus, typically chosen oversampling factors are in the order of 32, 64 or maybe 128. Consequently, the peak localization accura-

¹¹ We assume here that azimuth and range sampling rate in the SAR image comply with the Nyquist criterion.

cy attainable by pure oversampling is limited. A reasonable solution to refine the measured peak location is a post-processing by analytical interpolation techniques, e.g. a paraboloid interpolation as illustrated in Figure 14. The concept is not really new (see e.g. [43]) but still not in common use, notwithstanding its substantial performance gain (analyzed in [44]). As the signal shape of the oversampled sinc pulse is fairly smooth, the signal shape in between the oversampled pixels around the peak can be fitted by a model function. The simplest function that describes a peak is an elliptic paraboloid

$$f(x, y) = a_{20}x^2 + a_{02}y^2 + a_{11}xy + a_{10}x + a_{01}y + a_{00}. \quad \text{Eq. 7}$$

It already suffices for this purpose. As there are just 6 parameters in the formula, function fitting is applicable on base of a sub-patch of just 3x3 oversampled pixels, centered on the intensity maximum in the oversampled patch. With fitted a_{ij} , the apex of the paraboloid can be computed analytically and yields a more precise measurement for the peak position and the peak power.

Once, the sub-pixel position¹² $(x; y)$ of a CR in the image is estimated, it can be transformed into radar time coordinates

$$\begin{aligned} \tau_{m,CR} &= \tau_{Img0} + \frac{x}{RSF}, & x \geq 0 \\ t_{m,CR} &= t_{Img0} + \frac{y}{ASF}, & y \geq 0 \end{aligned} \quad \text{Eq. 8}$$

based on the following parameters taken from product annotation:

- fast time (τ_{Img0}) of the first range sample in near range
- range sampling frequency (RSF)
- slow time (t_{Img0}) of the first range line in early azimuth
- azimuth sampling frequency (ASF). As long as no resampling is applied in SAR processing, it equals to the pulse repetition frequency (PRF) of the raw data and might be annotated under this term.

In the process, the accuracy of these annotation parameters may affect the attainable accuracy of the CR's radar time coordinates. Potential error sources in this context are a limited knowledge of the actual parameter values or a limited number of digits in the product annotation.

¹² These equations refer to a pixel numbering starting with pixel (0;0) in the early azimuth, near range corner of the SAR image. Users, preferring a pixel numbering starting with pixel (1;1), have to substitute x by $x-1$ and y by $y-1$.

We estimated the measurement resolution of the proposed two-stage method, based on oversampling and subsequent parabola interpolation, by a series of measurements performed with increasing oversampling of 8, 16, 32 ... 512 in the first stage. Higher oversampling factors were out of question in our experiment because of memory constraints. In the measurement series, we observed stable peak location results differing by less than $1/10000$ pixel if the oversampling is at least 32, as it is shown in Figure 15. Even a coarse oversampling of 8 or 16 results in a difference of less than $1/1000$ pixel compared to more exact measurements. Thus, the experiment gives incidence that the two-stage method is at least as precise as pure oversampling with factor 512 and we conclude that oversampling by 32 is sufficient in combination with the paraboloid interpolation which actually boosts the measurement resolution of the peak location. The high consistency of the measurement result hypothesizes that even the accuracy of pure oversampling with factor 512 might be outperformed by far. Aiming at comparable resolution by pure oversampling is much less efficient and would be barely manageable on today's hardware. With measurement accuracy better than $1/512$ pixel, the proposed method guarantees that PTA does not introduce any significant additional measurement artifact to the measurement result.

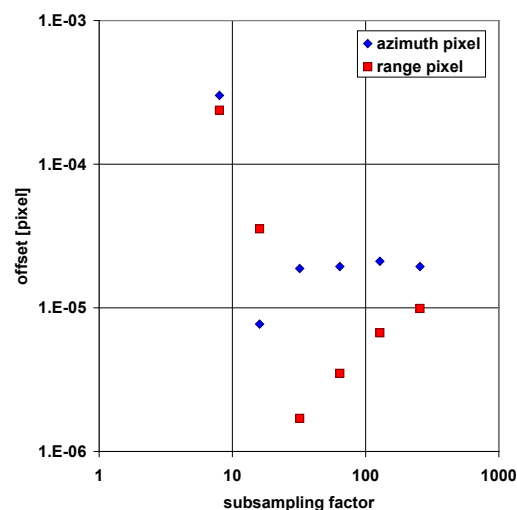


Figure 15: Estimation of measurement resolution of the proposed two-stage method. Chosen oversampling factor in the first stage (x axis) versus offset of measured peak position relative to a two-stage measurement result for an oversampling factor of 512 (y axis). The measurement results differ by less than $1/10000$ pixel. A comparison against pure oversampling of comparable resolution is inapplicable due to resource constraints [44].

The meta-information, derived as a byproduct of PTA, is a useful instrument for many purposes in the analysis of the measurement results. Some parameters indicate irregularities during the measurement process so that corrupted measurement values can be excluded from further analyses. Other parameters are valuable quality indicators in the validation of the SAR processor performance. Further parameters are required in subsequent processing steps, but they are conveniently obtained when derived in conjunction with the PTA, e.g. the incidence angle, which is needed in the computa-

tion of signal path delays (see section 2.6). Table 2 gives an overview on the particular parameters, the applied definitions for their measurement methods and their scope in the framework on CR measurements. Within the framework of the ERS-1 mission, ESA fixed measurement methods for these parameters to be applied for calibration and validation of this mission [45]. The definitions are kept for Sentinel-1A/B and, in the meantime, adopted by DLR for TerraSAR-X/TanDEM-X calibration and validation. As they are widely proven and tested in this way, we largely refer to the same definitions in this document. Minor deviations result from the more exact approach to measure the peak location that we propose in this document.

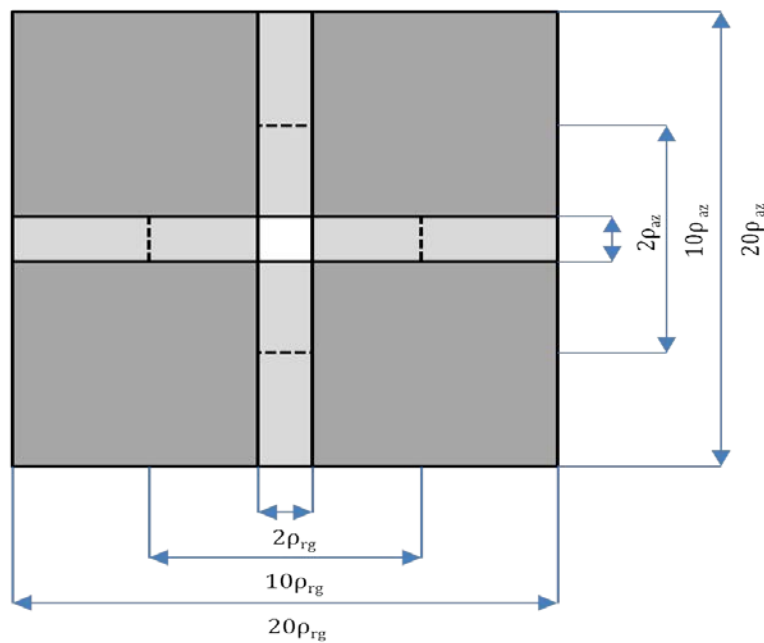


Figure 16: Size and arrangement of the measurement patches for the characteristics of clutter (dark grey), sidelobes (light grey) and mainlobe (white). The peak position of the CR defines the center of the mainlobe area. Sidelobe areas and the measurement patches for the clutter power are arranged around the mainlobe. ρ_{az} and ρ_{rg} refer to the 3 dB width in azimuth and range, respectively.

Table 2: Meta-information extracted as byproduct during PTA

Parameter	Description
Peak resolution, 3 dB width	<p>Applied definition, measurement method:</p> <p>Separate values for azimuth and range; distance of 3 dB points before and after the peak in range and azimuth cut, respectively.</p> <p>Scope:</p> <p>Verification of sensor and processor performance.</p>
Peak power	<p>Applied definition, measurement method:</p> <p>Signal power (i.e. in case of SLC data: Squared signal amplitude) in digital numbers at apex of interpolated paraboloid.</p> <p>Scope:</p> <p>Check against saturation. For 2x16 bit complex integer representation of image pixels, the peak power shall stay under 90 dB. CR measurements violating this limit are saturated and shall be excluded from further analyses.</p>
Signal energy	<p>Applied definition, measurement method:</p> <p>Integrated signal energy in a cross-shaped area (totality of white and light grey areas in Figure 16). The arms of the cross are oriented in range and azimuth direction, respectively. Length and width of the arms are derived from the 3 dB width of the point scatterer response. The integration is applied by summing up the oversampled squared amplitudes of the pixels in this area and multiplying the result by the pixel area and the radiometric calibration factor, read from product annotation.</p> <p>Scope:</p> <p>Check of CR state: water, snow or leaves in the CR affect the backscatter geometry and consequently cause a drop in the signal energy. Thus, a significant drop of the signal energy below the expected value, derived from theory (see [RD1] for detailed information), is a good indicator for such foreign disturbance. Location measurement values acquired under such irregular conditions shall be removed from further analyses because of the possibly shifted phase center of the contaminated CR.</p>

Parameter	Description
Mainlobe energy	<p>Applied definition, measurement method:</p> <p>Integrated signal energy in the mainlobe area (white area in Figure 16) of 2×2 resolution cells (2 times 3dB width), centered on the peak; same integration method as used for the signal energy.</p> <p>Scope:</p> <p>Used as input value for the estimation of signal to clutter ratio and integrated sidelobe ratio (see below).</p>
Sidelobe energy	<p>Applied definition, measurement method:</p> <p>Integrated signal energy in the totality of sidelobe areas (light grey areas in Figure 16); same integration method as used for the signal energy.</p> <p>Scope:</p> <p>Used as input value for the estimation of integrated sidelobe ratio (see below).</p>
Clutter power	<p>Applied definition, measurement method:</p> <p>The average energy of the clutter is estimated nearby the point scatterer response, but outside the mainlobe and sidelobe areas, so that merely clutter is present in the measurement patch. The four quadrants (dark grey areas in Figure 16), lateral of the sidelobes, may be an adequate choice for the measurement patch, provided that no other point scatter is located there (to be avoided by adequate choice of the CR's place of location!). The clutter power results by division of the measured clutter energy by the patch size.</p> <p>Scope:</p> <p>Used as input value for the estimation of the signal to clutter ratio (see below).</p>

Parameter	Description
Signal to clutter ratio (SCR)	<p>Applied definition, measurement method:</p> <p>Ratio of measured mainlobe energy and estimated clutter energy in mainlobe area, i.e. the clutter power multiplied by the mainlobe area (see [RD1] for detailed information on SCR).</p> <p>Scope:</p> <p>Computation of expected location accuracy (see [RD1]); choice of an adequate test side.</p>
Integrated Sidelobe Ratio (ISLR)	<p>Applied definition, measurement method:</p> <p>Ratio of mainlobe energy and sidelobe energy, defined above.</p> <p>Scope:</p> <p>Verification of sensor and processor performance.</p>
Peak Sidelobe Ratio (PSLR)	<p>Applied definition, measurement method:</p> <p>Separate values for early/late azimuth and near/far range; ratio of peak power and power of the maximum sidelobe in the respective direction. The detection areas for the maximum sidelobe in each of the four directions are limited to the fraction of the respective sidelobe areas next to the mainlobe (fraction of respective light grey area in Figure 16 between the edge of the mainlobe and the respective dashed line).</p> <p>Scope:</p> <p>Verification of sensor and processor performance.</p>

2.6. Signal Path Delay Correction

The comparison between the observed SAR range timings as derived from the images (see previous section 2.5 and the predicted SAR range coordinates from the reference geometry (see next section 2.7 is only possible if the wave propagation velocity through the atmosphere is taken into account.

The propagation velocity of electromagnetic waves in a medium (e.g. Earth's atmosphere) is expressed by the refractive index n which is the ratio of the velocity in the medium and the velocity in vacuum [13]. The refractive index may differ for varying frequencies, depending on the nature of the medium. Since the light velocity is lower within media than in the vacuum, the Earth's atmosphere introduces a path delay to radio signals, including the SAR range measurements. When vacuum light velocity is assumed to convert travel time to range in Eq. 5 the inferred ranges are too large.

This chapter describes several ways to estimate and correct the range delay encountered in the ionosphere and in the troposphere. The slant range delay

$$\Delta\tau_{SPD} = \Delta\tau_{SPD,Tropo} + \Delta\tau_{SPD,Iono} = 2 \frac{\Delta r_{SPD,Tropo} + \Delta r_{SPD,Iono}}{c} \quad \text{Eq. 9}$$

is composed of a tropospheric contribution $\Delta\tau_{SPD,Tropo}$ and an ionospheric contribution $\Delta\tau_{SPD,Iono}$. It is acceptable to use the vacuum light velocity for the conversion between range ($\Delta r_{SPD,Tropo}, \Delta r_{SPD,Iono}$) and time delay given the small order of magnitude (1 - 10 m).

Whenever calculating geometric ranges from SAR measurements traversing the troposphere, we have to subtract these delays from the annotated SAR range time values. *Note that we strictly stick to SAR conventions where range times always denote the true 2-way travel time and ranges always denote the physical 1-way distance.*

The correction of the atmospheric path delays in the range measurements should be handled the same way as in other geodetic observation techniques applying cm-wavelength radio signals, e.g., Global Navigation Satellite Systems (GNSS) or radar altimetry. Readers interested in the details may find them in [19]. For the geodetic techniques, the atmosphere is typically decomposed into a dispersive and a non-dispersive part [13][19]. The former is attributed to the ionosphere modelled by the total electron content (TEC) along the signal travel path, while the latter deals with the state of the neutral troposphere described by a pressure driven component and a water vapor driven component. Neglecting the path delay of the troposphere leads to slant range errors in the order of 2.5 to 4 meters along the typical line of sight of a SAR sensor, and the ionosphere causes decimeter-level errors in X-band (9.7 GHz) and errors of several meters in L-band (1.2 GHz). More detailed examples will be given in the next sections.

Note that in this document we model only atmospheric range shifts. In fact, linear ionospheric trends in azimuth may also cause shifts of the SAR image in the azimuth direction. But in the absence of accurate ionospheric data, and considering its relatively small magnitude compared with other effects described in this document, we will neglect this effect in this document. This is all the more acceptable for shorter wavelengths (e.g. X-band).

In the absence of accurate 3-D models, it is common to model the path delays governed by physical processes in zenith direction only, and to use these zenith path delays (ZDPs) as inputs to suitable empirical mapping functions to obtain the slant path delays (SPDs). Such an approach may be called the *zenith delay method*. A direct slant range computation, i.e. the *integration method*, is also possible, but comes at the expense of a re-computation if a second observation happened at the same location during the same time but with different viewing geometry. The zenith-based methods are therefore simpler to implement, because the delays need to be computed only once and may be stored in 2-D grids per epoch whereas the slant integration methods require a 3-D background model evolving with time. The benefit of the slant range integration method lies in the better representation of the horizontal angular dependency, which is not considered by the isotropic mapping functions scaling the ZPD, but may be handled by an additional horizontal gradient model. The following input data is always required, no matter which method has been selected:

- Reference coordinates of the reflector(s)
- Satellite state vectors from the SAR product annotation
- Date and time of the SAR acquisitions

The azimuth position and elevation of the satellite for the zero Doppler geometry of the reflector(s) are required inputs for the calculations and can be easily derived from the parameters above (see the Appendix). The reflector coordinates and the state vectors govern the mapping functions (zenith-delay methods) or the integration (slant-range integration methods), whereas the epoch is needed to derive the state of the atmosphere from the models. The following sections discuss several methods to correct tropospheric and ionospheric path delays which were implemented and tested by DLR/TUM during the TerraSAR-X ALE experiments at different test sites. It is important to note that the equations are stated such that the resulting slant range delay (see Eq. 9) always needs to be *subtracted* from the SAR range measurements extracted from the image raster.

In principle, the methods discussed may be also used for SAR product annotation, some even in near real time application, as rapid data or predated data are available, but this topic is beyond the goal of this document. The timely availability of underlying atmospheric products is of less importance when performing a high quality ALE analysis, because characterization of the SAR sensors is only meaningful if performed in post-processing, when all of the final-quality auxiliary products are available.

Readers should be also aware that the best possible ALE results are achieved if the corrections are based on nearby GNSS stations. While a perfectly reasonable expectation when calibrating SAR sensors at dedicated test sites, it is not a feasible operational requirement for generating corrections for enhanced SAR products available worldwide. This restriction will need to be resolved in the future, should such enhanced SAR products become operational, but for the purposes of this document, high quality ALE analysis will be the primary focus.

2.6.1. Troposphere

In atmospheric physics, the neutral atmosphere is divided into the troposphere and the stratosphere. However, for the purposes of microwave propagation through the atmosphere, one usually refers simply to the troposphere and assumes a typical vertical extension of about 50 km. This part of the atmosphere is non-dispersive for frequencies up to 30 GHz [13], and thus the corrections may be equally derived for all common SAR payloads (X-, C-, and L-band). The refractive index of the troposphere is a function of pressure, temperature and partial water vapor pressure, and can be decomposed into a wet and dry component. This property enables a separation into a wet and a dry (hydrostatic¹³) path delay [14]. While the hydrostatic part comprises approximately 90% of the overall delay and is well suited to pressure driven modelling, the wet component undergoes rapid changes due to the high spatiotemporal variability of water vapor. The hydrostatic correction is closely linked to topography. Hence, the reflector height has to be taken into account, either by transforming the pre-computed delays for the reflector height or by performing the integration accordingly.

For the purpose of eliminating the tropospheric path delay during ALE processing, we present three different methods: the slant range integration of atmospheric models of the European Centre for Medium-Range Weather Forecasts (ECMWF), the use of globally pre-computed zenith path delays along with the Vienna Mapping Function 1 (VMF1), and the use of zenith path delays inferred from GNSS observations. Note that the former two methods are applicable at a global level and may allow for path delays distributed with future SAR products, while the last method is limited to sites with high-grade geodetic GNSS receivers. The derivation of path delays from individual GNSS observations is out of scope for this document, but the details can be found in [15]. The motivation for discussing this method are corner reflectors located at geodetic observatories or in the vicinity of receivers contributing to a GNSS reference network (e.g. the EUREF), for which the GNSS-based path delays are routinely distributed as daily products.

¹³ Be aware that the separation of the refractivity into dry & wet and hydrostatic & wet are two different concepts, see details in [47], pp. 80.

2.6.1.1. Path delays based on ECMWF

The European Center for Medium Range Weather Forecast (ECMWF) operationally provides 3-dimensional weather data from current and past times that can be used to integrate the SAR slant delays.

The apparent slant range increase $\Delta r_{spd,Tropo}$ caused by ignoring the signal path delay can be calculated by integrating [16] the refractivity $N = (n - 1) \cdot 10^6$ along the signal path between SAR antenna and target on the ground:

$$\begin{aligned} \Delta r_{spd,Tropo} &= 10^{-6} \int_{r_{ground}}^{r_{satellite}} N dr && \text{Eq. 10} \\ &= 10^{-6} \int_{r_{ground}}^{r_{satellite}} \left(\frac{77.6890 P_d}{T} + \frac{71.2952 e}{T} + \frac{375463 e}{T^2} + 1.45 W_{cl} \right) dr \end{aligned}$$

where T denotes the local temperature, e the local partial water vapor pressure, P_d the local dry part of the atmospheric pressure and W_{cl} the local liquid water column in the atmosphere.

The numerical constants are experimentally derived and may be subject to small changes. The variables are routinely provided by ECMWF in different data sets.

ECMWF ERA-Interim Climate Reanalysis Data¹⁴:

This data set, described in [17], is a very valuable data set and convenient to use, since it contains among others all the required parameters (pressure, temperature, humidity) from a consistent model in 3-D since 1979. The horizontal resolution of this model is approximately 80 km, with 60 vertical layers provided. Model parameters are sampled in temporal steps of 6 hours at 00:00, 06:00, 12:00 and 18:00 UTC. While the consistency of this model may be advantageous for systematic time series experiments, disadvantages include the low update frequency of the data set (once per month) and the processing delay (ca. 2 months). Additionally, there may be systematic time differences between the model sampling times (fixed UTC) and local SAR observation times (dusk/dawn local time for sun-synchronous orbits).

¹⁴ <https://www.ecmwf.int/en/research/climate-reanalysis/era-interim>

ECMWF Operational Real-Time data:

These data sets are processed continuously and are especially valuable when atmospheric data are required shortly after SAR acquisition. They are also provided with a higher spatial resolution of 8 to 10 km. Historical data are available as well, but disadvantages for time series analysis may include the numerical weather model or boundary parameters such as the model, the input data used for assimilation, or changing orography, which may introduce discontinuities into the ALE analysis.

In systematic experiments performed at DLR, we compared zenith delays derived from ERA-Interim and operational with local GNSS-delays from several stations around the world [18]. The standard deviation was between 10 mm and 20 mm, depending on the location of the GNSS-receiver and the operational data performed generally a few mm better.

2.6.1.2. Path delays based on VMF1

The VMF1 [19] is the latest development in a series of mapping functions to convert tropospheric ZPDs into SPDs. Along with such mapping functions often come pre-computed integrated path delays and one should be aware that their names are sometimes used synonymously for both the actual function and the overall ability to correct the tropospheric path delays. The VMF1 was specifically designed for geodetic observation techniques like VLBI or GNSS. The dedicated mapping function (MF) uses continued fractions of the sine of the elevation angle E , which was introduced by Marini in 1972 [20]

$$MF_{h,w} = \frac{1 + \frac{a}{b}}{\sin(E) + \frac{1 + \frac{a}{b}}{\sin(E) + \frac{b}{\sin(E) + c}}}, \quad \text{Eq. 11}$$

where the coefficients a, b, c have to be independently determined for the wet (w) and the hydrostatic (h) version of the function. The two sets of b and c coefficients stem from long-term analysis of the ECMWF ERA40 data [16]. While the b coefficients have been fixed to empirical constants, the c coefficients have to be computed by hemisphere-dependent equations. The more demanding parameters are the a coefficients which need to be updated on a daily basis using the operational ECMWF model. The Vienna University of Technology computes these a coefficients as global grids with 6 hour temporal sampling together with integrated ZPDs (hydrostatic and wet in units of meters, 1-way) as a service of the Global Geodetic Observing System (GGOS)¹⁵. Source code for computing the hydrostatic and the wet MF is also provided. It is worth noting that there also exists a second version of the VMF1 which is dedicated to the International Terrestrial Reference Frame (ITRF) sites. However, for

¹⁵ Vienna Mapping Function service: <http://ggosatm.hg.tuwien.ac.at/delay.html>

global applications only the gridded VMF1 with its corresponding coefficients is applicable. Figure 17 gives an example of the wet and the hydrostatic ZPDs from two VMF1 products of June 1st 2017.

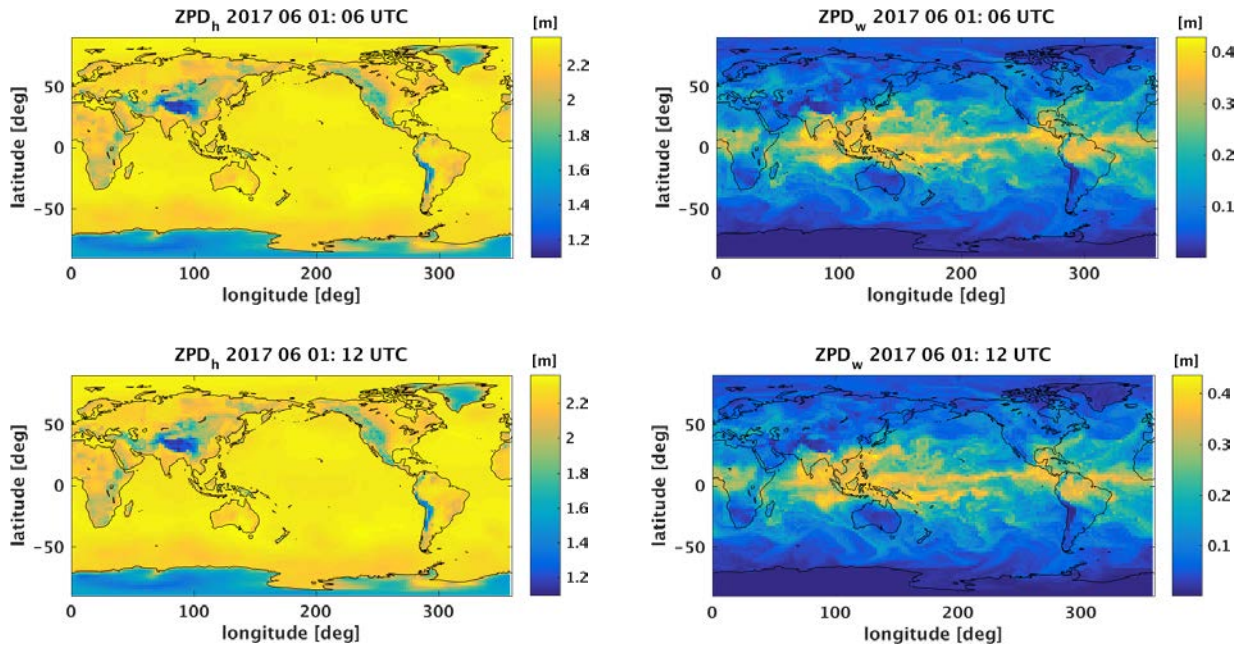


Figure 17: Examples for the global grids (2° x 2.5°) of hydrostatic (left) and wet (right) path delays distributed with the VMF1.

The vertical integration of the ECMWF model is performed with respect to a global elevation model (*orography_ell^t*) having a resolution of 2 by 2.5 degrees in latitude and longitude (approximately 220 by 280 km). The height difference of the CR to this underlying elevation model has to be taken into account when deriving the slant path delays for the SAR ranges.

In order to transform the hydrostatic ZPD, the delay is first converted to its corresponding pressure value, which is updated for the height difference between station and the elevation grid. Converting the modified pressure back to path delay yields the hydrostatic ZPD. The wet ZPD is directly obtained through an empirical decay law that takes the height difference into account. The details of the height correction are given in [21] and are based on four equations

$$p(h_g) = \frac{zpd_h(h_g)}{0.0022768} (1 - 0.00266 \cos(2\varphi_s) - 0.28 \cdot 10^{-6} h_g) \quad \text{Eq. 12}$$

$$p(h) = 1013.25 \cdot (1 - 0.0000226 h)^{5.225} \quad \text{Eq. 13}$$

$$zpd_h(h_s) = 0.0022768 \frac{p(h_s)}{1 - 0.00266 \cos(2\varphi_s) - 0.28 \cdot 10^{-6} h_s} \quad \text{Eq. 14}$$

$$zpd_w(h_s) = zpd_w(h_g) \cdot e^{-\frac{(h_s - h_g)}{2000}} \quad \text{Eq. 15}$$

where:

zpd_h = the hydrostatic ZPD

zpd_w = the wet ZPD

p = the pressure in millibar

φ_s = the station latitude

h_s = station height above the ellipsoid in meters

h_g = height of the elevation model (*orography_ell*) at the station location (from 2-D interpolation)

For the SAR observation of a particular CR, the computation can be decomposed into several consecutive steps:

1. Convert the reflector coordinates to latitude φ_{CR} , longitude λ_{CR} and height h_{CR} , and compute the elevation E of the satellite at zero-Doppler (see section 2.7.3)
2. Download the global grids holding the a_h , a_w and the zpd_h , zpd_w for the four epochs enclosing the date and time of the SAR observation. For instance, a SAR acquisition at 2016 06 01 - 16:00h would require the files *VMFG_20160101.H06*, *VMFG_20160101.H12*, *VMFG_20160101.H18* and *VMFG_20160102.H00*.
3. Perform tri-cubic interpolations (latitude, longitude, time) to obtain the VMF1 data at the location of the CR for the time of the observation: $a_{h,CR}$, $a_{w,CR}$, $zpd_{h,CR}$, $zpd_{w,CR}$
4. Evaluate the VMF1 using the outcomes of step 1 and 3 as inputs. Note that the computed mapping functions MF_h and MF_w are already corrected for the height difference between CR and the underlying elevation model, if the provided source codes are used.
5. Correct the zenith path delays of step 3 for the height difference using the Eq. 12 - Eq. 15. The hydrostatic path delay at grid height is converted to pressure (Eq. 12). The pressure is modified for the height difference (Evaluate Eq. 13 for h_s and h_g to get the Δp). Convert the pressure at station height back to a hydrostatic path delay (Eq. 14). Directly transform the wet path delay using Eq. 15.
6. Compute the summation using the outcomes of step 4 and step 5 to obtain the SPD

$$\Delta r_{spd,Tropo} = zpd_{h,CR} \cdot MF_h + zpd_{w,CR} \cdot MF_w \quad \text{Eq. 16}$$

The key aspect of different mapping functions is their behavior at low elevation angles, i.e. close to the horizon. Regarding space-borne SAR payloads, the full performance products typically cover swaths between 25° to 55° incidence angle (equivalent to 65° to 35° in elevation), which is less demanding than the geodetic techniques which observe at much shallower angles. However, even for SAR, the VMF1 is advised if one aims for the best possible correction of the troposphere. To demonstrate the impact of the mapping on the tropospheric delays, the VMF1 (Eq. 11) was compared to a simple cosine mapping function

$$MF_{h,w} = \frac{1}{\cos(1-E)} \quad \text{Eq. 17}$$

The results are listed in Table 3 and show differences of up to 1 cm in the total tropospheric delay for SAR observations at the edge of the swath (55° incidence angle). This difference would show up as a range dependent distortion when performing an ALE assessment with multiple reflectors across the whole swath and should be avoided when aiming for the best quality in the geometric calibration of a SAR payload.

In conclusion, the VMF1 provides access to reliable tropospheric corrections at a global scale and allows for efficient processing because of the short latency of the products (less than 34 hours). Its limitations are the spatiotemporal resolution (6 hours and 220 by 280 km) and the omission of the horizontal angular dependency in the tropospheric path delays.

Table 3: Comparison of a simple 1/cosine mapping function with the VMF1 across a typical full performance swath of a generic SAR payload (25° to 55° incidence angle). The VMF1 was evaluated for the Wettzell geodetic observatory (latitude = 49° 08' 42", longitude = 12° 52' 33", h = 659m) at 06UTC using the product VMFG_20160101.H06. To compute the slant delays in meters, a hydrostatic ZPD of 2.2 m and a wet ZPD of 0.2 m have been assumed.

Mapping	25°	35°	45°	55°
dry cosine	2.427	2.686	3.111	3.836
dry VMF1	2.427	2.684	3.107	3.826
wet cosine	0.221	0.244	0.283	0.349
wet VMF1	0.221	0.244	0.283	0.348
tot cosine	2.648	2.930	3.394	4.184
tot VFM1	2.647	2.928	3.390	4.174

2.6.1.3. Path delays based on GNSS

The GNSS stations operate at L-band between 1.2 and 1.5 GHz and are sensitive to the tropospheric path delay if processed at zero-difference level, i.e. single receiver precise point positioning (PPP) [22]. This allows for the estimation of high quality tropospheric path delays if the clocks and the orbits are fixed to precisely pre-determined solutions. Under the umbrella of the International GNSS Service (IGS), the US Naval Observatory (USNO) and the Center for Orbit Determination in Europe (CODE) perform such processing on a routine basis for all the receivers of the global IGS network [22][23]. Comparable products for the receivers of the European Reference Network (EUREF) are provided by different analysis centers (ACs) [24]. Figure 18 gives an overview on the IGS and the EUREF stations, but there are most likely a lot more products available, e.g. via the receivers of various national networks. We therefore advise those interested to check with the national GNSS authorities for existing tropospheric products. Since the processing is performed independently for each receiver, the tropospheric path delays should only be used in the receiver's vicinity (< 10 km). The CRs of DLR/TUM are located at geodetic observatories hosting several IGS GNSS receivers which make the GNSS-based tropospheric path delays the first choice for our SAR ALE assessments.

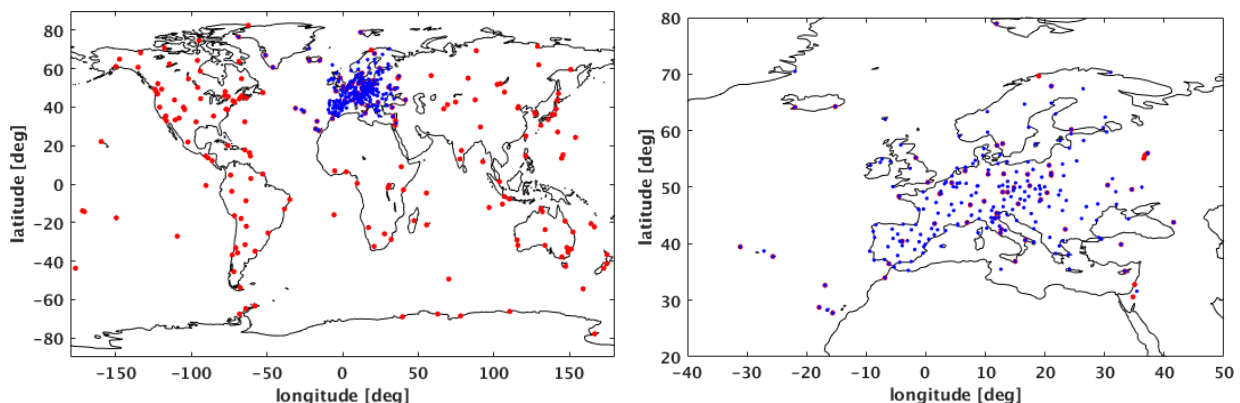


Figure 18: Global IGS station network (red) and regional EUREF network (blue) for which tropospheric path delays are routinely processed. Global view (left) and regional zoom (right).

In general, the GNSS-based tropospheric delays are provided as total delays (the sum of hydrostatic and wet delays) in zenith direction and a horizontal gradient decomposed into its North and East components. Depending on the analysis strategy, the temporal sampling of the total ZPDs and the gradient may vary between 5 minutes and 2 hours. However, it is worth noting that the 5 minute data are not based on independent, epoch-specific solutions; they are linked through temporal parameter constraints in the underlying least squares computation, particularly the gradient. The latency of the products is usually some 1-2 weeks due to the dependency on the final GNSS products (orbits, clocks), but for the sources mentioned above there is also a rapid solution which can be used for near real time applications. Another important aspect is the a priori modelling of the dry path delay using models like VMF₁ or its predecessor, i.e. the Global Mapping Function (GMF). This means that the

actual GNSS-based tropospheric estimates are only the wet delays in the zenith direction, as well as the gradients. The knowledge about the a priori modelling can be used to decompose the total delay of the products into hydrostatic and wet delays, which are required for the vertical transformations (see discussion for the VMF1 in section 2.6.1.2). Table 4 provides a short summary on the products issued by IGS (USNO), CODE and EUREF.

Table 4: Summary on the GNSS-based tropospheric path delay products provided by the International GNSS Service (IGS), the Centre of Orbit Determination in Europe (CODE) and the EUREF Analysis Centers (ACs). The details are given in [22][23][24].

	IGS [†]	CODE	EUREF*
GNSS Network	global IGS	global IGS	regional Europe
Mapping function	GMF	VMF1	VMF1
A-priori hyd. PD	Dry Niell	VMF1	VMF1
Temporal sampling	5 min	2 hours	2 hours
Gradient	yes	yes	yes
Data access	ftp://igs.ensg.ign.fr/pub/igs/products/troposphere/	ftp://ftp.unibe.ch/aiub/CODE/	http://www.epncb.oma.be/_productsservices/troposphere/

[†] Computed by the US Naval Observatory (USNO)

* Several ACs contribute to EUREF ZPDs, the table refers to the BKG solution (Federal Agency for Cartography and Geodesy)

In principle, use of the GNSS-based tropospheric delays in SAR ALE is straightforward as long as the distance of the test site from the station(s) is not too large (naturally, the closer the better) and if one takes the height difference between GNSS receiver and the CR into account. The latter can be based on the methods discussed in the previous section (Eq. 12-Eq. 15), but in this case the total tropospheric delay of the GNSS products needs to be separated into hydrostatic and wet ZPDs. A strict decomposition would require the very model which was used during the GNSS computation, see Table 4, but because the goal is a vertical transformation, we propose a simpler scheme suitable for all products. It is based on the Global Pressure and Temperature model (GPT2) [25] and the equation proposed by Saastamoinen [26].

The GPT2 is an empirical model for the atmospheric state (temperature, pressure, partial water vapor pressure) as well as the corresponding coefficients of the VMF1 (a_h, a_w), and was derived from a 10 year analysis of ECWMF ERA-Interim data. The inputs are station coordinates (longitude, latitude and height). Source codes and the underlying data grid are available from the Technical University of Vienna¹⁶.

¹⁶ <http://ggosatm.hg.tuwien.ac.at/delay.html>

The equation of Saastamoinen is a well-known model for deriving slant-range tropospheric path delay using surface level temperature, pressure, and water vapor pressure. In its original form [26], the equation provides an estimate for the total delay, but in [27] it is shown how the equation can be decomposed into a hydrostatic and wet part. The hydrostatic part is still considered a reliable approximation when used with GTP2 [25], and still serves as a backup in the Bernese GNSS software [15], for instance in case of the Dry Niell model listed in Table 4. For the zenith direction (i.e. $z = 0$), the hydrostatic equation of Saastamoinen is:

$$ZPD_h = \frac{0.002277}{\cos(z)} \cdot (p - 0.155471e - B \tan(z)^2) + \delta R \quad \text{Eq. 18}$$

$$\approx 0.002277 \cdot (p - 0.155471e)$$

where:

p = the pressure in millibar

e = the water vapor pressure in millibar

$B, \delta R$ = tabulated empirical correction terms (not used here)

Combining this model with the height correction scheme enables the computation of tropospheric slant path delays from the GNSS products using the following step by step approach:

1. Download the tropospheric product for the day of the SAR observations (receiver-based solutions of IGS, or network-based solutions of CODE, EUREF; for the network-based solutions, extract the applicable receiver)
2. Load the total ZPD and the gradient time series, and interpolate the values for the time of the SAR observation, e.g. 1D cubic
3. Evaluate the GPT2 for the GNSS receiver coordinates (longitude, latitude, height as annotated in the tropospheric product) to get the pressure and the water vapor pressure at the GNSS receiver for date & time of the SAR observation
4. Convert the output of step 3 to the hydrostatic delay (Eq. 18) and subtract it from the total delay of step 2 to obtain its hydrostatic and a wet components
5. Use the method described in the previous section (Eq. 12-Eq. 15) to correct the zenith delays for the height difference between GNSS receiver and CR

6. Evaluate the GPT2 for the location of the CR (longitude, latitude, height) to get the coefficients (a_h, a_w) and ultimately the VMF1 MF
7. Compute the tropospheric slant path delay, including the gradient contribution, by combining the outputs of steps 2, 5 and 6:

$$\Delta r_{spd,Tropo} = zpd_{h,CR} \cdot MF_h + zpd_{w,CR} \cdot MF_w + grad_{TRO}(A, E) \quad \text{Eq. 19}$$

The gradient term is computed from the direction to SAR satellite (i.e. azimuth A , elevation E , see Appendix I), the hydrostatic mapping function MF_h and the horizontal gradient terms G_E, G_N included in the tropospheric product [28]:

$$grad_{TRO}(A, E) = MF_h \cdot \cot(E) \cdot [G_E \sin(A) + G_N \cos(A)]. \quad \text{Eq. 20}$$

Figure 19 shows a comparison of different GNSS-based tropospheric ZPD products for the day 2016-06-26 for two GNSS receivers at the Wettzell geodetic observatory. All solutions have been corrected for the height of the CR, and the ECMWF-based delay of the VMF1 is included for comparison. The differences between different solutions for the same receiver (WTZR) typically lie within some millimeters, but can be as large as 1 cm during certain epochs. The path delay distributed with the VMF1 captures the overall pattern, but due to the temporal sampling of the underlying ECMWF data it cannot represent the site-specific details, i.e. the deviations may reach several cm. However, such deviations only occur in regions or seasonal periods with high humidity; the dry periods or dry regions are much better represented by the underlying weather models. Regarding the IGS solutions for the different receivers available at Wettzell (WTZR & WTZS), they agree to within 1-2 mm. Our TUM/DLR long term ALE analysis of TSX & TDX at Wettzell, which makes use of the IGS ZPD of all four GNSS receivers to correct for the troposphere, confirms this very high level of consistency.

The gradient components (Figure 19, bottom) reveal the different processing strategies. The constraints used with CODE and EUREF result in a piece-wise daily structure whereas the IGS solution maintains the sub-daily structures. Note that the gradient would also require a transformation to compensate the difference in height, but we are not aware of any method which accomplishes such a correction; the outcome of the gradient is simply added to overall delay. The typical contributions of the gradient are only ca. 1-2 millimeters, but in our measurements series we observed occasional gradient contributions of up to 5 mm. Because of this and the more detailed sampling of the actual path delay, we suggest the IGS products as the primary source for correcting the tropospheric path delays, provided that the CR installation allows for such corrections. Compared with other sources of path delays (VMF1, slant integration), we found the GNSS-based tropospheric corrections to give the best ALE results (see example given in section 4.2).

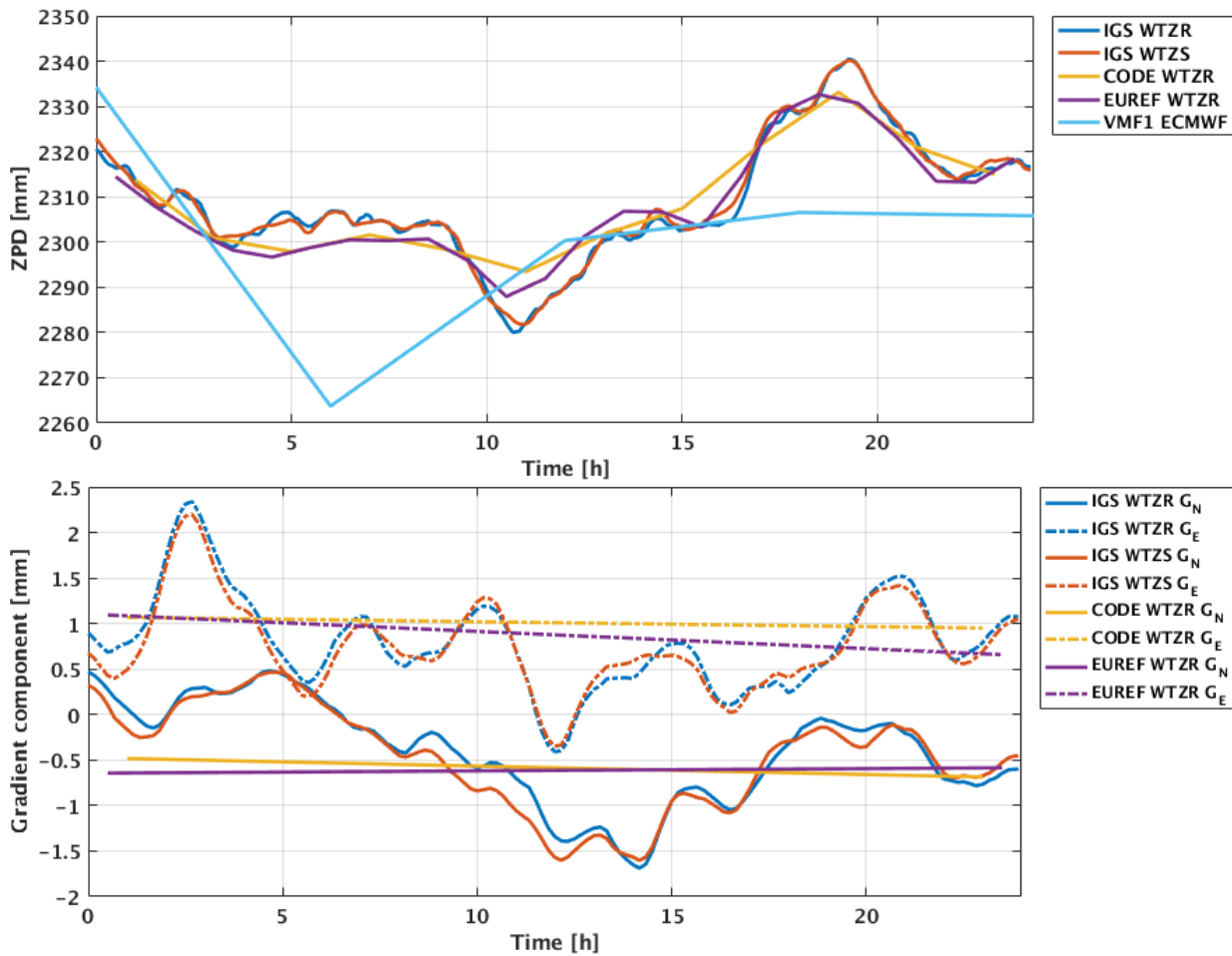


Figure 19: Tropospheric zenith path delay products of 2016 06 26 for two GNSS receivers (WTZR, WTZS) located at Wettzell geodetic observatory. Total tropospheric path delay (top) and gradient components (bottom). The products are provided by the International GNSS Service (IGS), the Centre of Orbit Determination in Europe (CODE), and the European reference GNSS network EUREF, and the Vienna Mapping Function 1 (no gradients, only the ZPD).

2.6.2. Ionosphere

The ionization of the upper part of Earth's atmosphere is driven by solar radiation and causes a frequency dependent path delay for microwave signals. The ionized atmosphere consists of free electrons and charged particles, and its vertical extent ranges approximately from 50 to 1500 km altitude [13]. It can be characterized by the vertical variation of the electron density. The peak concentration occurs around 400 km, but for modelling the correction of microwave signals, these layers are condensed into a single layer containing the total number of electrons. The layer is assigned the altitude of the maximum electron concentration. This method of modelling the ionosphere follows the principles applied in GNSS, which makes it readily applicable to all the SAR payloads (X-band, C-band, L-band) because its fundamental delay equation is given by the signal's frequency. The details are given in [13][30].

Using a frequency-based series expansion of the refractivity and coupling the coefficients of the series to the electron density, one can derive the first order approximation of the ionospheric path delay in slant range [13]:

$$spd_{ion} = \frac{40.3 \cdot 10^{16} s^{-2}}{f^2} \cdot vTEC \cdot MF(z) \quad \text{Eq. 21}$$

where:

f = the carrier frequency of the signal in Hz

$vTEC$ = total number of electrons (vertical) in TEC units (1 TECU = 10^{16} electrons per m^2)

$MF(z)$ = mapping function for conversion into slant delay using the zenith angle z

Higher order correction would require additional terms linked to f^3, f^4, \dots , but these are not discussed here, as even in the case of GNSS (L-band) the use of the f^2 term corrects for more than 99.9 % of the expected delay signal [8]. Note that Eq. 21 provides the path delay as required for the SAR range measurements. To correct the phase, the sign needs to be reversed because in a dispersive medium the phase is advanced (different behavior of group velocity and phase velocity).

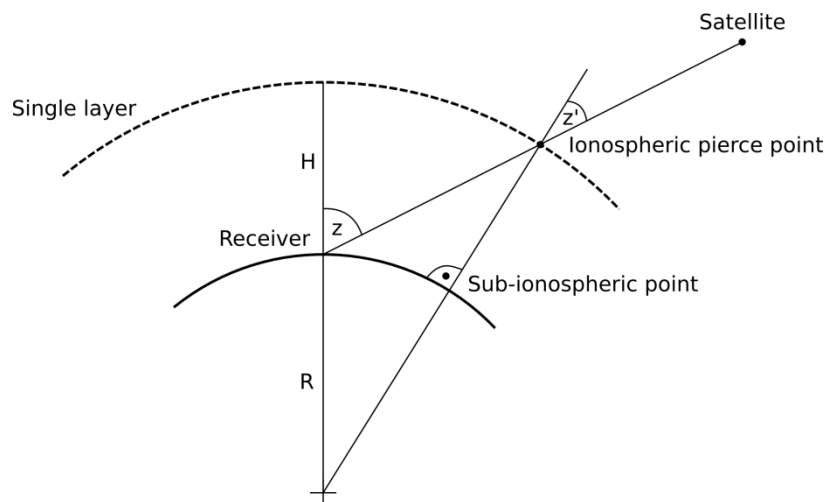


Figure 20: Concept of the ionospheric mapping function assuming a single layer ionospheric model.

The concept of the ionospheric mapping function is illustrated in Figure 20. The $vTEC$ is bound to the ionospheric pierce point (IPP), i.e. the location where the satellite's line of sight intersects with the hypothetical layer holding the total electron distribution. The actual mapping function remains isotropic – it only depends on z – but the $vTEC$ depends on the direction to the satellite through the IPP. This differs from the tropospheric concept which models the vertical path delay right at the location of the receiver. When assuming the $vTEC$ layer as a spherical shell, the mapping function reads [30]:

$$MF(z) = \frac{1}{\sqrt{1 - \left(\frac{R}{R+H} \sin(z)\right)^2}}$$

Eq. 22

with R denoting the radius of the station on the Earth's surface, $R + H$ is the radius of the single layer model, and z denotes the zenith angle. Due to the larger vertical extension of the ionosphere, a single GNSS receiver can probe a much larger region when compared to the troposphere. For instance, a height of 450 km for the single layer model results in an observable cap having a 3000 km diameter. This ability is exploited to generate global ionospheric maps (GIMs) from the GNSS observations of the global IGS network [30].

Several ACs generate GIMs for the IGS which are averaged for the official IGS product [29], but because of the underlying methodology, we have selected the CODE product. Its computation is based on a consistent least squares inversion of daily GNSS observations [23][30] which yields not only the vTEC maps as input for Eq. 21, but also the corresponding variance-covariance information. The latter can be used to quantify the error in the ionospheric path delay correction. The products come in two versions, the final solution termed *codg* and a preliminary near real time solution termed *codr*. Both products can be obtained from the IGS on a daily basis. One file contains 25 grids of global vTEC distribution and the grids have a spatial resolution of longitude 5° by latitude 2.5° (about 580 by 280 km). Note that the temporal sampling of the rapid product is only 2 hours, which is also the case for the final products dated 19th of October 2014 or earlier.

Figure 21 shows three maps (06 UTC, 12 UTC, 18 UTC) of vTEC distribution extracted from the final CODE product of June 1st 2017. The main bulge trails the location of the sun by about two hours, i.e. it is always located around 2PM local time. The RMS maps, also derived from the least squares parameter estimation, are the result of the underlying station distribution (see Figure 21) and may be used to gauge the quality of the ionospheric corrections. SAR satellites (e.g. TerraSAR-X or Sentinel-1) often use sun-synchronous orbits in dusk-dawn configuration, which lead to equator crossings around 6AM and 6PM local time, causing the satellites to cross either ahead of the main bulge or behind the bulge in its tail region. Looking at the maps of Figure 21, the SAR observation of a CR located in central Europe would experience a vTEC of about 15TECU (6AM pass) or 20 TECU (18PM pass). Regarding the SAR bands and a typical swath covering 25 to 55 degrees, a vTEC of 20 TECU leads to ionospheric path delays of up to 0.15 m (X-band) and 11.6 m (L-band), see Table 5. For CR installations in the equator region and depending on the solar activity, the vTEC governing the path delay can reach even larger values of up to 30-40 TECU. Taking into account the strong spatiotemporal variability of the TEC emphasizes the need for a proper consideration of the ionosphere in the ALE. Although for higher frequencies such as X-band the ionospheric range delays are generally much lower than the typical tropospheric delays of 2-4 meters, their impact on the long term variability in X-band SAR acquisitions is very similar. The reason is the seasonal behavior of the TEC and thus of the ionospheric delay, which typically varies from near zero to decimeter-level (mid-latitude to Polar Regions) or decimeter-level in general (tropical regions). For C-band or L-band the ionospheric delay is much more severe,

while the temporal variability of the tropospheric delay – mainly driven by the water vapor – remains at the decimeter-level. Because of their similar temporal variability, the ionosphere and troposphere are similarly important in the ALE analysis, even for X-band missions like TerraSAR-X.

Table 5 also shows the impact of a simple cosine mapping function (Eq. 17) when compared to the single layer mapping function (Eq. 22) associated with the GIM product. Using the simplified mapping function results in errors of up to 1.8 m in L-band, and for X-band the deviation is still as large as 2.8 cm. The RMS of the ν TEC estimate may be as large as 1 TECU for many regions (Figure 21), which causes severe limitations for L-band SAR (1 TECU corresponds to 0.28 m in L-band), while for C-band and X-band this uncertainty corresponds to 0.014 m and 0.004 m, respectively. Therefore, with our present knowledge of the TEC, L-band SAR is clearly limited by the ionosphere.

Table 5: Ionospheric path delay in meters for the different SAR bands assuming typical swath coverage and a ν TEC of 20 TECU. The single layer mapping (SLM) function (Eq. 22) was evaluated for an Earth radius $R = 6378 \text{ km}$ and a shell radius of $R + H = 6821 \text{ km}$, i.e. the single layer model radius used by CODE to generate the GIMs.

Mapping	25°	35°	45°	55°
	X-band (9.7 GHz), e.g. TSX			
Cosine	0.095	0.105	0.121	0.149
SLM	0.110	0.126	0.147	0.177
	C-band (5.4 GHz), e.g. Sentinel-1			
Cosine	0.305	0.337	0.391	0.482
SLM	0.355	0.406	0.475	0.571
	L-band (1.2 GHz), e.g. ALOS-2			
Cosine	6.176	6.833	7.916	9.758
SLM	7.197	8.220	9.616	11.570

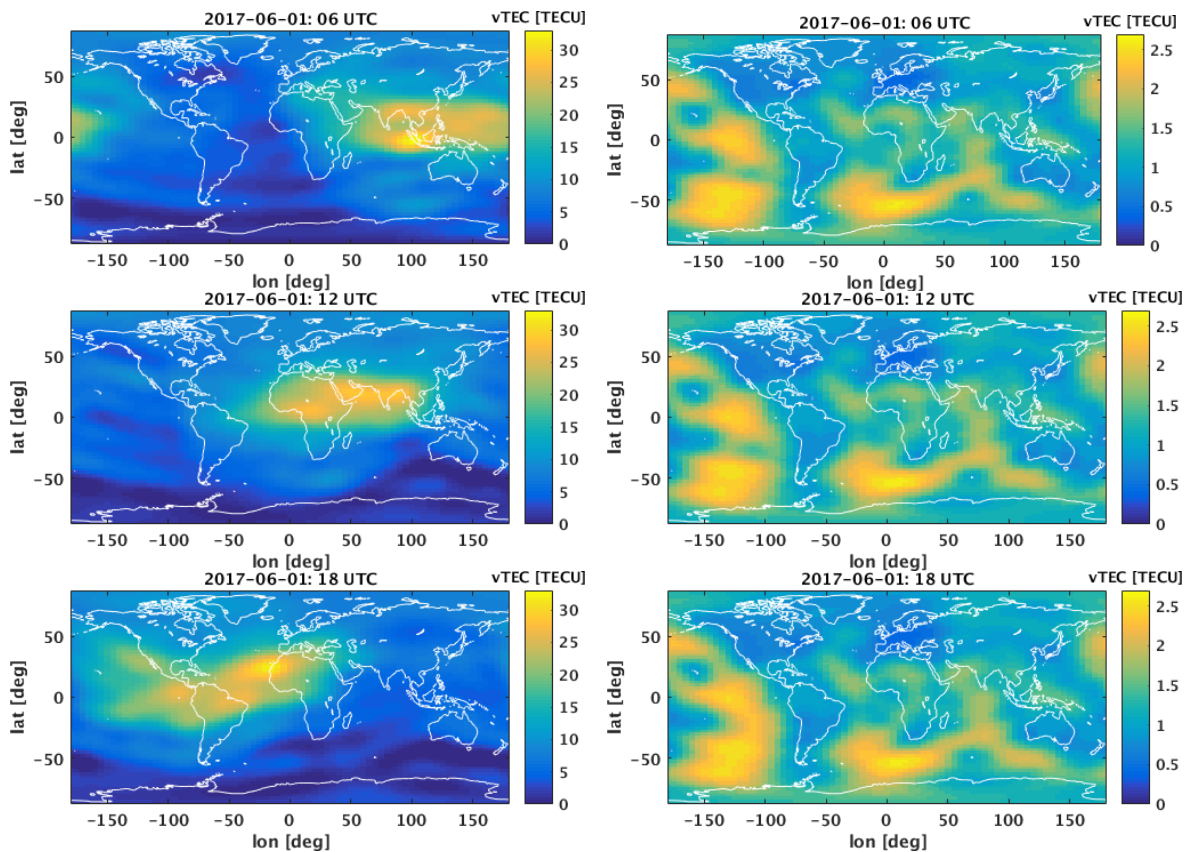


Figure 21: Global vTEC distribution based on the CODE global ionospheric map product for the 1st of June 2017. vTEC map (left) and corresponding RMS map (right).

An additional important consideration is the fact that SAR satellites usually orbit within the upper region of the ionosphere. Strictly speaking, resolving this would require the 3-D distribution of the free electrons and the integration of the electrons along the observed slant-range path. To our knowledge, there is not yet any global model which can provide such information with sufficient quality. We decided to opt for an empirical approach to bypass this situation to some degree. The average orbit height of TerraSAR-X is 512 km and the analysis of the electron density versus altitude using the International Reference Ionosphere model (IRI-2007) indicates that approximately 75% of the electrons are below TerraSAR-X orbit level [31]. The value was determined for the location of Wettzell and we are aware that this only represents the situation at mid-latitudes. However, any bias introduced by this assumption will be captured by the mean values of the range ALE measurements, which may be seen as a sensor's geometric calibration value. Such dependencies are inevitable when performing geometric calibration and any substantial change in the process would require the re-computation of the calibration constants, as was already discussed in section 2.5.4. Once there is a superior method for resolving this problem, the ionospheric corrections should be modified accordingly, but for now we suggest the use of constant empirical factors to rescale the ionospheric path delay for a dedicated SAR mission, see Table 6. The factor of 90% for Sentinel is only a first order extrapolation based on the value found for TerraSAR-X.

Table 6: Approximate scaling factors for the ionospheric path delay considering the orbit altitude of different SAR missions

Mission	Average Orbit height	Scaling factor
TerraSAR-X	515 km	0.75
Sentinel-1	693 km	0.90

In summary, the computation of the ionospheric correction using the GIMs requires the following steps:

1. Download the CODE ionospheric GIM product for the day of the SAR observations. Depending on the interpolation method in step 3, one would additionally require the product(s) for the previous or the next days if the SAR product was acquired near midnight.
2. Compute the IPP by intersecting the spherical shell of the vTEC model with the line defined by the CR-coordinates and the satellite's zero Doppler position, and convert the IPP coordinates to latitude and longitude (Eq. 36). The radius of the geocentric sphere is 6821 km (see the header of the CODE products).
3. Interpolate the vTEC at the IPP for the time of the SAR observation using the GIMs and a trilinear or tri-cubic interpolation method (latitude, longitude, time). If the vTEC quality is of interest, repeat the process for the RMS maps.
4. Compute the single layer mapping function (Eq. 22) for the zero-Doppler geometry. The radius R is the norm of the CR coordinate vector, the $R + H$ is the radius of the VTEC single layer model, i.e. 6821 km.
5. Evaluate Eq. 21 using the outputs of step 3 and step 4 to obtain the ionospheric slant path delay. Rescale the result to account for the orbit height (Table 6).

2.7. Modelling of Expected Image Coordinates

The expected range and azimuth timings of the ALE analysis are inferred from the range-Doppler equations in zero Doppler geometry as introduced in section 2.3. This requires the satellite trajectory from the product annotation and the instantaneous ITRF position of the CR. The latter is computed using the conventional geodynamic models that are part of the ITRF definitions. Starting from the CR reference coordinate (position, linear displacement, frame epoch) stemming from survey of the ground installation [RD1], the instantaneous CR coordinate can be computed by considering the epoch difference (linear displacement), and adding the deformation of the geodynamic effects. This procedure is documented in the two subsequent sections 2.7.1 and 2.7.2. Resolving the range-Doppler equation for the instantaneous CR coordinate requires the numerical computation of the sensor' zero-Doppler state vector (section 2.7.3). Along with the range-Doppler equations this finally yields the sought for expected range and azimuth timings, which is addressed in the final section 2.7.4.

2.7.1. Geodynamics

During the determination of the ITRF, the effects of the solid Earth causing displacements of the reference stations are removed, i.e. the frame is defined through so called regularized station coordinates representing the average state of the Earth's crust [8], see section 2.4. If one determines the CR reference coordinates in the ITRF, either by differential GNSS or by on-site terrestrial survey and its conversion to ITRF, these coordinates too refer to this average Earth surface. On the other hand, observations made by satellites to reference markers located on the ground (CRs, GNSS receivers, ...) refer to the dynamic state of the surface at the time of observation, illustrating the purpose of the ITRF as a global reference to allow the geometrical measurement of the Earth. Consequently, we can model the instantaneous position of the CR during a SAR acquisition by adding the displacements computed from the conventional dynamic models for the date and time of SAR observation. These models encompass all the tidal related effects affecting the Earth's crust (solid Earth, ocean, atmosphere) as well as secondary effects related to the dynamics of the Earth's rotational axis, see the overview given in Table 7. In total these effects add up to displacements of some 25 cm in the vertical direction and about 6 cm in the horizontal direction. The details are described in the IERS conventions and the following sections are a summary based on chapter 7 of the conventions and the implementations at TUM/DLR. Note that there are also non-tidal effects which are not discussed here in detail, because even with the release and adoption of ITRF 2014, these effects are still not part of the IERS conventions. Presently, the estimation of inter-annual signals has proven superior to the a-priori correction of non-tidal signals and further tests are needed to decide which models should be included in the data reduction of the future ITRF [33].

With the exception of the ocean loading, all effects are either given as continuous models depending on the station longitude and latitude, or as global grids allowing for the interpolation of an arbitrary station. The displacement results are usually computed in the local North, East, and up system and

may be summarized in a vector $[\Delta_n \ \Delta_e \ \Delta_u]^T$. Its addition to the CR reference coordinates requires the transformation for the global ITRF axes given by [13]:

$$\Delta X_i = \mathbf{R}(\varphi, \lambda)^T \cdot [\Delta_n \ \Delta_e \ \Delta_u]^T \quad \text{Eq. 23}$$

with ΔX_i denoting the displacement expressed in global ITRF for the i -th effect, and the $\mathbf{R}(\varphi, \lambda)^T$ is the rotation matrix depending performing the transformation. It depends on the latitude φ and the longitude λ of the CR. More details on this procedure as well as the computation of \mathbf{R} are given in the appendix. Note that all the results are computed such that they have to be *added* to the ITRF reference coordinates to obtain the instantaneous position of the CR.

Table 7: Magnitude of the solid Earth displacement effects based on the geodynamic models listed in the IERS conventions 2010 [8]. The non-tidal atmosphere and the secular trends are not part of the conventions; see the discussion in the text.

Effect	Horizontal [mm]	Vertical [mm]
Solid Earth tides	± 50.0	± 200.0
Ocean loading	± 10.0	± 50.0
Pole tides	± 1.5	± 6.0
Atmospheric tidal loading	± 0.2	± 1.5
Ocean pole tide loading	± 0.3	± 0.5
Atmospheric non-tidal loading	± 3.0	± 15.0
Secular trends	up to 100 mm/y	up to 15 mm/y

2.7.1.1. Solid Earth Tides

The solid Earth tides (SETs) are the uplift of the Earth crust which is caused by the gravitational force of Sun and Moon. The signal typically varies between -20 cm and +20 cm in the vertical direction but there is also a significant horizontal displacement which can reach up to 5 cm. It is the largest of all the solid Earth displacement effects, see the comparative listing given in Table 7, and together with atmospheric path delay the SETs may be considered as the minimum requirement when performing the SAR ALE analysis. The SET computation is driven by date and time, and requires the corresponding constellation of Sun and Moon as seen from the Earth (i.e. in the ITRF), as well as a geodynamic model describing the deformation ability of the solid Earth. The model and how to implement it is covered in detail by the IERS conventions [8].

The model is based on the Love and Shida numbers [8] (for their concept and the numerical values see [54]) holding the information about the Earth's deformation ability, which is combined with the different diurnal and semi-diurnal tidal frequencies. A general computational scheme is shown in Fig-

ure 22. Starting from the position of a CR and the time of the acquisition, one computes the different tidal constituents using the nominal frequency values associated with the deformation numbers (step 1), and corrects these results for the actual frequencies (step 2). The summation of both results ensures the modelling of all tidal displacement contributions which are larger than 1 mm (step 3). The final result is the displacement $[\Delta x \ \Delta y \ \Delta z]_{SET}^T$ in meters which is already expressed the global ITRF. Note that the permanent tidal deformation also included in the model is not required because per definition it is excluded from the ITRF and the geodetic observation techniques. Strictly speaking, the ITRF coordinates are so-called *conventional tide free* coordinates.

Regarding the computation of the position vectors of Sun and Moon, the IERS standard are the D421 planetary ephemerides issued by NASA Jet Propulsion Laboratory (JPL). A straight forward application of these ephemerides is given by the NASA's SPICE toolkit¹⁷, which is available as an Application Programming Interface (API) supporting several programming languages. Using these routines provides access to the Earth's orbit around the Sun, as well as the Moon's orbit around the Earth, and the output may be returned directly in the ITRF, as required for the SET computation. Note that SPICE only supports the ITRF 93 but here the ITRF updates are negligible due to the large distances and the uncertainties involved.

For the processing of the TerraSAR-X ALE, TUM/DLR have implemented the conventions with the SPICE toolkit in the background, but for users looking for a ready-to-use program there exists an open source freeware named *solid.exe* created by D. Milbert [37]. Its implementation is based on the former IERS 2003 conventions, which should not make any difference as the model has remained unchanged, but the computation of Sun and Moon has been simplified. Users should also be aware that the output is given in the local horizontal system requiring the transformation given by Eq. 23, and that the time of computation is GPS time. We found the differences to our implementations to be in the order of 1 mm, which makes *solid.exe* a useful alternative for all but the most precise requirements.

Figure 23 shows two global results of the SETs for different dates with the displacements given in North, East and up. The first date (2017-06-09) corresponds to a full Moon constellation for which the alignment of Sun and Moon results in the largest uplift signals of +/- 20 cm. Note that this figure is identical to a new Moon constellation. In the case of sun-synchronous dusk-dawn orbits, a satellite is located about 90 degrees with respect to Sun direction, hence the ground tracks closely follows the -20 cm minimum band visible in the up component. Therefore, a TerraSAR-X or Sentinel-1 acquisition in Europe occurring around 18:00 UTC would experience the full -20 cm minimum vertical signal along

¹⁷ <https://naif.jpl.nasa.gov/naif/toolkit.html>

with several cm of horizontal displacement. The second date (2017-06-17) is a half Moon constellation causing an overall dampening of the signal, but now the Moon is in phase with the SAR satellites, resulting in the maximum vertical signal of about +20 cm. Consequently, the entire SET signal bandwidth is mapped into a long-term ALE analysis which underlines the importance of its correction.

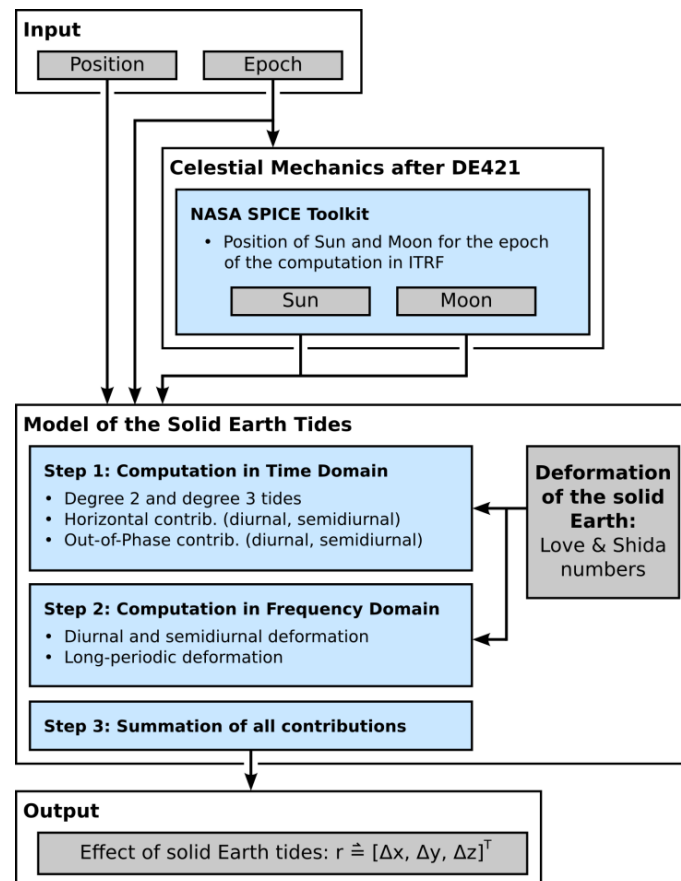


Figure 22: Computational scheme of the solid Earth tides following the descriptions given in the IERS conventions 2010 [8].

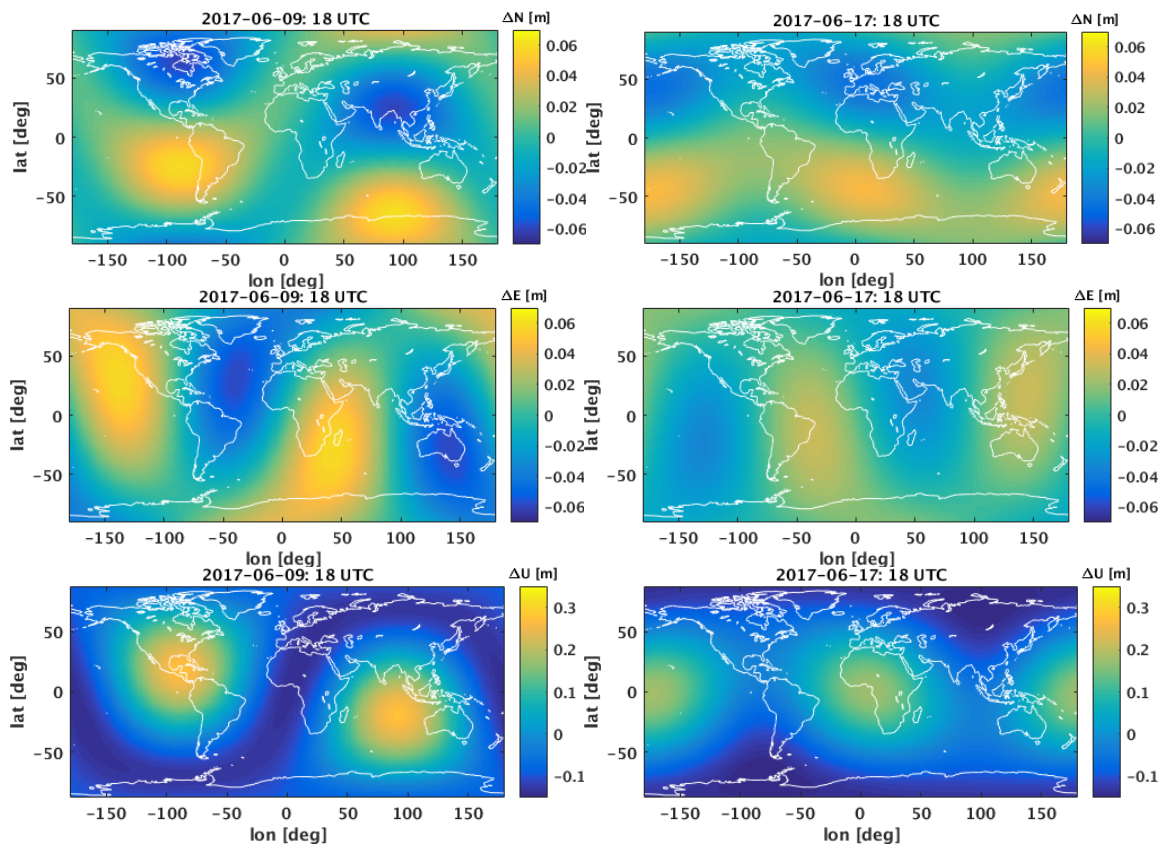


Figure 23: Global solid Earth tide displacement at 18:00 UTC in North (top), East (mid) and up (bottom) for the full Moon constellation on 2017-06-09 (left) and the half Moon constellation 2017-06-17 (right).

2.7.1.2. Other Geodynamic Effects

Besides the SETs, there are the effects of ocean loading, pole tides, atmospheric tidal loading, and ocean pole tide loading, which are all part of the IERS conventions listing the periodic signals that exceed the 1 mm level. The Table 7 provides a general overview on the typical magnitudes in horizontal and vertical direction, and Figure 24 illustrates their global up component for the day 2017-09-06 at 18:00 UTC.

2.7.1.2.1. Ocean loading

The ocean loading (OL) is the secondary effect of the tidal water re-distribution pressing against the coastlines of the continents and islands. Naturally, the effect is most pronounced for near coastal CR installation, for instance the TUM/DLR CRs at GARS O'Higgins at the Antarctic Peninsula. Eliminating the effect requires a model of the ocean tides and the deformation pattern derived from the computation of the coastline response using a weighting function (i.e. Green's function). To allow a computation by the average user, the problem has been decomposed into a service for requesting the site specific dynamic parameters and a routine for converting these parameters into the actual displacement in local north, east, and height. This has the advantage of a relatively easy application for dedi-

cated sites, but it poses a limitation if one is interested in the global representation, e.g. when the correction should be annotated to the SAR products [41]. Regarding the ALE analysis and specific test sites, this is not a problem and the user may simply request the deformation parameters by submitting the coordinates to the service maintained by the Onsala Space Observatory¹⁸. There are several ocean tidal models to choose from, but we suggest the FES2004 by Lyard et al. [39], which is also the default selection in the Bernese GNSS software [15]. The center of mass correction is not required. The output format has to be in the so-called BLQ format in order to use the FORTRAN routine *HAR-DISP.FOR*, available as a supplement to the IERS conventions [8]. For CR installations in the vicinity of IGS station, there exists the *FES2004.BLQ* file that contains the site specific deformation parameters of every IGS station. The file can be downloaded from the user data server of the Bernese software¹⁹. Once the deformation parameters have been derived for a specific site, the effect of ocean loading can be computed for any date and time.

Figure 24a displays the vertical ocean loading result for the IGS stations included in the *FES2004.BLQ* file for the day 2017-06-09 at 18:00 UTC. The loading shows a large spatial variation because of the complicated tidal pattern and the water mass interaction with the highly irregular coastlines. For Europe, the largest impact is observed north-west of France (Brest), where the vertical signal may be as large as ± 4 cm, and the horizontal deformation can reach 1-2 cm. In other regions like Alaska or islands like Hawaii the impact is even larger (up to 5 cm).

2.7.1.2.2. Atmospheric tidal loading

The daily heating of the atmosphere by the sun results in pressure variations which in turn cause displacements referred to as *atmospheric tides* or atmospheric tidal loading (ATL). The most important harmonics, i.e. the diurnal tides S_1 and the semidiurnal tides S_2 , are covered by the model of Ray and Ponte (RP03) [8]. The resolution of the model is 1 degree (equivalent to 110 km) and it is distributed as 12 global grids holding the amplitude values of the sine and cosine harmonics in north, east, and height, and for both the diurnal and the semi-diurnal components²⁰. Interpolation of these grids for the latitude and longitude of a CR yields the applicable amplitude coefficients which are combined according to the equations given in the IERS conventions. The vertical displacement can reach the millimeter level, see Figure 24c, whereas the horizontal displacement is about a factor of 10 smaller. Therefore, this effect is of less importance for the SAR ALE analysis.

¹⁸ <http://holt.oso.chalmers.se/loading/>

¹⁹ <ftp://ftp.unibe.ch/aiub/BSWUSER52/STA/>

²⁰ <http://geophy.uni.lu/ggfc-about/tide-loading-calculator.html>

2.7.1.2.3. Pole tides

The so-called pole tides (PT) are the consequence of the changes in the Earth's rotation axis affecting the Earth's centrifugal potential. They are modeled through the deviation of the Earth's mean rotation pole from the actual rotation pole, which is dominated by a free oscillation with a period of about 435 days (Chandler wobble) and an annual oscillation forced by the seasonal displacement of air and water masses. This means that the pole tides are not a diurnal or semidiurnal effect but that the pattern shown in Figure 24b moves eastward with rate of approximately 0.8 degrees per day. During a long-term ALE analysis, one captures the full signal having an impact of ± 6 mm, which makes the pole tides a significant effect when aiming for the best possible ALE results. The state of the rotational pole is published and constantly updated by the IERS²¹, with the IAU2000 *finals.data* holding the latest version being in line with the 2010 conventions. Combining this state with the model of the mean rotation pole described in the conventions enables a relatively straightforward computation of the pole tide effect.

2.7.1.2.4. Ocean pole tide loading

The ocean pole tide loading (OPTL) is a secondary effect of the pole tides leading to variation in the ocean's equilibrium state and thus to small loading effects that interact with the sea floor and the coast line. The effect's pattern is an inverse of the pole tides, see Figure 24d, but the magnitude hardly exceeds the 1 mm level. For the continental land, the impact is damped even further. Thus, in our analysis the OPTL was only included for completeness. Omitting this effect in the SAR ALE analysis is fully justified since the best possible ranging accuracy presently achieved by the TerraSAR-X mission is about 1-2 cm. The computation shares many similarities with the pole tides and the surface response is available through pre-computed grids having a resolution of 0.5 by 0.5 degrees (about 55 by 55 km), which enable the interpolation for the ALE test site.

²¹ <https://www.iers.org/IERS/EN/DataProducts/EarthOrientationData/eop.html>

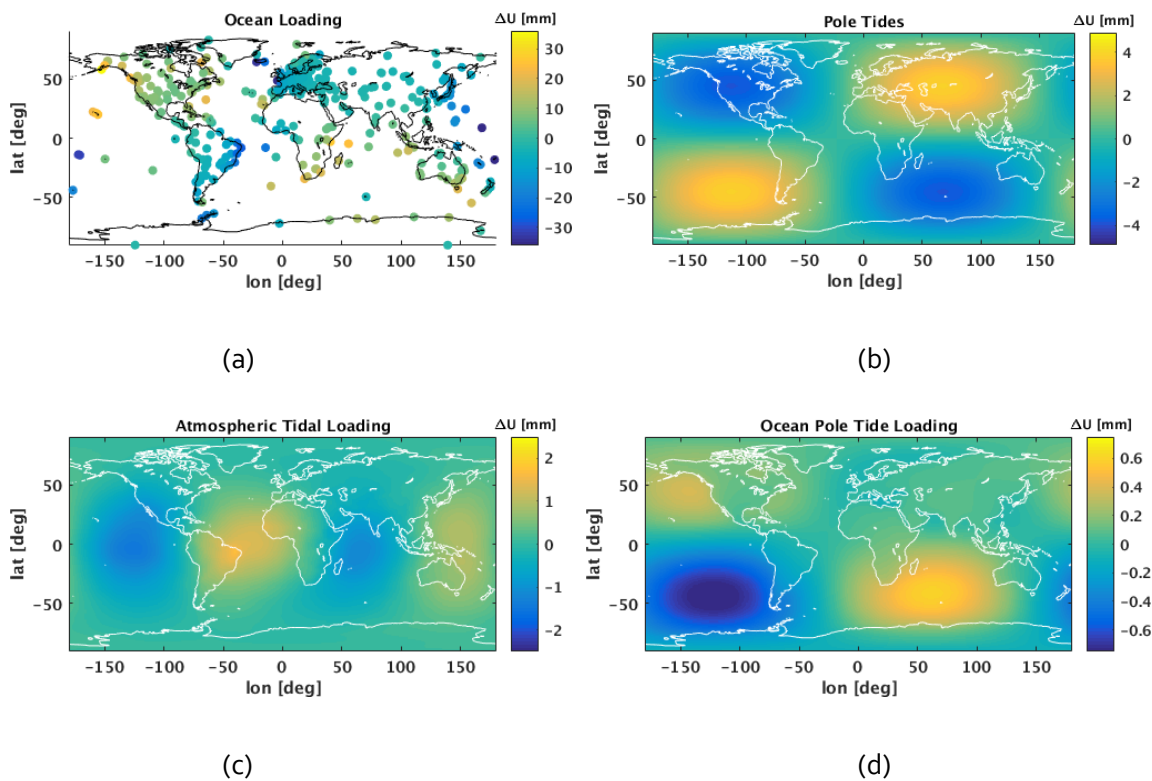


Figure 24: Vertical displacement signal for the ocean loading (a), the pole tides (b), the atmospheric tidal loading (c) and the ocean pole tide loading (d) for the day 2017-06-09 at 18:00 UTC.

2.7.1.2.5. Atmospheric non-tidal loading

In addition to the tidal driven effects discussed above, there are also non-tidal effects related to the atmosphere, the ocean and the hydrology that may lead to local site specific deformations. In the context of the ITRF determination, the reduction of these effects is still in debate and the latest tests performed during the processing of the ITRF₂₀₁₄ solution showed that the estimation of periodic signals in the station coordinates is superior to the a priori reduction using an atmospheric loading model [33]. Hence we suggest to follow the recommendation given in the IERS conventions which is not to include such signals as a standard effect, but to evaluate them on an experimental basis.

For the atmospheric non-tidal loading induced by the pressure changes of the local weather, there is a loading service operated by NASA²² that distributes displacement series for the IGS stations and as

²² <https://gemini.gsfc.nasa.gov/aplo/aplo.html>

global grids. The details are given in [38]. The impact is in the order of 1-2 cm as listed in Table 7. For our ALE analysis of TSX1 and TDX1 using the CRs installed at geodetic observatories, we achieved a small improvement when introducing the displacements extracted from the corresponding IGS station series.

2.7.1.2.6. Secular trends

Long-term trends are not displacements in the sense of the IERS conventions but they are crucial for the ALE processing. The stations defining the ITRF are bound to the tectonic plates and undergo the secular motion related to plate tectonics. There are many other secular motions like post glacial rebound or irregular deformations at rift regions like the San Andreas Fault. The rates can become as high as 10 cm/y, see Figure 25. These deformations are part of the ITRF solution and are estimated during the processing to obtain the continuous realization of the frame, i.e. the defining station coordinates have to be known for every frame epoch. Thus in their functionality as ITRF reference markers, CRs also have an epoch and at least require the linear deformation corresponding to plate tectonics, which was already discussed in [RD1]. Installations at geodetic reference stations or close to it have the advantage that the true velocity is precisely known through the ITRF solution, and discontinuities related to Earthquakes are taken into account by piece wise linear modelling. This information is part of the so-called *solution independent exchange format* (SINEX) files or the easier to handle *sets of station coordinates* (SSC) files holding the velocity solutions of the whole ITRF station network. Figure 25 visualizes the global velocity field of the GNSS station (IGS14.SSC) contributing to the ITRF2014 solution. These files are published with the ITRF release and the latest version can be found at the ITRF website²³. For other locations, the secular displacement may be interpolated from the ITRF station velocity field but one has to take care of the tectonic plate boundaries when selecting the station, see Figure 25. Moreover, there are site specific effects like uplifts which may not apply to the location of the CR installation. Errors in the CR velocity will show up as a residual trend in the long-term ALE analysis, provided that the CR installation itself is stable and that the SAR payload allows for cm-level accuracy. On the other hand, one might argue that with the high-quality processing of absolute range and azimuth, SAR becomes sensitive to these signals, which is of course a benefit of the ALE calibration, but when performing the ALE assessment such effects should be avoided.

²³ http://itrf.ign.fr/ITRF_solutions/2014/

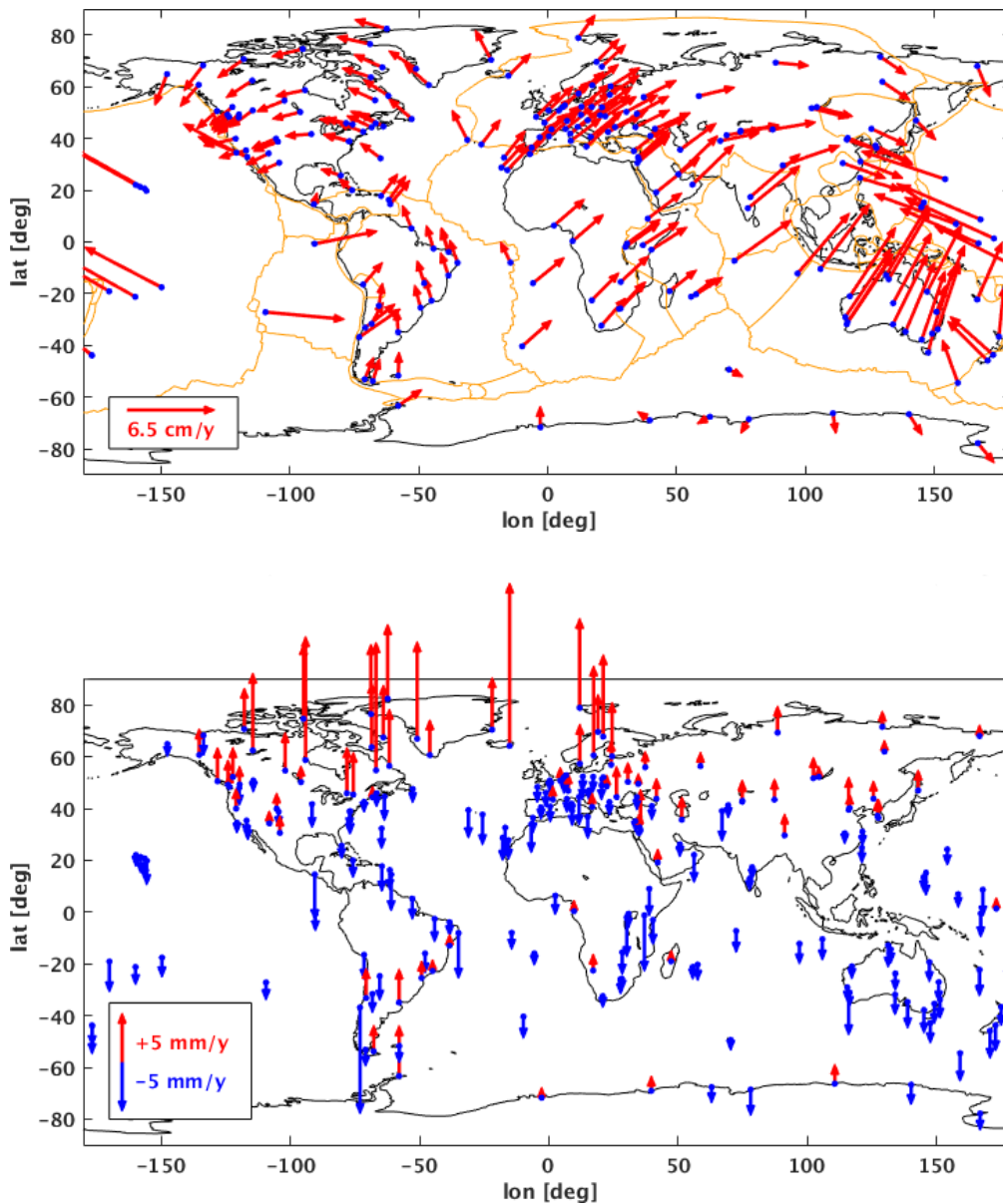


Figure 25: ITRF2014 GNSS velocity field from the IGS14 solution. Horizontal field (top) and vertical field (bottom). The plate boundaries are from the tectonic model MORVEL56 [40].

2.7.2. Definition of Object Position in ITRF

From the terrestrial survey of the CRs according to [RD1] we obtain the reference coordinates in the ITRF as it was already mentioned in chapter 1. The reference station protocol, see Figure 14 in [RD1] holds the CR coordinates $X_{CR} = [x \ y \ z]^T$ in meters that belong to a dedicated frame epoch t_{e0} . Preferably, the secular linear displacement \dot{X}_{ITRF} is already part of the protocol; otherwise it may be inferred from the velocity fields as discussed in the previous section. Starting from the reference coordinate, the instantaneous dynamic position of the CR is established by transforming the coordinate

to the epoch of the SAR acquisition (linear displacement), and by adding the geodynamic effects computed for the time of the acquisition. These instantaneous coordinates will be used to predict the SAR range and azimuth for the final comparison.

For the date and time of each SAR acquisition, one has to execute the following steps

1. Conversion of the CR reference coordinates $X_{CR}(t_{e0})$ to latitude and longitude using Eq. 36. Along with the date and time of the SAR acquisition, the latitude and longitude are the inputs for the geodynamic models. This conversion is only needed once.
2. Transforming the reference coordinate to the actual epoch ($t = t_{Img0}$) of the SAR acquisition by considering the linear displacement:

$$\mathbf{X}_{CR}(t) = \mathbf{X}_{CR}(t_{e0}) + \dot{\mathbf{X}}_{ITRF} \cdot (t - t_{e0}) \quad \text{Eq. 24}$$

1. Evaluating the geodynamic effects for the acquisition epoch using the longitude and latitude of step 1. Be aware that the OL, the ATL, the PT and the OPTL require the transformation from the local North, East, and up to the global x , y , and z ; see Eq. 23.
2. Addition of all effects to the CR coordinate of step 2 to obtain the true reference position $\hat{\mathbf{X}}_{CR}(t)$ of each SAR acquisition ($t=t_{Img0}$).

$$\hat{\mathbf{X}}_{CR}(t) = \mathbf{X}_{CR}(t) + \Delta\mathbf{X}_{SET}(t) + \Delta\mathbf{X}_{OL}(t) + \Delta\mathbf{X}_{ATL}(t) + \Delta\mathbf{X}_{PT}(t) + \Delta\mathbf{X}_{OPTL}(t). \quad \text{Eq. 25}$$

2.7.3. Definition of SAR Sensor in ITRF

The state vectors annotated in the TerraSAR-X SAR products and Sentinel-1 are already given in ITRF. The state vectors in both missions are annotated in a sampling grid of 10 seconds. State vectors in between the sampling points are in need of interpolation. The interpolated state vectors can directly be used to solve the zero Doppler equations in order to solve for the image coordinates of the target. As already described in section 2.5.2, for TerraSAR-X the position of the SAR antenna is annotated while for Sentinel-1 the satellite center of mass is provided. This will lead to elevation dependent range offsets, see section 2.5.2.

For the interpolation of a state vector at the instant of interest, Chebyshev polynomials are recommended in [53]. Chebyshev polynomials are defined by the recurrence relation

$$T_0(\tau) = 1 \quad \text{Eq. 26}$$

$$T_1(\tau) = \tau$$

$$T_{i+1}(\tau) = 2\tau \cdot T_i(\tau) - T_{i-1}(\tau) \quad \text{for } i \geq 1$$

Chebyshev series of type

$$f(t) = \sum_{i=0}^n c_i T_i(\tau) \quad \text{with } \tau = 2 \cdot \frac{t-t_a}{t_b-t_a} - 1 \quad \text{Eq. 27}$$

approximate the vector components of satellite position (x_S, y_S, z_S) and velocity ($\dot{x}_S, \dot{y}_S, \dot{z}_S$). In Eq. 27, t_a and t_b denote start and end of the time interval, the approximation is valid for. The fit of Chebyshev coefficients c_i requires the annotated state vectors at $n+1$ adjacent sampling points. Chebyshev polynomials of order 7 turned out to be an adequate choice for orbit interpolation aiming at an accuracy level of 1 cm. Thus, the polynomial fit requires 8 annotated state vectors. With respect to interpolation accuracy, it is most adequate to choose these state vectors centered on the instant of interest, i.e. 4 state vectors before and 4 state vectors after the expected zero-Doppler azimuth. The measured azimuth from with the PTA (section 2.5.5) may serve as an indicator to select the state vectors.

While satellite position and velocity are given by the annotated state vectors, the approximate satellite acceleration has to be derived from the velocity vectors. The first time derivate of Eq. 27, required for this purpose, is given by

$$\dot{f}(t) = \frac{2}{t_b-t_a} \sum_{i=0}^{n-1} d_i T_i(\tau) \quad \text{Eq. 28}$$

where coefficients d_i results from the recurrence relation

$$d_{n+1} = 0 \quad \text{Eq. 29}$$

$$d_n = 0$$

$$d_i = d_{i+2} + 2 \cdot (i + 1) \cdot c_{i+1} \quad \text{for } i = n - 1, n - 2, \dots, 1$$

$$d_0 = \frac{d_2}{2} + c_1.$$

2.7.4. Estimation of Expected Radar Times

Given the position of the object on ground (see section 2.7.2) and the state vectors of the satellite trajectory (see section 2.7.3), both consistently in ITRF, we first compute the expected azimuth time $t_{e,CR}$ of the closest approach iteratively. As soon as an appropriate approximate for $t_{e,CR}$ is given in this way, the expected range time results according to Eq. 5 by

$$\tau_{e,CR} = \frac{2 \cdot \|\mathbf{X}_S(t_{e,CR}) - \hat{\mathbf{X}}_{CR}\|}{c_0}. \quad \text{Eq. 30}$$

According to zero Doppler condition Eq. 4, the velocity vector $\dot{\mathbf{X}}_S(t_{CR})$ at the instant of closest approach is perpendicular to the line of sight, characterized by the distance vector $\mathbf{X}_S(t_{CR}) - \hat{\mathbf{X}}_{CR}$ between satellite and target. Before and after this instant, the angle between both vectors deviates from 90° . Over a long time interval²⁴, this angular deviation is monotonically decreasing while the satellite is approaching and monotonically increasing when the satellite departs. Consequently, the scalar product

$$f(t) = \dot{\mathbf{X}}_S(t) \cdot (\mathbf{X}_S(t) - \hat{\mathbf{X}}_{CR}) \quad \text{Eq. 31}$$

is an appropriate optimization criterion in a Gauss-Newton optimization of $t_{e,CR}$. The Gauss-Newton recurrence relation

$$t_{e,CR}^{(i+1)} = t_{e,CR}^{(i)} - \frac{f(t_{e,CR}^{(i)})}{\dot{f}(t_{e,CR}^{(i)})} \quad \text{Eq. 32}$$

requires the knowledge of the first temporal derivative of $f(t)$, given by

$$\dot{f}(t) = \ddot{\mathbf{X}}_S(t) \cdot (\mathbf{X}_S(t) - \hat{\mathbf{X}}_{CR}) + \|\dot{\mathbf{X}}_S(t)\|^2. \quad \text{Eq. 33}$$

In each iteration step, we compute the satellite's position $\mathbf{X}_S(t_{e,CR}^{(i)})$, velocity $\dot{\mathbf{X}}_S(t_{e,CR}^{(i)})$ and acceleration $\ddot{\mathbf{X}}_S(t_{e,CR}^{(i)})$ according to section 2.7.3 and inserted these vectors in Eq. 31 and Eq. 33. The stop criterion for this recurrence is given by the comparison of $f(t_{e,CR}^{(i)})$ against a predefined lower limit, e.g. 10^{-9} .

²⁴ To be exact: as long as the temporal deviation from the instant of closest approach is small against the satellite's orbit period.

3. Comparison and Analysis

The results of section 2.5 (observed image timing coordinates), section 2.6 (path delay corrections) and section 2.7 (predicted timing coordinates) form the basis of the ALE analysis. The easiest method to do the analysis is a date by date tabulation of all the values in a spreadsheet, which may be separated according to the different pass geometries involved. This allows the comparison by simple addition and subtraction of the individual columns, see TSX example in Table 8 and Table 9. Keep in mind that the atmospheric path delays have to be subtracted from the SAR range-time observations in order to correct for the reduced light velocity. For each pass geometry, acquired at a test site, we recommend small stacks of at least 10 repeated acquisitions to generate the statistics, but some 20 to 30 acquisitions are advised for a more reliable ALE analysis.

When comparing the two results, we compute the difference of *image timings minus the predicted timings*. The corresponding equations for azimuth and range read

$$\Delta Azimuth = (t_{m,CR} - t_{e,CR})v_{beam} \quad \text{Eq. 34}$$

$$\Delta Range = \frac{\tau_{m,CR} - \tau_{e,CR}}{2} c - \Delta r_{spd,Tropo} - \Delta r_{spd,Iono} \quad \text{Eq. 35}$$

Table 8: Excerpt of the tabulated input for the TerraSAR-X ALE analysis in Metsähovi, Finland. SoD refers to seconds of day.

acquisition [date]	$t_{m,CR}$ [SoD]	$\tau_{m,CR}$ [s]	$\Delta r_{spd,Tropo}$ [s]	$\Delta r_{spd,Iono}$ [s]	$t_{e,CR}$ [SoD]	$\tau_{e,CR}$ [s]
2013-12-12	17862.2915822	0.003833137266	1.7961E-08	9.81E-11	17862.2915910	0.003833121185
2013-12-23	17861.4919671	0.003833473478	1.7239E-08	7.67E-11	17861.4919757	0.003833458238
2014-04-12	17861.1333844	0.003832477082	1.7489E-08	2.76E-10	17861.1333921	0.003832461378
...

Table 9: Absolute Location Error: comparison of observed and predicted SAR timings and conversion to units of meters for the data shown in Table 8.

acquisition [date]	Δt [s]	$\Delta \tau$ [s]	v_{beam} [m/s]	c [m/s]	$\Delta Azimuth$ [m]	$\Delta Range$ [m]
2013-12-12	-8.828E-06	-1.9781E-09	7068.0091	299792458	-0.0624	-0.2965
2013-12-23	-8.624E-06	-2.0757E-09	7067.9221	299792458	-0.0610	-0.3111
2014-04-12	-7.780E-06	-2.0610E-09	7067.9767	299792458	-0.0550	-0.3089
...

The topic of outliers was already covered in [RD1] through the analysis of the SCR, and it was also mentioned that not all of the outliers can be linked to a drop in the SCR. Other causes may be orbit maneuvers or exceptional weather conditions not appropriately handled by the corrections. Usually such events are rare and we can assume that only a very small number of observations have to be eliminated as additional outliers. Therefore we suggest a simple statistical test using the mean of the range and azimuth differences, as well as the corresponding standard deviations. Results that are outside the limit defined by the mean value and two times the standard deviation are to be removed (2 sigma test), see example given in Figure 26. Note that individual sensors have to be treated independently. The figure only shows the procedure for TSX, but it was applied the same way to TDX. However, it is advised to perform the processing at least once without eliminating any potential outlier to inspect the entire data set and to analyze the raw SAR sensor performance.

The remaining ΔA and ΔR values are statistically summarized by the mean and the standard deviation, characterizing the sensors ALE capabilities. Provided that the SAR sensor behaves consistently across different imaging modes and beams, these four values give the full description of its geometric performance. The mean values correspond to the geometrical calibration constants in range and azimuth which may be annotated to the SAR product. If these calibration constants remain stable and hold at a global level, the standard deviations in range and azimuth can be interpreted as the system's accuracy (1 sigma level), that is, the ALE of a single range and azimuth observation of a point target with sufficient SCR.

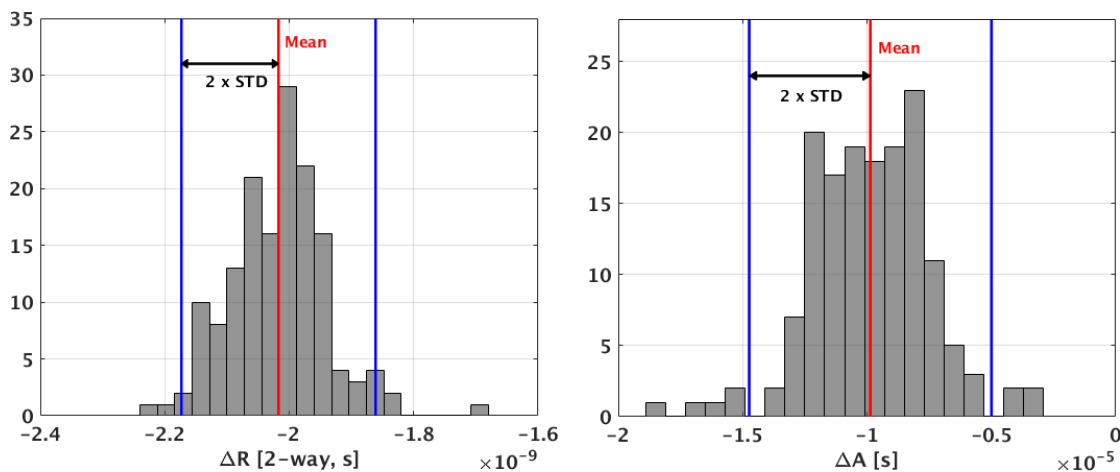


Figure 26: Outlier elimination by applying a 2 sigma test. The histograms show the data of the TerraSAR-X analysis of the corner reflector at Metsähovi observatory: Range (left), and azimuth (right).

A topic requiring some discussion is the units. For interpretation, one usually prefers metric results but the computations should be carried out in units of time. Due to the SAR principle, the range-time is the two-way round trip time and the conversion to units of length is given by the vacuum light ve-

locity. Therefore, one only has to make sure that all the terms of Eq. 35 are of the same unit and the same convention (1-way vs. two-way). The azimuth is the time of zero-Doppler in orbit and it is linked to the satellite's position and velocity. In units of time, e.g. seconds of day referring to the UTC, the azimuth result is unique but conversion to units of length is ambiguous. One can use either the satellite velocity which corresponds to the along-track distance the satellite is off from the predicted zero-Doppler position, or the ground track velocity (velocity of the zero-Doppler plane on ground) yielding the error made when localizing the target in the image. Because the SAR satellite's movement is bound to the Earth (curved geometry), these two velocities differ significantly. In the case of TSX, the average orbit velocity reads 7683 m/s while the ground track velocity varies with the location on the Earth surface and therefore across the swath (typical TSX values lie around 7050 m/s). In terms of metric ALE, the latter is the more appropriate value, but it needs to be computed separately for every target. On the other hand, the satellite orbit velocity applies to the azimuth calibration constant, i.e. the correction of the zero-Doppler time which needs to be applied by the SAR processor or to be annotated to the product to correct the timing grids. This is the reason why we advise to keep the computations in units of time, because in this case one directly obtains the calibration constants as required for subsequent use. Only the final results should be converted to metric units by using the appropriate velocities: vacuum light velocity for range and for azimuth the satellite's orbit velocity (calibration) or the zero-Doppler velocity (ALE analysis).

The TerraSAR-X example given in Table 9, Table 10 and Figure 27 illustrates the process. The ALE analysis along with the calibration is based on the 1.5 m CR installed at the Metsähovi geodetic observatory, Finland. The CR is oriented for the descending passes. Datatakes affected by snow and water are already removed; see the details given in [RD1] which leaves us with 185 usable acquisitions between November 2013 and December 2016. The data are high-resolution spotlight images of three different beams, i.e. beam 22, beam 45, and beam 68, which correspond to incidence angles at the CR of 27 degree, 37 degree and 45 degree, respectively. The tropospheric corrections are based on the IGS path delay product (see section 2.6.1.3) of Metsähovi's permanent GNSS station (IGS identification ID = METS), and the ionospheric corrections have been derived from the CODE GIM product (see section 2.6.2). For predicting the reference radar timings, all the geodynamic corrections given in section 2.7.1 have been applied to the CR reference coordinates.

The outcome of the comparison is given in Table 9. The reason for the remaining offsets is the omission of the calibration values annotated to the TSX products, which belong to a simplified atmospheric path delay correction that is in line with the TSX SAR processor and the operational product accuracy requirements of better than the 1 m [9]. The offsets found in the analysis may be interpreted as an improved geometrical calibration with more accurately determined constants, which correspond to the more elaborate calibration procedure described in this document. From the perspective of a SAR satellite data provider this is the dilemma of geometrical calibration: it is bound to the conventions and correction standards specified for the SAR product. See also discussion given in section 2.5.4. Using different models or adding additional corrections, e.g. some of the minor geodynamic

effects, might lead to unwanted offsets as illustrated in the example. For the advanced SAR user who aims at the best possible ALE capability of the SAR product, it is important that the processing of the SAR products remains both transparent and consistent. Modifications made in the internally applied processor constants have to be comprehensive because they affect the externally determined geometrical calibration. Only with this information ready at hand (like in the TerraSAR-X product annotation), an experienced user may perform an improved recalibration.

Table 10: Updated geometrical calibration constants for TerraSAR-X and TanDEM-X. The values have been derived from the ALE analysis of the 1.5 m corner reflector located at Metsähovi geodetic observatory. Conversion to meters is given by vacuum light velocity (range) and the TSX orbit velocity of 7683 m/s (azimuth).

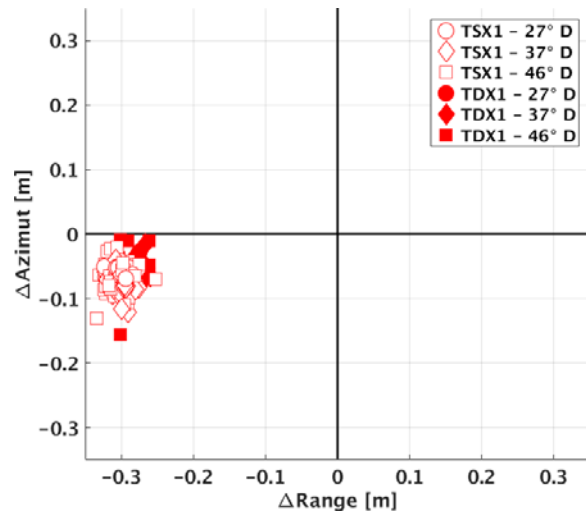
Sensor	Range [2-way, s]	Azimuth [s]	Range [1-way, m]	Azimuth [m]
TSX	-2.0203e-09	-9.83e-06	-0.3028	-0.0755
TDX	-1.8771e-09	-7.07e-06	-0.2814	-0.0543

Our full analysis of TSX and TDX is shown in Figure 27. After converting the differences in range and azimuth to metric units and arranging the values in two dimensions, the individual offsets of both sensors become clearly visible. To generate the figures, we used the zero-Doppler velocities of the beams as annotated in the TSX products [46] to convert the azimuth to the ALE in units of meters: 7068 m/s (beam 22), 7047 m/s (beam 45), and 7024 m/s (beam 68). Eliminating the small number of outliers (16 datatakes) by the 2-sigma test, as shown in Figure 26, yields two consistent clusters, one for TSX and one for TDX, see Figure 27c. The range and azimuth calibration constants, i.e. the remaining mean values, are summarized in Table 10. In units of meters, the range has to be corrected by approximately 30 cm, and the azimuth requires a shift of the satellite's zero-Doppler position by about 7 cm. Applying the new calibrations makes both satellites perfectly consistent (Figure 27d), and we may characterize the overall mission having a best possible ALE capability (1 sigma) of 1.1 cm in range and 1.5 cm in azimuth.

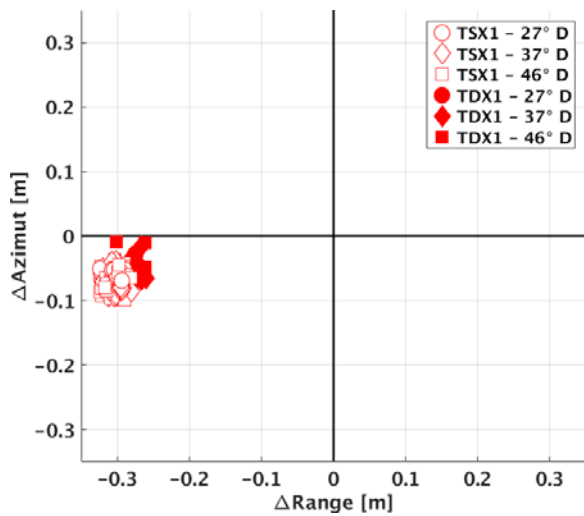
In addition to the 2-D scatter plots, time sequential visualization is another useful tool of graphical analysis for the ALE range and azimuth offsets. Only by the help of these representations one can discover slow seasonal variations, trends or discontinuities, but the interpretation is complicated by the fact that there are several potential causes which are hard to discriminate. Such signals might be due to limitations in the orbit determination, the site of the CR installation (e.g. hydrology), the SAR payload (oscillator aging), the processor generating the images, or the atmospheric models used to correct the path delay. This document shall help ruling out these effects one by one given the high accuracy potential of the proposed method.



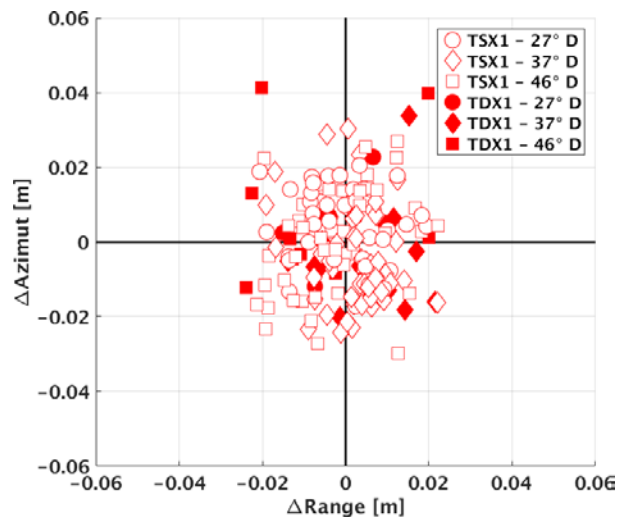
(a)



(b)



(c)



(d)

Figure 27: Absolute Location Error analysis and geometrical calibration of TerraSAR-X and TanDEM-X using the 1.5 m corner reflector of Metsähovi station (Finland). The corner reflector (a), raw result before outlier removal (b), result after outlier removal (c), and final result after applying the recalibration of Table 10(d).

The quality of the orbit may be cross-checked by SLR observations if available or by analyzing its internal consistency as discussed in [35]. The ground installations sites of CRs have to be selected with care and verification of the reference coordinates from time to time can confirm their stability. The SAR payload can be monitored by the help of dedicated calibration datatakes, and the processor should take into account the different effects connected to platform motion which are discussed in section 2.5.3. These two tasks the SAR payload and the processor are in the responsibility of the SAR satellite provider. The quality of the path delay modelling is to some extent linked to the installation site. Being close to a permanent GNSS receiver allowing for path delay corrections, or selecting a location having predictable atmospheric conditions give significant advantages in such detailed analyses. Thus we want to emphasize once more the importance of well-maintained test sites that rule out unwanted movement of the targets and allow for reliable path delay correction.

Figure 28 gives an example of an ALE range and azimuth time series, which was generated from the final TSX and TDX ALE result of Figure 27d. The two curves display mainly random patterns and do not indicate any prominent long term signal. Looking closer at the range (see blue shading in Figure 28 top), one can make out periods in the summer months where the range offsets become even more consistent, while around the spring times some slight peaks occur. These small remaining features are likely related to the TSX orbit, i.e. the handling of solar radiation pressure and the air drag, which was published in the analysis of the TSX science orbit product [35]. Refinements have been made and preliminary results using an updated orbit product tend to confirm that a renewed TSX orbit solution can improve the results of Figure 28. Hence even the sub-centimeter range ALE might become possible in near future if SAR missions are coupled with orbits of the best quality, and if the procedures outlined in this document are considered during the geometric calibration.

In this section we focused on the general steps to perform the comparison of predicted and observed SAR timings, as well as the basic methods to analyze the ALE. The (re)calibration was demonstrated and the TSX examples shown in this section give an idea what a user can expect from a well-behaving SAR sensor which has been optimized for smallest possible ALE. The following section provides further examples addressing aspects like the individual contribution of corrections or different SAR products, and it also includes Sentinel-1 to show results that may be obtained when certain elements like the SAR processor are not yet fully optimized for ALE at the far sub-pixel level.

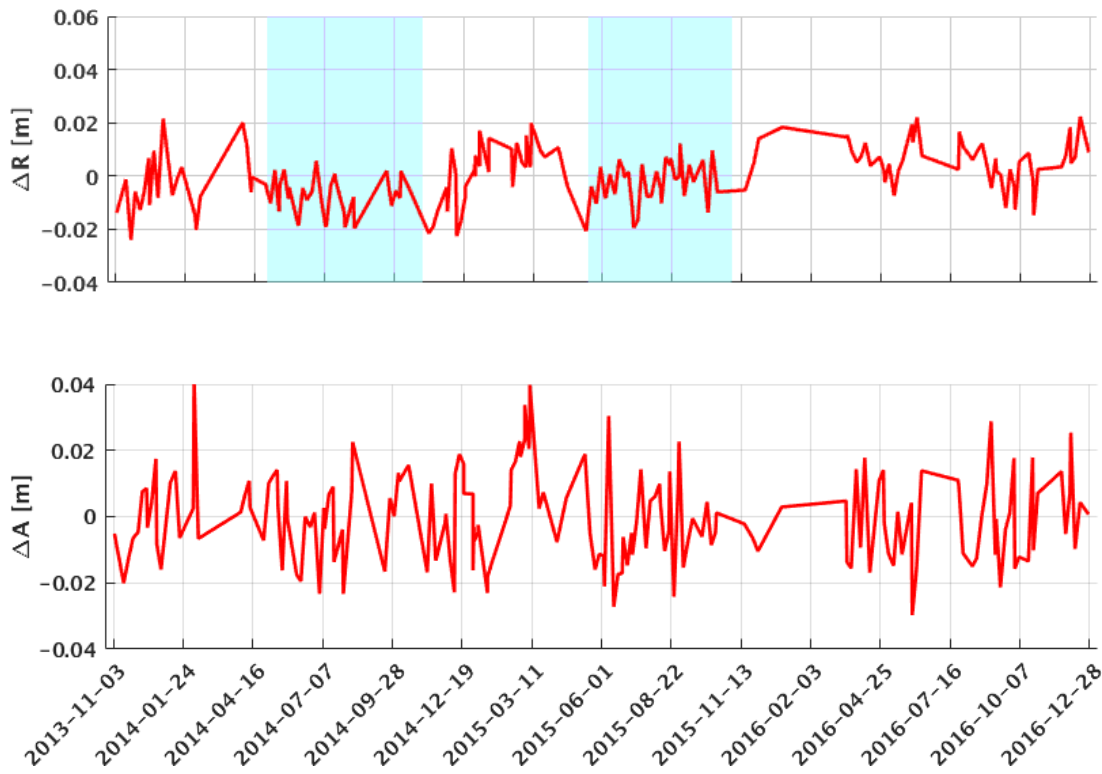


Figure 28: Time sequential view of the TerraSAR-X and TanDEM-X ALE analysis (final result as shown in Figure 27d) for the 1.5 m corner reflector of Metsähovi station, Finland. Range result (top) and azimuth result (bottom). The two periods in range with improved short term consistency are marked in blue.

4. Examples

In this chapter we present additional examples covering extended aspects of the ALE beyond the standard protocol which was discussed in chapter 3. The results are based on the datasets gathered for the various test sites operated by TUM/DLR and UZH, as well as the openly accessible CR array in eastern Australia maintained by Geoscience Australia (GA) [12]. The SAR satellites TSX & TDX and S1A & S1B regularly capture SAR images of these sites, which have been processed following the ALE protocol, starting from level-1b SSC products of different SAR imaging modes. Section 4.1 focuses on Sentinel-1 using the mission's default *interferometric wide swath* (IW) product. Section 4.2 deals with TerraSAR-X data in *high-resolution spotlight* mode and *Stripmap* mode.

4.1. Sentinel-1 Examples

The standard product of the Sentinel-1 mission is the interferometric wide swath mode (TOPS), see section 2.5.1, having resolution of about 3 m by 22 m (slant range by azimuth) [48]. It covers the ground in three parallel swaths (IW₁, IW₂ and IW₃) and a total swath width of approximately 250 km [47]. For central Europe, both satellites S1A and S1B offer a very high data rate of up to four active passes per 12 day repeat cycle). This high data rate amounts to 177 usable products for our 1.5 m CR (descending) at Wettzell, Germany Figure 33a), which form the basis for the following analysis.

Regarding the two Sentinel-1 satellites, 144 products of S1A and 33 products of S1B have become available as of July 2017. Both data sets comprise the two available passes at Wettzell (31° and 41° incidence angle), and the 41° products even allow for two independent SAR observations per pass due to the overlap in subsequent bursts; i.e. the CR is located in the overlap area of the constantly repeated IW burst pattern. Thus the ALE analysis can be based on CR observations in 31°-IW₁ and 41°-IW₂ (early azimuth & late azimuth).

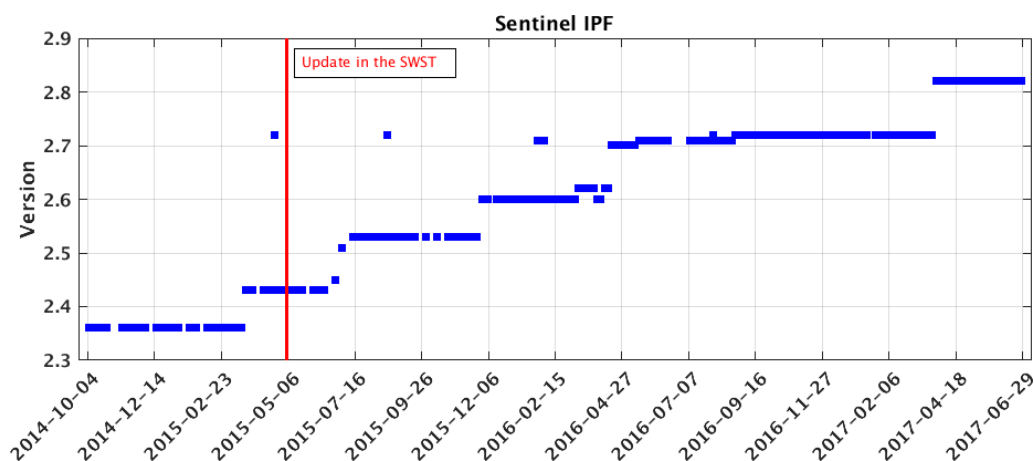


Figure 29: Overview on Sentinel-1 processor version (Instrument Process Facility, IPF) for the Wettzell dataset. The update in the Sampling Window Start Time (SWST) on March 5th has to be considered in products generated by the IPF before this date [51].

The processing was carried out using the full protocol: troposphere (IGS GNSS ZPD products), ionosphere (CODE GIMs) and all the described geodynamic displacements. Moreover, the residual bistatic correction [49] to redeem the incomplete compensation of the *satellite motion during echo reception* in the S1-IPF (see section 2.5.3.2.1, Eq. 6) was applied to the observed azimuth after performing the PTA. Another property of S1 products is the changing IPF SAR processor version, as it can be seen in Figure 29 for the Wettzell data set. In the standard scenario, SAR products are processed only once, and because there is no reprocessing involved, changes in the underlying auxiliary products or timing corrections may lead to discontinuities in the ALE analysis. A well-known example is the sampling window start time (SWST) parameter, which was updated in the IPF in May 2015 [51], see Figure 29. We have modified our data accordingly, so in the results shown here, this jump is not present anymore in the S1A analysis. Similar effects were observed in TerraSAR-X data sets due to updates of the geometrical calibration in the TMSP [6][55]. To avoid such behavior and to ensure consistent results, it is advised to base the ALE analysis on a homogeneously processed data set. For S1A/B, the SWST parameters and the delay constants are given in the instrument auxiliary data²⁵, which can be related to the annotation of a dedicated S1A/B product. In terms of the orbit product, all the annotated S1A/B state vectors have been exchanged for the final precise orbit product also available at the Sentinel-1 quality control website²⁶.

The temporal view of the S1A/B ALE displayed in Figure 30 reveals several features which can be linked to the elements of the TOPS data. Most prominent are the individual ALE offsets for the different subswaths (31° -IW1 vs. 41° -IW2) for both range and azimuth. Apart from a small deviation in the mean value, S1A and S1B behave identically. The magnitude of the offsets is not critical when regarding the official 7 m ALE requirement (3σ) for the IW data [48], but the beam dependence makes the geometrical calibration much more cumbersome. The results are in line with the data analysis published in [50], which found evidence for beam dependence across all the S1 products (SM, IW and EW). Therefore every beam/product combination would require an individual geometric calibration, which is hardly feasible, and the ESA IPF team is now investigating for possible improvements, addressing known limitations of IPF in compensating for the platform motion (see section 2.5.3.2).

Another more subtle effect is the different results of the burst overlap area (41° -IW2). While azimuth displays a more or less random behavior (Figure 30, diamond markers), the range offsets are clearly separated into two distinctive lines. If we remember that the 31° -IW1 measurements take place around center azimuth of burst, a pattern becomes visible: from early azimuth to mid azimuth to late azimuth, the average range error shifts from about 0.5m to -0.25m. The most probable explanation is the *satellite motion during pulse duration* (see section 2.5.3.2.3), which is known to cause a range bias.

²⁵ https://qc.sentinel1.eo.esa.int/aux_ins/

²⁶ https://qc.sentinel1.eo.esa.int/aux_poeorb/

In [52] theoretical considerations are presented for S1 TOPS and the effect is estimated with about 0.25 resolution cells, or about 0.75 m when applying the nominal IW slant range resolution of roughly 3 meters. This is an almost perfect match for value we found in the practical ALE.

When visualized in the usual 2D ALE scatter plot, the discussed effects lead to three distinctive clusters, see Figure 31. In terms of ALE quality, the range is vastly superior which was expected because the 1.5 m CR provides approximately 29 dB SCR in IW C-band, which translates into a theoretical ALE of about ± 0.04 m (range) and ± 0.30 m (azimuth), see details in [RD1]. The ALE values achieved in the experiment (cf. Table 11) are very close when considering the results on a cluster by cluster basis. There seems to be slight advantage of S1B over S1A, but the numbers should not be stressed too much, as the temporal coverage of both sensors is quite different.

In conclusion of the overall values listed in Table 11, the 1σ ALE capability of Sentinel-1 IW amounts to about ± 0.35 m in range and ± 1 m in azimuth, provided that the overall mean values found for S1A and S1B would be re-introduced as their updated geometrical calibration. This might appear sufficient when compared to the average resolution of the IW product, but the true potential of the data is illustrated by the cluster results. Therefore, investigation of the S1 IPF for compensating the satellite motion effects is currently in progress. This could allow for a much more consistent S1A ALE and ease the geometrical calibration.

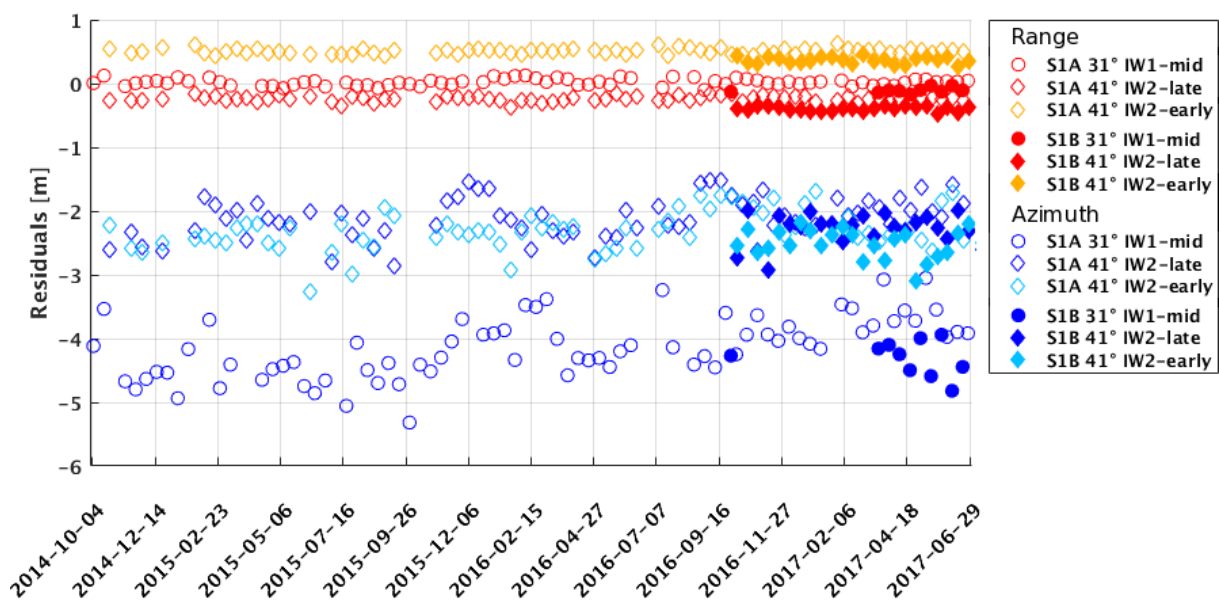


Figure 30: Time sequential view of the Sentinel1A/B ALE result for the IW data of the Wettzell 1.5m descending CR. Δ Azimuth [m] in blue, Δ Range [1-way, m] in red.

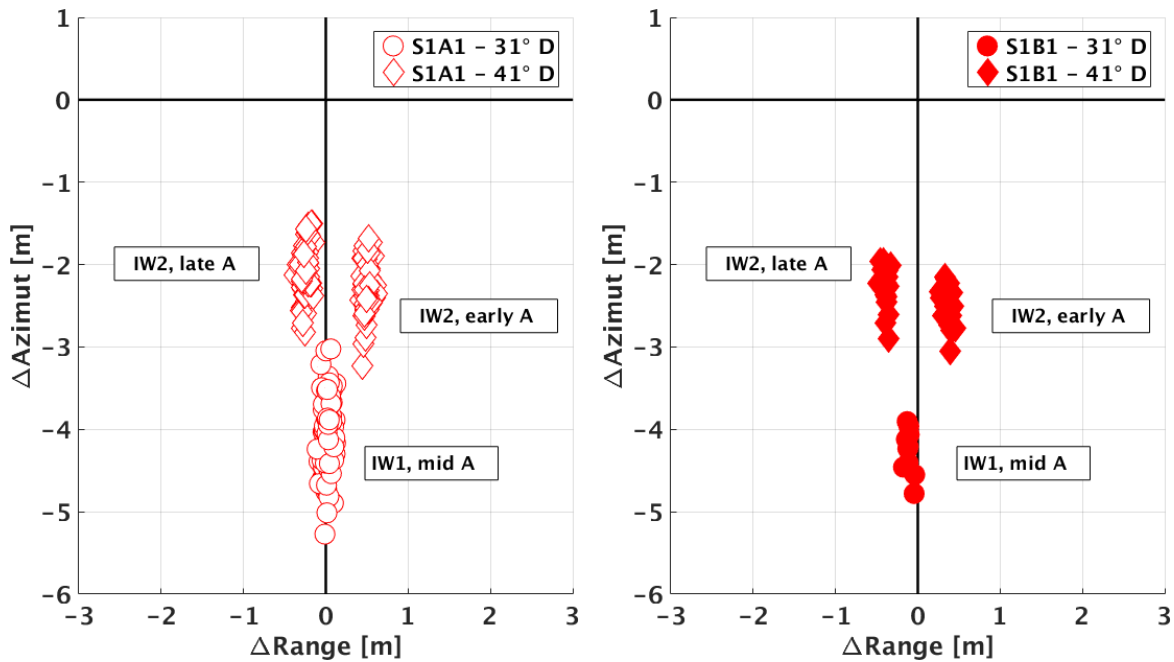


Figure 31: ALE result of Sentinel-1A (left) and Sentinel-1B (right) for the IW TOPS data of the 1.5 m CR located at Wetzell, Germany.

Table 11: ALE results for the Sentinel-1A/B IW data of the 1.5 m CR located at Wetzell, Germany. The beams refer to the clusters shown in Figure 31. N is the number of observations.

Beam	Sentinel-1A			Sentinel-1B		
	N	ΔR [1-way,m]	ΔA [m]	N	ΔR [1-way,m]	ΔA [m]
IW1 _{mid A}	70	0.017 ± 0.052	-4.091 ± 0.468	23	-0.109 ± 0.041	-4.252 ± 0.276
IW2 _{early A}	70	0.503 ± 0.042	-2.284 ± 0.305	23	0.361 ± 0.052	-2.490 ± 0.229
IW2 _{late A}	74	-0.245 ± 0.044	-2.084 ± 0.314	10	-0.398 ± 0.037	-2.252 ± 0.242
All data	214	0.090 ± 0.311	-2.843 ± 0.985	56	-0.035 ± 0.351	-2.707 ± 0.773

Recent results for Sentinel-1 over the Australian Corner Reflector Array Test Site

In Queensland in Eastern Australia there is a large CR array consisting of 40 reflectors distributed over a roughly circular area ~120 km wide, installed in 2014 by Geoscience Australia (GA) [12]. Although the array's primary purpose is to provide support for interferometric processing of the Surat region in Queensland, the very high quality of the installations and the careful DGPS survey of the CR coordinates make this field an attractive test site for SAR ALE activities. Errors in a few of the target coordi-

nates initially provided were discovered after first analyses of the targets using Sentinel-1 [50], but these were later resolved by reprocessing the DPGS survey data; please refer to the details given in the supplemental material to [12] added in response. With ITRF 2008 coordinates publicly available for this site, all the information required for a high-quality ALE analysis exists. The CR mount models providing the offset between the survey point and the CR phase center (corner apex) may be requested from GA²⁷, and the ITRF displacement of the test site may be inferred from IGS stations in Eastern Australia (see section 2.7.1.2.6).

Of the 40 available CRs, most of them (34) are 1.5 m in size, with three each at 2.0 m and 2.5 m large. All CRs are oriented for ascending pass geometries. The average uncertainty of the survey (2σ) is given as 2.2 cm horizontal and 4.4 cm vertical, but the mount models required for computing the phase centers may introduce some additional uncertainty.

Figure 32 shows scatterplots of the S-1A and S-1B ALE after processing at UZH for frame shift, atmospheric corrections, SET, and bistatic residual corrections (Eq. 6, see section 2.5.3.2.2), as well as intra-burst corrections (see section 2.5.3.2.3). A recent improvement to the way the bistatic correction of Eq. 6 is made is responsible for the reduced swath-to-swath overlap in azimuth compared with the IW_{1/2} azimuth separation visible in Figure 31. The updated correction is being currently implemented by DLR as well. Also, the inter-pulse satellite motion discussed earlier in connection with Figure 31 has also been corrected in Figure 32 (see section 2.5.3.2.3), responsible for a reduced range spread overall. These first S-1 results with refined corrections for the satellite motion effects suggest that the ALE for IW TOPS can be further improved, and the findings will be made available once the testing has been completed.

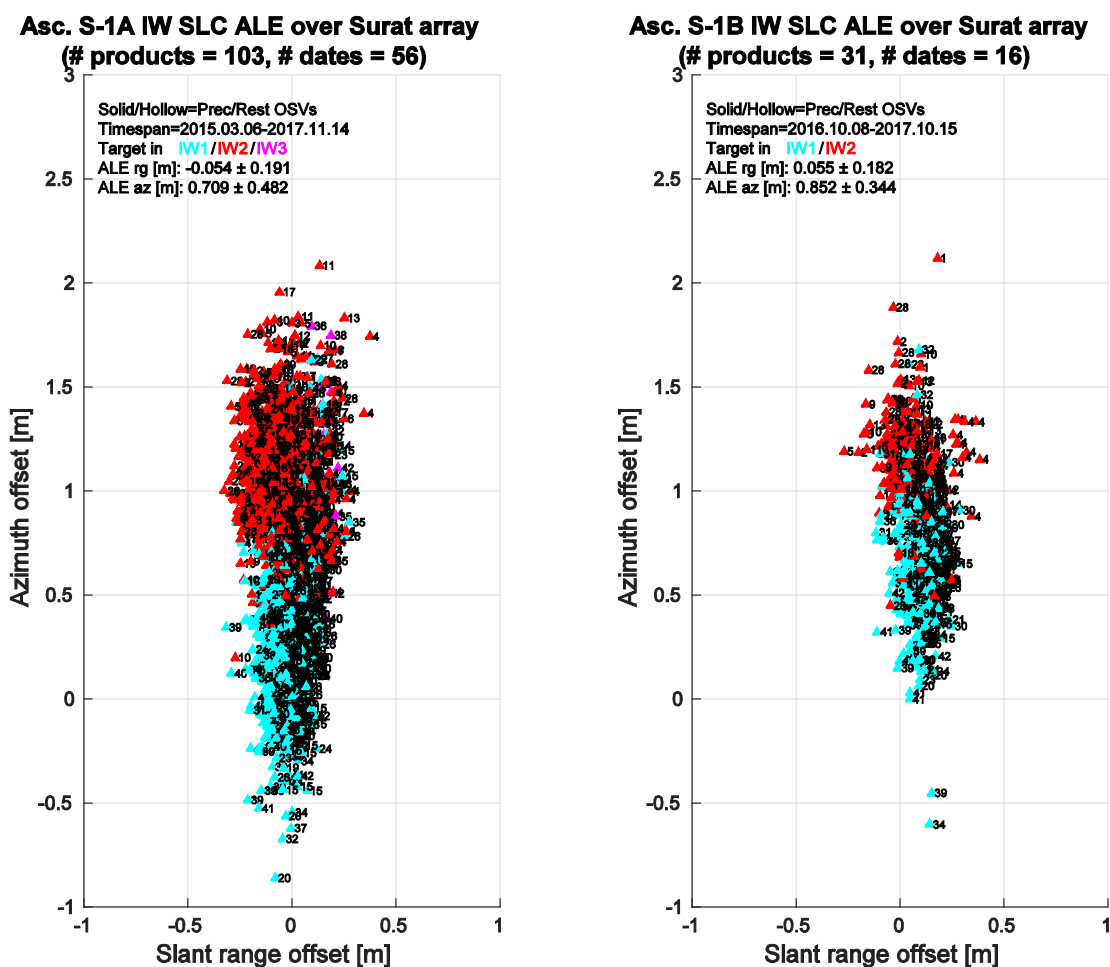
The difference in the sign convention used by UZH and DLR/TUM for the equations Eq. 34 and Eq. 35 is responsible for a reflection of the ALE points about the range and azimuth axes when moving from one to the other. While DLR/TUM scatter ALE is calculated as “imaged positions – predicted positions”, UZH employs the opposite convention (predicted – imaged). In the former case, the image is considered to be the measurement to be compared with the GNSS-based reference. UZH takes another approach, preferring instead to consider the image raster the reference while testing the accuracy of the predicted positions, which are based on the product annotations in combination with timing corrections applied during post-processing. Nonetheless, comparison of the mean bias magnitudes, the range and azimuth spreads and the relative offsets between subswaths is not hindered by this difference in convention. In any case, this difference is not immediately obvious when comparing Figure 31 and Figure 32, however, mainly because of the reduction in the azimuth ALE and inter-

²⁷ Geoscience Australia: geodesy@ga.gov.au

For further details see the supplemental material of [13]: <https://doi.org/10.1080/08120099.2015.1040073>

swath disparity in the latter case made possible by the additional inter-pulse and updated bistatic corrections.

As in the DLR/TUM processing, there was a small difference in the *mean* range bias between the two sensors. A mean spread of 19 cm in range and about 41 cm in azimuth was observed. Note that both values were calculated for a combination of subswaths (IW₁ and IW₂). Slightly smaller scatter was observed within each subswath alone. Small relative azimuth shifts are visible between the IW₁/2/3 subswaths (~58 cm between IW₁/2; ~12 cm between IW₂/3), which may be the result of even more subtle biases which are currently still under investigation. The best methods for the implementation of the known timing corrections are currently still being investigated by UZH, DLR and others.



(a) S-1A ALE from IW-SLC products covering the CR array

(b) S-1B ALE from IW-SLC products covering the CR array

Figure 32: S-1 ALE for IW-SLC products covering the CR array in Queensland, Australia

4.2. TerraSAR-X Examples

Examples for TerraSAR-X have already been demonstrated in chapter 3. In this chapter we want to exploit the possibilities offered by the high resolution of TerraSAR-X and show some details of the protocol, demonstrate the importance of the different correction steps, and show the accuracy differences of different correction methods.

Impact of corrections

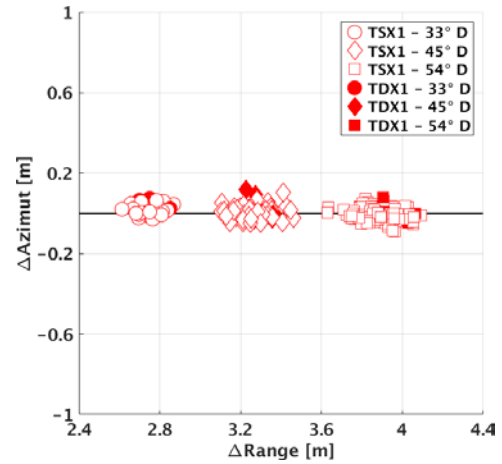
To discuss the impact of the atmospheric path delay and the geodynamic displacement of the CR reference, we processed the TSX data of the Wettzell test site (Germany) several times while introducing the corrections one by one. The geodetic station at Wettzell hosts two CRs with 1.5 m edge length, oriented for ascending and descending passes, respectively, of which we show the TSX result of the descending CR. The underlying data are 199 SAR images acquired between 12/2013 and 01/2017 with TSX and TDX in high-resolution spotlight mode. They have a nominal resolution of 0.6 m by 1.1 m (range by azimuth). The images are distributed across three beams (spot 35, spot 66, spot 97) resulting in incidence angles at the CR of approximately 33°, 45°, and 54°.

The step by step ALE results in range and azimuth are listed in Table 12, and are also visualized in Figure 33b-f. Starting from the raw SAR data and using only the renewed TSX and TDX geometrical calibration (see previous chapter 3), the outcome is dominated by the range error due to the troposphere. The error is composed of three groups according the beams, see Figure 33b. On average, the range offset reads about 3.5 m, and not correcting any path delay would mean a range ALE of ± 0.5 m. On the other hand, the azimuth is already very accurate because its error is mainly driven by the timing accuracy of the SAR processor, as well as the along track orbit quality. If orbit and processor are of sufficient quality, the azimuth may easily be centered to zero-Doppler using a single azimuth calibration constant.

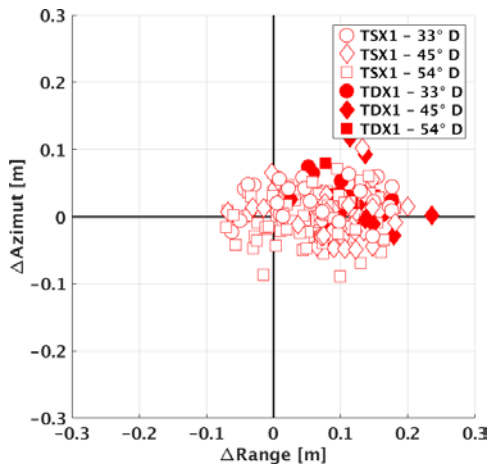
Introducing the tropospheric correction generates a huge improvement in range, both the offset and the spread in range are reduced to sub-decimeter level. The impact of the ionosphere is less pronounced in X-band, but its importance becomes immediately clear when additionally taking into account the solid earth tides and the epoch of the SAR acquisition, that is, the linear displacement of the CR expressed by the \dot{X}_{ITRF} . Only when considering the triplet of troposphere, ionosphere and solid earth tides, one is able to approach the 1-2 cm level in range, given that the test site experiences no substantial deformations by ocean loading. Note that the azimuth slightly gains through the removal of the horizontal signals coming from the geodynamics.



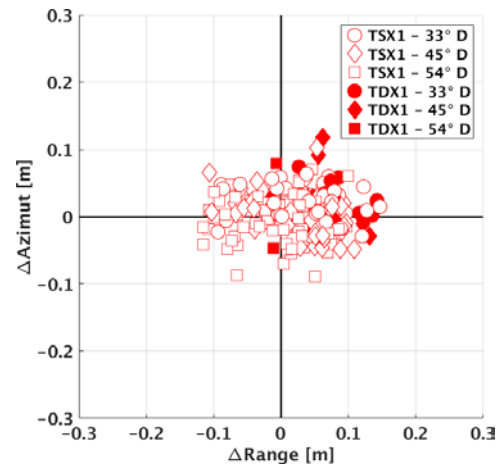
(a) Wettzell 1.5 m CR



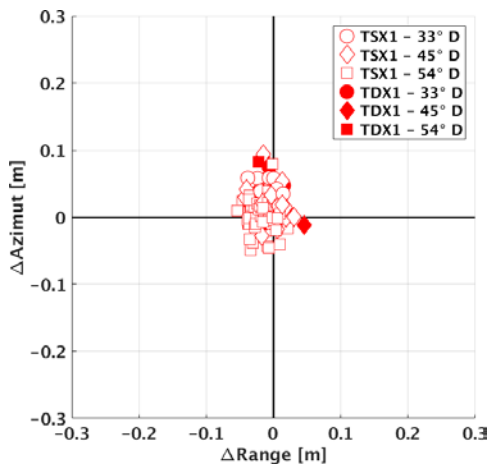
(b) Raw result



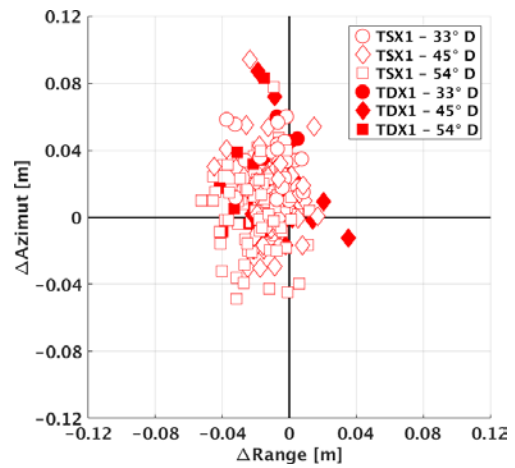
(c) Troposphere removed



(d) Ionosphere removed



(e) Solid Earth tides and tectonics removed



(f) Other geodynamic effects removed

Figure 33: TerraSAR-X and TanDEM-X result of Wettzell 1.5 m CR. Corrections have been added step by step.

Table 12: Impact of the individual corrections when using a geometrically calibrated SAR sensor. Example of TerraSAR-X using high resolution spotlight data of the Wettzell 1.5 m CR. Starting from the calibrated raw data, the path delays and the different geodynamic effects are included step by step. In the last step, outliers are removed by the 2 sigma test.

Correction	Δ Range [1-way, m]	Δ Azimuth [m]
Raw - calibration parameters	3.451 ± 0.460	0.006 ± 0.034
+ Troposphere	0.075 ± 0.064	0.006 ± 0.034
+ Ionosphere	0.022 ± 0.060	0.006 ± 0.034
+ Solid Earth Tides, \dot{X}_{ITRF}	-0.013 ± 0.016	0.013 ± 0.025
+ Other geodynamic effects	-0.014 ± 0.014	0.013 ± 0.024
Outliers removed (2 sigma test)	-0.013 ± 0.013	0.013 ± 0.020

The other geodynamic effects, which have been described in section 2.7.1.2, further improve the ALE by 1-2 millimeters, but users should be aware that the ocean loading can have a much larger impact for certain coastal locations. After performing the 2 sigma test, the final ALE result (last line of Table 12) is quite close to what was achieved at our primary calibration site in Metsähovi, Finland (see chapter 3). The remaining offsets confirm the applicability of the new calibration constants.

Concluding from this example, the troposphere, the ionosphere and the solid earth tides **must be corrected for every ALE analysis**. Along with the proper consideration of the ITRF epoch/linear displacement, this allows for an absolute localization of better than 3 cm, provided that the SAR processor and the orbit are of similar quality, and that the target is bright enough (no radiometric ALE limitation).

Troposphere Impact

In section 2.6.1, we have proposed three different strategies to compute and remove the tropospheric path delay in a SAR ALE analysis. To provide a guideline for their impact on the SAR ALE, the five CRs available to DLR/TUM have been processed with the different tropospheric corrections. The CRs are located at three geodetic stations: Wettzell (Germany), GARS O'Higgins (Antarctica) and Metsähovi (Finland). Their sizes range from 0.7 m (GARS O'Higgins) to 1.5 m (Wettzell, Metsähovi). They are covered by a large amount of TSX-1 and TDX-1 HR spotlight data, see Table 13, involving several different high-resolution spot light beams between 27° and 54° incidence angle, as well as ascending and descending passes. The temporal timelines read as follows: 07/11-12/16 (Wettzell), 03/13-01/16 (GARS O'Higgins), and 11/13-12/16 (Metsähovi).

The results based on the GNSS tropospheric delays (IGS product) define the benchmark of the comparison (see last line of Table 13). Calibrated by the Metsähovi CR, the average range offsets usually

remain below 1.5 cm; only the Wettzell ascending CR shows a slightly larger value. Also the standard deviations are perfectly comparable across all CRs. In accordance with their sizes, the smaller 0.7 m CRs at GARS O'Higgins lack some 1-2 mm in the standard deviation when compared to the larger CRs.

If we exchange the troposphere for the VMF₁ or the ECMW Slant range integration, the results degrade across all test sites, but the effect is not very large, i.e. roughly 6 mm for the worst case. Of interest are the mean values in case of GARS O'Higgins. Apparently there is an offset between the ECMWF model and what is observed by GNSS. Both the VMF₁ zenith delays and the slant range integration make use of the ECMWF model, and in both cases we observe similar offsets of about 4.5 cm. The reason for this behavior is unclear but when the goal is 1-2 cm consistency across several test sites, the IGS path delays should be favored. Nevertheless, the other methods are useful alternatives; especially their global applicability offers considerable advantage when moving from dedicated ALE cal/val activities to monitoring applications.

Table 13: Comparison of different methods to correct the tropospheric path delay at the different test sites used by TUM/DLR for TSX and TDX ALE analysis. ΔRange mean and standard deviation [1-way, in cm].

	WTZ _A (86 DTs)	WTZ _D (199 DTs)	OHI _A (200 DTs)	OHI _D (94 DTs)	MET _D (185 DTs)
EMWF	-3.0 ± 1.8	-1.5 ± 1.7	5.7 ± 1.7	2.9 ± 1.7	-0.3 ± 1.5
VMF ₁	-1.1 ± 2.2	1.1 ± 1.9	4.4 ± 1.6	4.3 ± 1.8	-0.4 ± 1.5
IGS ZPD	-2.3 ± 1.3	-1.4 ± 1.4	0.2 ± 1.7	0.3 ± 1.5	0.0 ± 1.3

Australian CR Array with TSX Stripmap

The corner reflector array in Queensland, Australia, was described in the latter part of section 4.1. A first test of the coordinates including the mount model is presented here by using several TerraSAR-X Stripmap scenes, with the scatter plot shown in Figure 34. The data have been captured for two subsets of the array and comprise the CRs 5,6,8,9,13,14 (first subset, 13 scenes, 12/14-09/15) and 30,36,37,38,40 (second subset, 4 scenes, 12/14-02/15). The geometries are different, i.e. the first subset was measured with beam 4 (~24° incidence angle) and second subset with beam 11 (~42° incidence angle). The ALE analysis follows the entire protocol: troposphere (VMF₁ ZPD products), ionosphere (CODE GIMs), the total of the geodynamic displacements, and the updated TSX-1/TDX-1 calibration constants (see chapter 3).

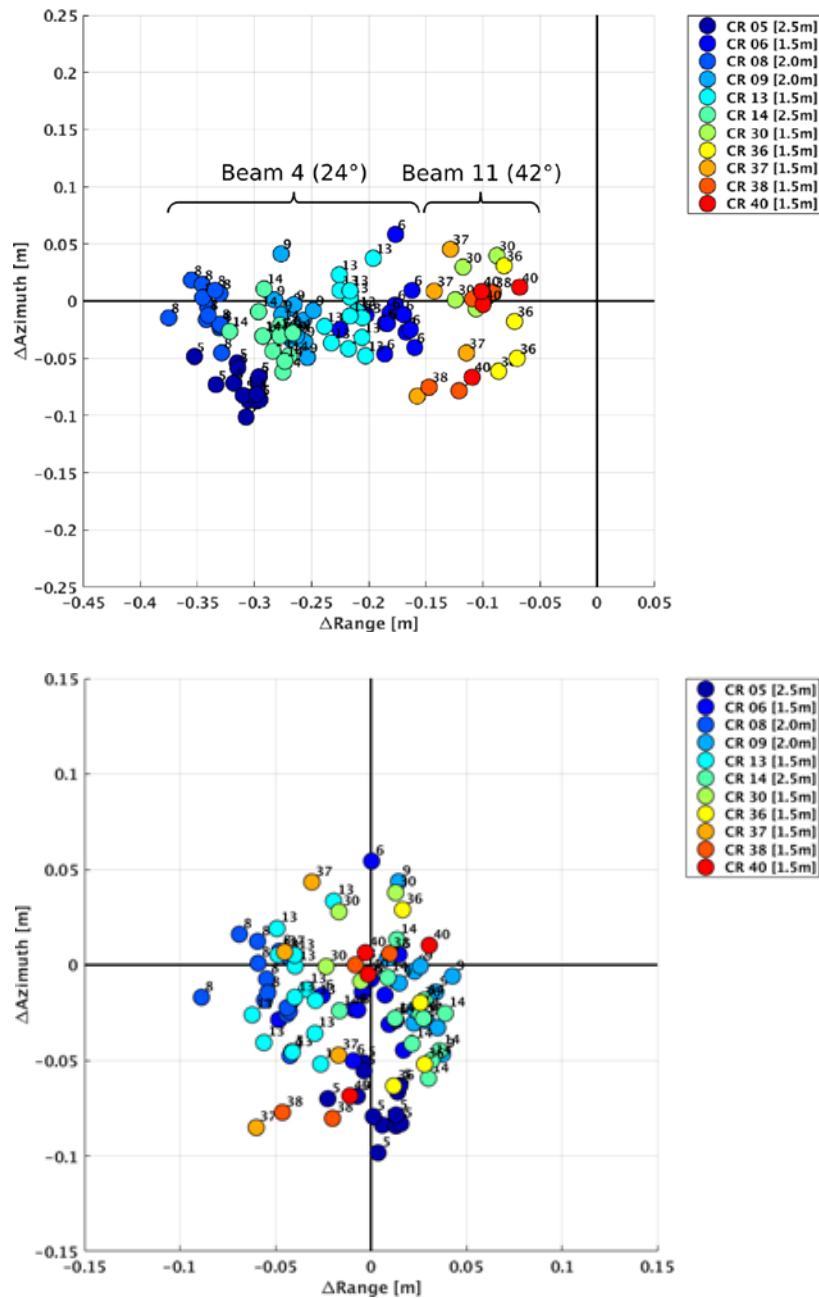


Figure 34: TSX ALE for two subsets of the CR array in Australia captured with Stripmap data. Result without the mount model for the CR phase center (top) and result after applying the model (bottom). Note the change in the scope of the axes.

With the mount model included, the CRs show very good ALEs of 1-2 cm standard deviation in range and 2-5 cm standard deviation in azimuth for the TerraSAR-X Stripmap, see values in Table 14. The larger CRs should provide a smaller ALE and this is indeed the case when examining the azimuth results. The small amount of only 4 datatakes for the second subset makes these results less reliable,

but nonetheless they remain fairly consistent. Regarding the remaining offsets, almost all of them are explained by the uncertainty of the reference coordinates. The only CR which raises some questions is CR 5, because the -7.2 cm offset in azimuth is somewhat larger than expected. Possible reasons are the mount model (not perfectly aligned with the orientation) or the survey.

In summary, we can conclude from our results that the Australian CR array allows for high quality ALE processing at the 5 cm level and SAR satellite providers are well advised to use it for the analysis of their different products and to (re)calibrate their sensors. Further investigation of the array is now due to be carried out under this ESA contract as a cooperation of DLR, GA, TUM and UZH. We intend to qualify all of its CRs as best as possible with TerraSAR-X and Sentinel-1, and plan to publish our findings later next year.

Table 14: ALE results for the TerraSAR-X Stripmap data for the 11 CRs of the GA reflector array (Queensland, Australia) which are covered by the Stripmap data set. The CR id (first column) corresponds to the list published by GA [12].

CR [#]	Size [m]	Datatakes	Range [1-way, cm]	Azimuth [cm]
5	2.5	13	-0.1 ± 1.7	-7.2 ± 1.5
6	1.5	13	-0.4 ± 1.8	-1.8 ± 2.6
8	2.0	13	-5.5 ± 1.3	-1.1 ± 1.8
9	2.0	13	2.5 ± 1.0	-1.4 ± 2.3
13	1.5	13	-4.0 ± 1.2	-1.5 ± 2.6
14	2.5	13	2.0 ± 1.5	-2.8 ± 1.9
30	1.5	4	-1.0 ± 1.6	1.3 ± 2.2
36	1.5	4	1.9 ± 0.8	-2.8 ± 4.2
37	1.5	4	-4.0 ± 1.9	-2.1 ± 5.7
38	1.5	4	-1.7 ± 2.3	-3.9 ± 4.7
40	1.5	4	0.2 ± 1.9	-1.5 ± 3.6

Appendix 1: Fundamental Geometric Relationships

The following section describes fundamental geometric relationships that are needed throughout the processing presented in this document. By definition, we select the global International Reference Frame (ITRF) as the reference for the ALE processing; see the details in section 2.4. The conversion of an ITRF coordinate X to latitude φ and longitude λ is based on the WGS-84 ellipsoid (Table 15), which is also required to compute azimuth A and elevation E of a satellite in the local horizontal frame of a CR position X , cf. Figure 35.

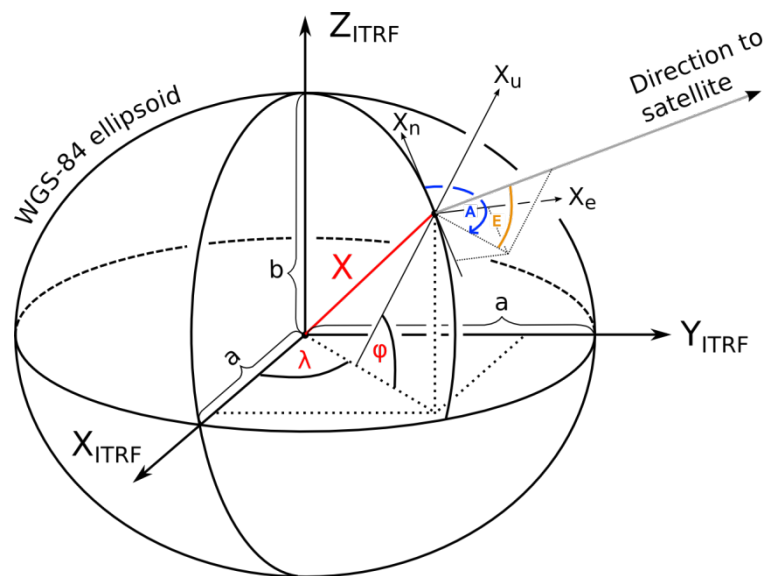


Figure 35: Definition of a local Cartesian reference frame for the ITRF position X using the WGS-84 ellipsoid (a , b) as a proxy for the Earth's surface geometry. The direction to a satellite in the local frame is given by azimuth and elevation (A , E).

Table 15: Dimension parameters of the WGS-84 ellipsoid [32]

WGS-84 parameters	
semi major axis	$a = 6\,378\,137.0\text{ m}$
semi minor axis	$b = 6\,356\,752.3142\text{ m}$

Conversion between global x , y , z and latitude, longitude, height using the WGS-84 ellipsoid

To convert global ITRF coordinates $\mathbf{X} = [x \ y \ z]^T$ to latitude, longitude and height, one can use the following set of equations [13] and the ellipsoid parameters listed in Table 15:

$$\varphi = \arctan \frac{z + e'^2 b \sin^3 \theta}{p - e^2 a \cos^3 \theta} \quad \text{Eq. 36}$$

$$\lambda = \arctan \frac{x}{y}$$

$$h = \frac{p}{\cos \varphi} - N$$

with the auxiliary quantities

$$e^2 = \frac{a^2 - b^2}{a^2}$$

$$e'^2 = \frac{a^2 - b^2}{b^2}$$

$$\theta = \arctan \frac{z a}{p b}$$

$$p = \sqrt{x^2 + y^2}$$

$$N = \frac{a^2}{\sqrt{a^2 \cos^2 \varphi + b^2 \sin^2 \varphi}}$$

Note that in their implementation the arctan2 function should be used to avoid ambiguities when computing the angles.

Conversion between global x, y, z and local North, East, up

The local system of an observer on the Earth's surface requires the definition of local axes in North East and up direction. Using the WGS-84 ellipsoid as proxy for the Earth's surface, the local horizon can be defined by the tangential surface spanned by the local North and East direction vectors, and the up direction is simply the direction of the ellipsoidal height, see Figure 35. Consequently the rotation matrix \mathbf{R} for mapping the global axes to the local axes at the location the point \mathbf{X}_P is computed from its latitude φ_P and longitude λ_P [13]:

$$\mathbf{R} = \begin{bmatrix} -\sin \varphi_P \cos \lambda_P & -\sin \varphi_P \sin \lambda_P & \cos \varphi_P \\ -\sin \lambda_P & \cos \lambda_P & 0 \\ \cos \varphi_P \cos \lambda_P & \cos \varphi_P \sin \lambda_P & \sin \varphi_P \end{bmatrix} \quad \text{Eq. 37}$$

The latitude and longitude are computed by Eq. 36. The transformation of an arbitrary global coordinate \mathbf{X}_{global} to this local system situated at \mathbf{X}_P reads

$$[x_n \ y_e \ z_u]^T = \mathbf{R} \cdot (\mathbf{X}_{global} - \mathbf{X}_P) \quad \text{Eq. 38}$$

The Eq. 38 is fundamental for the computation of a SAR satellite's azimuth and elevation at zero Doppler, as well as the conversion of the corrections of the dynamic Earth. The latter requires the inverse transformation because most of the underlying geodynamic models yield the displacements in the local geometry $[x_n \ y_e \ z_u]^T$, see section 2.7.1. To reverse the Eq. 38, one simply transposes the \mathbf{R} (i.e. the inverse of a rotation matrix is equivalent to the transposed matrix):

$$\mathbf{X}_{global} = \mathbf{R}^T \cdot [x_n \ y_e \ z_u]^T + \mathbf{X}_P \quad \text{Eq. 39}$$

Keep in mind that geodynamic displacements $[\Delta x_n \ \Delta y_e \ \Delta z_u]^T$ are only relative changes with respect to the location \mathbf{X}_P and therefore the transformation from the local frame to the global frame becomes a simple rotation.

$$\Delta \mathbf{X}_{global} = \mathbf{R}^T \cdot [\Delta x_n \ \Delta y_e \ \Delta z_u]^T \quad \text{Eq. 40}$$

Computation of azimuth and elevation of a satellite

The computation of a SAR satellite's azimuth and elevation at zero-Doppler requires the solution of the range-Doppler equations, see section 2.7.4. Once the range-Doppler equations have been solved, the position vector of the SAR satellite at zero-Doppler time is transformed to the locale frame of the CR by using Eq. 38. From the transformed vector, the azimuth A and the elevation E are easily derived. The elevation may be converted to the zenith angle z required by several of the correction formulas.

$$A = \text{atan} \left(\frac{y_e}{x_n} \right) \quad \text{Eq. 44}$$

$$E = \text{atan} \left(\frac{z_u}{\sqrt{x_n^2 + y_e^2}} \right)$$

$$z = 90 - E$$

Appendix 2: Sentinel-1 Sample Calculation

This sample calculation demonstrates the application of the protocol procedure for Sentinel-1A based on the corner reflector CR11 at the reflector array in Queensland, Australia; see also the examples in section 4.1. It was imaged on May 5th, 2016 and is included in the data product

S1A_IW_SLC__1SSH_20160511T083250_20160511T083320_011208_010FoA_EEBE.SAFE

which can be obtained from the Sentinel open access hub²⁸.

Based on this example, we show all calculation steps required to:

- determine the expected position of a target
- correct the measured radar time coordinates of this target for Stop-Go-Approximation and signal propagation effects
- compute the ALE

Table 16 and Table 17 give an overview on the calculations and may serve as a template that a user can adopt for his own computations.

The first step is to determine the instantaneous coordinates of the target, see Table 16. The ITRF2008 coordinates of CR11 are known from the geodetic survey carried out by Geoscience Australia (GA) who installed and maintains the CR test site [12]. The coordinates have to be transformed to the epoch of datatake acquisition (2016.361, when expressing the date November 5th, 2016 in units of years) – see section 2.7.1.2.6. Moreover, one has to add the contributions of the different geodynamic effects (see section 2.7.1) evaluated for the instant of the datatake acquisition, i.e. 2016-05-11 08:33:52 UTC. The computed azimuth is equivalent to the instant of closest approach between sensor and target (Table 17, row 1). The underlying position and velocity of the sensor at this instant (Table 16, rows 8 and 9) result from the Zero Doppler equations using orbit interpolation (see sections 2.7.3 and 2.7.4). To obtain accurate results, one should use the Sentinel-1 precise orbit ephemerides product²⁹

S1A_OPER_AUX_POEORB_OPOD_20160531T121522_V20160510T225943_20160512T005943.EOF

²⁸ <https://sentinel.esa.int/web/sentinel/sentinel-data-access>

²⁹ https://qc.sentinel1.eo.esa.int/aux_poeorb/

Subsequently the computed reference range is derived from the geometric distance between target and sensor.

The measured range and azimuth are extracted with the point target analysis (see section 2.5.5). For the selected product of Sentinel-1A, the CR₁₁ is located in burst 1 of the subswath IW₂. The accurately determined sub-pixel coordinates for the peak of the CR point response within this burst read:

$$\begin{aligned} az &= 249.8798 \\ rg &= 6430.3507. \end{aligned}$$

The corresponding radar time coordinates

$$\begin{aligned} t_{CR,m} &= t_o + az/PRI = 2016-05-11T08:32:52.260504997 \text{ UTC} \\ T_{CR,m} &= T_o + rg/RSF = 0.005770939113 \text{ s} \end{aligned}$$

are computed from the time annotation (i.e. azimuth and range start times and sampling rates) of the burst:

$$\begin{aligned} t_o &= 2016-05-11T08:32:51.746863 \text{ UTC} \\ T_o &= 0.005671003967685765 \text{ s} \\ PRF &= 486.4863102995529 \text{ Hz} \\ RSF &= 64,345,238.12571428 \text{ Hz} \end{aligned}$$

Accurate geolocation at the sub-pixel level requires a measured azimuth time that is precisely corrected for the effect of Stop-Go-Approximation. In the case of Sentinel-1, only a bulk azimuth correction $\tau_{mid}/2$, referring to half the fast time of the center sub-swath (IW₂ or EW₃, respectively), is already subtracted during SAR focusing, but this bulk correction does not suffice for sub-pixel accuracy.

A straight forward way to refine the Stop-Go-Correction is to undo this bulk azimuth shift and to apply the exact correction value computed for the target's image coordinates. However, the annotated azimuth times are based on the starting edge of the pulse repetition interval depicted in Figure 6, and not on the true echo receive time of the single target. For this reason, the most convenient way to correct for the truly measured Zero-Doppler azimuth time is to go back from the annotated azimuth time to the instant of radar pulse transmission. This is performed by subtracting $rank \cdot PRI$, where *rank* means the number of traveling radar pulses, and *PRI* the duration of the pulse repetition interval; both values are readily available from the annotation of the Sentinel-1 image product. The structure of this XML document is explained in [58]. Subsequently, one adds half of the actually measured fast time (range), i.e. the $\tau_{m,CR}/2$, to end up at zero-Doppler azimuth of the target. The corresponding values for the given example are listed in Table 17, row 12 to 14.

Like the azimuth, the measured range time coordinate also has to be corrected in the case of Sentinel-1, because it still contains the Doppler effect discussed in section 2.5.3.2.3. There is just an indirect way to access the Doppler centroid in the focused burst because only the raw data Doppler centroid is annotated in the image product. The procedure to derive the focused Doppler centroid from the annotated parameters is described in [59]. There are two contribution, that are relevant for our computations: firstly the geometric Doppler contribution $f_{\eta c}$ from antenna orientation, which is given as polynomial referring to the center of each burst, and secondly the contribution from electronic antenna steering, characterized by the Doppler rate

$$k_t(\tau) = \frac{k_a(\tau) \cdot k_s}{k_a(\tau) - k_s} \quad \text{Eq. 41}$$

with k_a being the azimuth FM rate (also given as polynomial per burst), and k_s being the Doppler rate the electronic steering introduces to the raw data. The sum of both contribution yield the Doppler centroid

$$f_{DC,CR} = f_{\eta c} + k_t(\tau) \cdot (t_{CR,m} - t_{mid}) \quad \text{Eq. 42}$$

of the focused target, where t_{mid} denotes the burst center time. In our example, the procedure leads to an estimate of -1539.23 Hz for the Doppler centroid $f_{DC,CR}$ at the position of CR11. This Doppler centroid and the chirp rate K_r of the used chirp pulse (7.792817275120481e+11 Hz/s, taken from the annotation of the S1A image product) yield a range offset time

$$\Delta\tau = \frac{f_{DC,CR}}{K_r} \quad \text{Eq. 43}$$

In the example, it amounts to -0.00000001976 s and has to be corrected for. It corresponds to a range bias of -0.2962 m.

Furthermore, the measured range has to be corrected for the signal propagation delays, as there are: tropospheric delay: 2.8784 m (0.00000019203 s); ionospheric delay 0.0820 m (0.00000000547 s). Note, that the signal propagation delays have to be subtracted from the range measurement, thus the negative signs in Table 17.

In the last step, one computes the difference between the computed and the measured time, which results in an ALE of -0.063 m in range and 0.174 m in azimuth when applying the conversion to units of length, see Table 17 row 19 to 21.

Table 16: Sample calculation for the computation of the expected radar times (positions and offsets in m; velocities in m/s). Date and time of the computation are 2016-05-11 08:32:52 UTC.

Row	Parameter	X	Y	Z	Description
1	CR position at epoch 2016.361 in ITRF2008	-4979009.3977	2766786.0807	-2860862.7193	section 2.7.1.2.6 & TN100
2	solid Earth tides	0.0250	0.0075	0.0444	section 2.7.1.1
3	ocean loading	-0.0047	0.0045	-0.0046	section 2.7.1.2.1
4	atmospheric tidal loading	-0.0003	-0.0000	-0.0002	section 2.7.1.2.2
5	pole tides	-0.0007	-0.0004	-0.0003	section 2.7.1.2.3
6	ocean pole tide loading	0.0002	0.0002	0.0002	section 2.7.1.2.4
7	CR position	-4979009.3782	2766786.0925	-2860862.6798	Σ of rows 1 to 6
8	satellite position at zero-Doppler	-5215175.4690	3480679.1546	-3288500.3987	section 2.7.3
9	satellite velocity at zero-Doppler	-1933.5554	3289.3163	6559.0019	section 2.7.3

Table 17: Sample calculation for the determination of the ALE. Range related times are given as two-way round trip times.

Row	Parameter	Azimuth	Range	Description
10	computed radar times	2016-05-11T 08:32:52.260818744 UTC => 30772.260818744 s of day	0.005770916226 s	section 2.7.4
11	measured radar times	2016-05-11T 08:32:52.260504997 UTC => 30772.260504997 s of day	0.005770939113 s	section 2.5.5
12	removal of bulk azimuth correction	0.002930633 s		+ $T_{mid}/2$
13	shift to pulse transmit time	-0.005511057 s		- $rank \cdot PRI$
14	correction for satellite motion	0.002885470 s		+ $T_{m,CR}/2$
15	range correction w.r.t. Doppler		-0.000000001976 s	+ FDC_{CR}/FM_{chirp}
16	correction for tropospheric delay		-0.000000019203 s	section 2.6.1.1 (ECMWF)
17	correction for ionospheric delay		-0.000000000547 s	section 2.6.2 (CODE)
18	measured radar times (corrected)	30772.260810043 s of day	0.005770917387 s	Σ of rows 11 to 17
19	ALE in s	-0.000008701 s	0.000000001161 s	row 18 – row 10
20	conversion factor	$V_{FDC0}=6842.9409$ m/s	$c/2=149896229$ m/s	
21	ALE in m	-0.0595 m	0.1740 m	row 19 · row 20

List of Figures

Figure 1: Brief sketch of measurement arrangement and procedures.....14

Figure 2: Flow chart of the protocol described in this note. Documents *TN100 and *TN200 refer to [RD1] and this document, respectively.15

Figure 3: SAR acquisition geometry. The distance $r = r$ between sensor and target is minimum at $t=t_0$. At this instant, the range vector r is perpendicular to the flight path.18

Figure 4: Range history, i.e. temporal progression of the distance between sensor and target during data take acquisition. Plotted for three targets: at near, mid and far range (schematic diagram).19

Figure 5: Information on the location of a point scatterer, derivable from radar coordinates. a: Azimuth defines the zero Doppler plane. b: Range defines the surface of a sphere centered on the sensor. c: The intersection of both surfaces results in a circle line which is perpendicularly oriented to the satellite’s flight path in space.20

Figure 6: A SAR instrument registers radar echoes as a function of time t . The offset k indicates the number of travelling pulses accounting for the fact, that the signal round trip delay is larger than a pulse repetition interval.....24

Figure 7: The plot on the left depicts the true timing of the received SAR echo sample matrix, while the plot on the right illustrates the timing as it is assumed by the Stop-Go-Approximation. This mismatch directly affects the time coordinates of the final SAR image.25

Figure 8: Schematic sketch of the TerraSAR-X imaging modes Stripmap, Spotlight and ScanSAR [9].27

Figure 9: Impact of the difference between center of mass (red) and a geometrical SAR antenna reference (blue) on range observations. The effect is shown for the Sentinel-1 spacecraft having an average roll steering of 29.5° and the near range to far range coverage for the IW TOPS of 25° to 42° 29

Figure 10: Satellite motion from pulse transmission until echo reception (non-scale schematic diagram). While the radar signal is traveling, the satellite moves from position P1 (at instant of pulse transmission) via position P2 (at instant of pulse reflection on ground) to position P3 (at instant of echo reception).34

Figure 11: Satellite motion during echo reception (non-scale schematic diagram). There are two CRs: One in near range and one in far range. Both CRs reflect the radar pulse at different times and also the instants of echo reception differ. Consequently, the satellite is at different positions: P₂ while pulse reflection by near range CR₁, P₃ while pulse reflection by far range CR₂, P₄ and P₅ while receiving the respective echoes.35

Figure 12: Satellite motion while pulse duration (non-scale schematic diagram). The satellite moves from P₁ to P₂ while transmitting the pulse. Consequently, there is an approximately equal motion (from P₆ to P₇) while receiving the echo. P₃, P₄ and P₅ denote the satellite positions at the instants when leading edge (P₃), center (P₄) and trailing edge (P₅) of the radar pulse are reflected on ground. The orbit segments the satellite passes during pulse transmission (segment P₁–P₂), pulse reflection (segment P₃–P₅) and echo reception (segment P₆–P₇) are highlighted by thick lines.36

Figure 13: Increase of signal travel distance (non-scale schematic diagram). According to Pythagorean Theorem, the distance covered by a pulse, transmitted half of the signal travel time before closest approach, amounts to approximately $r \cdot 1 + v^2c^2$ where r means the distance between sensor and target at closest approach, v the speed of the satellite and c the light velocity. The analogous geometric considerations are true for the echo received half of the signal travel time after the closest approach.37

Figure 14: Schematic diagram of the proposed two-stage method [44]40

Figure 15: Estimation of measurement resolution of the proposed two-stage method. Chosen oversampling factor in the first stage (x axis) versus offset of measured peak position relative to a two-stage measurement result for an oversampling factor of 512 (y axis). The measurement results differ by less than 1/10000 pixel. A comparison against pure oversampling of comparable resolution is inapplicable due to resource constraints [44].42

Figure 16: Size and arrangement of the measurement patches for the characteristics of clutter (dark grey), sidelobes (light grey) and mainlobe (white). The peak position of the CR defines the center of the mainlobe area. Sidelobe areas and the measurement patches for the clutter power are arranged around the mainlobe. ρ_{az} and ρ_{rg} refer to the 3 dB width in azimuth and range, respectively.43

Figure 17: Examples for the global grids (2° x 2.5°) of hydrostatic (left) and wet (right) path delays distributed with the VMF₁.52

Figure 18: Global IGS station network (red) and regional EUREF network (blue) for which tropospheric path delays are routinely processed. Global view (left) and regional zoom (right).55

Figure 19: Tropospheric zenith path delay products of 2016-06-26 for two GNSS receivers (WTZR, WTZS) located at Wettzell geodetic observatory. Total tropospheric path delay (top) and gradient components (bottom). The products are provided by the International GNSS Service (IGS), the Centre of Orbit Determination in Europe (CODE), and the European reference GNSS network EUREF, and the Vienna Mapping Function 1 (no gradients, only the ZPD).59

Figure 20: Concept of the ionospheric mapping function assuming a single layer ionospheric model.60

Figure 21: Global vTEC distribution based on the CODE global ionospheric map product for the 1st of June 2017. vTEC map (left) and corresponding RMS map (right).63

Figure 22: Computational scheme of the solid Earth tides following the descriptions given in the IERS conventions 2010 [8]. 68

Figure 23: Global solid Earth tide displacement at 18:00 UTC in North (top), East (mid) and up (bottom) for the full Moon constellation on 2017-06-09 (left) and the half Moon constellation 2017-06-17 (right). 69

Figure 24: Vertical displacement signal for the ocean loading (a), the pole tides (b), the atmospheric tidal loading (c) and the ocean pole tide loading (d) for the day 2017-06-09 at 18:00 UTC. 72

Figure 25: ITRF2014 GNSS velocity field from the IGS14 solution. Horizontal field (top) and vertical field (bottom). The plate boundaries are from the tectonic model MORVEL56 [40].74

Figure 26: Outlier elimination by applying a 2 sigma test. The histograms show the data of the TerraSAR-X analysis of the corner reflector at Metsähovi observatory: Range (left), and azimuth (right).79

Figure 27: Absolute Location Error analysis and geometrical calibration of TerraSAR-X and TanDEM-X using the 1.5 m corner reflector of Metsähovi station (Finland). The corner reflector (a), raw result before outlier removal (b), result after outlier removal (c), and final result after applying the recalibration of Table 10(d).....82

Figure 28: Time sequential view of the TerraSAR-X and TanDEM-X ALE analysis (final result as shown in Figure 27d) for the 1.5 m corner reflector of Metsähovi station, Finland. Range result (top) and azimuth result (bottom). The two periods in range with improved short term consistency are marked in blue. 84

Figure 29: Overview on Sentinel-1 processor version (Instrument Process Facility, IPF) for the Wettzell dataset. The update in the Sampling Window Start Time (SWST) on March 5th has to be considered in products generated by the IPF before this date [51].85

Figure 30: Time sequential view of the Sentinel1A/B ALE result for the IW data of the Wettzell 1.5m descending CR. Δ Azimuth [m] in blue, Δ Range [1-way, m] in red. 87

Figure 31: ALE result of Sentinel-1A (left) and Sentinel-1B (right) for the IW TOPS data of the 1.5 m CR located at Wettzell, Germany.....88

Figure 32: S-1 ALE for IW-SLC products covering the CR array in Queensland, Australia 90

Figure 33: TerraSAR-X and TanDEM-X result of Wettzell 1.5 m CR. Corrections have been added step by step. 92

Figure 34: TSX ALE for two subsets of the CR array in Australia captured with Stripmap data. Result without the mount model for the CR phase center (top) and result after applying the model (bottom). Note the change in the scope of the axes.95

Figure 35: Definition of a local Cartesian reference frame for the ITRF position X using the WGS-84 ellipsoid (a, b) as a proxy for the Earth’s surface geometry. The direction to a satellite in the local frame is given by azimuth and elevation (A, E).97

List of Tables

Table 1: Approximate amounts of satellite motion effects for Sentinel-1 and TerraSAR-X. The exact amount depends on parameters like imaging mode and acquisition geometry. Thus, the table gives just a coarse orientation on the effects' order of magnitude. Values in braces refer to effects, the operational SAR processor (IPF for Sentinel-1 data or TMSP for TerraSAR-X data) already compensates for..... 33

Table 2: Meta-information extracted as byproduct during PTA..... 44

Table 3: Comparison of a simple $1/\cosine$ mapping function with the VMF1 across a typical full performance swath of a generic SAR payload (25° to 55° incidence angle). The VMF1 was evaluated for the Wettzell geodetic observatory (latitude = $49^\circ 08' 42''$, longitude = $12^\circ 52' 33''$, h = 659m) at 06UTC using the product *VMFG_20160101.H06*. To compute the slant delays in meters, a hydrostatic ZPD of 2.2 m and a wet ZPD of 0.2 m have been assumed.54

Table 4: Summary on the GNSS-based tropospheric path delay products provided by the International GNSS Service (IGS), the Centre of Orbit Determination in Europe (CODE) and the EUREF Analysis Centers (ACs). The details are given in [22][23][24].56

Table 5: Ionospheric path delay in meters for the different SAR bands assuming typical swath coverage and a vTEC of 20 TECU. The single layer mapping (SLM) function (Eq. 22) was evaluated for an Earth radius $R = 6378$ km and a shell radius of $R + H = 6821$ km, i.e. the single layer model radius used by CODE to generate the GIMs..... 62

Table 6: Approximate scaling factors for the ionospheric path delay considering the orbit altitude of different SAR missions 64

Table 7: Magnitude of the solid Earth displacement effects based on the geodynamic models listed in the IERS conventions 2010 [8]. The non-tidal atmosphere and the secular trends are not part of the conventions; see the discussion in the text..... 66

Table 8: Excerpt of the tabulated input for the TerraSAR-X ALE analysis in Metsähovi, Finland. SoD refers to seconds of day.....78

Table 9: Absolute Location Error: comparison of observed and predicted SAR timings and conversion to units of meters for the data shown in Table 8.....78

Table 10: Updated geometrical calibration constants for TerraSAR-X and TanDEM-X. The values have been derived from the ALE analysis of the 1.5 m corner reflector located at Metsähovi geodetic

observatory. Conversion to meters is given by vacuum light velocity (range) and the TSX orbit velocity of 7683 m/s (azimuth).81

Table 11: ALE results for the Sentinel-1A/B IW data of the 1.5 m CR located at Wettzell, Germany. The beams refer to the clusters shown in Figure 31. N is the number of observations.88

Table 12: Impact of the individual corrections when using a geometrically calibrated SAR sensor. Example of TerraSAR-X using high resolution spotlight data of the Wettzell 1.5 m CR. Starting from the calibrated raw data, the path delays and the different geodynamic effects are included step by step. In the last step, outliers are removed by the 2 sigma test.....93

Table 13: Comparison of different methods to correct the tropospheric path delay at the different test sites used by TUM/DLR for TSX and TDX ALE analysis. Δ Range mean and standard deviation [1-way, in cm]. 94

Table 14: ALE results for the TerraSAR-X Stripmap data for the 11 CRs of the GA reflector array (Queensland, Australia) which are covered by the Stripmap data set. The CR id (first column) corresponds to the list published by GA [12]...... 96

Table 15: Dimension parameters of the WGS-84 ellipsoid [32]97

Table 16: Sample calculation for the computation of the expected radar times..... 103

Table 17: Sample calculation for the determination of the ALE 103

References

- [1] ESA ERS-1 Product Specification SP-1149 GENo3, 1992.
- [2] Aulard-Macler M., *Sentinel-1 Product Definition*, MDA Technical Note, Ref. S1-RS-MDA-52-7440, MacDonald, Dettwiler and Associates (MDA), Richmond, BC, Canada, 2012, 126p.
- [3] Eineder M., Minet C., Steigenberger P., Cong X.Y., and Fritz T., *Imaging Geodesy - Toward Centimeter-Level Ranging Accuracy With TerraSAR-X*, IEEE Transactions on Geoscience and Remote Sensing, vol. 49, no. 2, pp. 661–671, Feb. 2011.
- [4] Cong X.Y., Balss U., Eineder M., and Fritz T., *Imaging Geodesy - Centimeter-Level Ranging Accuracy With TerraSAR-X: An Update*, IEEE Geoscience and Remote Sensing Letters, vol. 9, no. 5, pp. 948–952, Sep. 2012.
- [5] Schubert A., Small D., Jehle M., Meier E., *COSMO-skymed, TerraSAR-X, and RADARSAT-2 geolocation accuracy after compensation for earth-system effects*, 2012 IEEE International Geoscience and Remote Sensing Symposium, Munich, 2012, pp. 3301-3304.
- [6] Gisinger C., Balss U., Pail R., Zhu X.X., Montazeri S., Gernhardt S., Eineder M., *Precise Three-Dimensional Stereo Localization of Corner Reflectors and Persistent Scatterers with TerraSAR-X*, IEEE Transactions on Geoscience and Remote Sensing, vol. 53, no. 4, pp. 1782–1802, Apr. 2015.
- [7] Cumming I.G., Wong F.H., *Digital Processing of Synthetic Aperture Radar Data*, Artech House, Norwood, MA.
- [8] Petit G., Luzum B. (eds.), IERS Conventions (2010), IERS Technical Note No. 36, Verlag des Bundesamtes für Kartographie und Geodäsie, Frankfurt am Main, 2010. Online <https://www.iers.org/IERS/EN/Publications/TechnicalNotes/TechnicalNotes.html>
- [9] Fritz T., Eineder M., TerraSAR-X Ground Segment Basic Product Specification Document, technical note by the German Aerospace Center (DLR), Ref. TX-GS-DD-3302, Iss. 1.9, 2013.10.09, 2013. Online: <http://sss.terrasar-x.dlr.de>.
- [10] Bamler R, Eineder M, Accuracy of Differential Shift Estimation by Correlation and Split-Bandwidth Interferometry for Wideband and Delta-k SAR Systems. Geoscience and Remote Sensing Letters, 2005, vol. 2, pp. 151-155.
- [11] Garthwaite M.C., Nancarrow S., Hislop A., Thankappan M., Dawson J.H., Lawrie S., *The Design of Radar Corner Reflectors for the Australian Geophysical Observing System*, Australian Government / Geoscience Australia, Record 2015/03 | GeoCat 82751, 2015.
- [12] Garthwaite M.C., Hazelwood M., Nancarrow S., Hislop A., Dawson J.H., *A regional geodetic network to monitor ground surface response to resource extraction in the northern Surat Basin, Queensland, Aust. J. Earth Sci.* 1–9, 2015. doi: 10.1080/08120099.2015.1040073
- [13] Hofmann-Wellenhof B., Lichtenegger H., Wasle E., *GNSS Global Navigation Satellite Systems*, Springer-Verlag Wien, 2008.
- [14] Hopfield H.S., *Two-Quartic Tropospheric Refractivity Profile for Correcting Satellite Data*, Journal of Geophysical Research, 74 (18), 4487-4499, 1969. doi: 10.1029/JC074i018p04487
- [15] Dach R., Lutz S., Walser P., Fridez P. (eds.), *Bernese GNSS Software Version 5.2*, University of Bern, Bern Open Publishing, 2015. doi: 10.7892/boris.72297

- [16] Hanssen R., *Radar Interferometry: Data Interpretation and Error Analysis*. Kluwer Acad. Publ., Dordrecht 2001, ISBN 0-7923-6945-9
- [17] Dee D. P., Uppala S. M., Simmons A. J., Berrisford P., Poli P., Kobayashi S., Andrae U., Balmaseda M. A., Balsamo G., Bauer P., Bechtold P., Beljaars A. C. M., van de Berg L., Bidlot J., Bormann N., Delsol C., Dragani R., Fuentes M., Geer A. J., Haimberger L., Healy S. B., Hersbach H., Hólm E. V., Isaksen I., Kållberg P., Köhler M., Matricardi M., McNally A. P., Monge-Sanz B. M., Morcrette J.-J., Park B.-K., Peubey C., de Rosnay P., Tavolato C., Thépaut J.-N., Vitart, F. (2011), *The ERA-Interim reanalysis: configuration and performance of the data assimilation system*. Q.J.R. Meteorol. Soc., 137: 553–597. doi:10.1002/qj.828
- [18] Cong X.Y., Bals U., Suchandt S., Eineder M., Runge H., *SAR absolute ranging - Validation and application of SAR geodesy processor using ECMWF reanalysis and operational data*, 2016 IEEE International Geoscience and Remote Sensing Symposium (IGARSS), Beijing, 2016, pp. 3246-3249.
- [19] Böhm J., Werl B., Schuh H., *Troposphere mapping functions for GPS and VLBI from ECMWF operational analysis data*, Journal of Geophysical Research, 111, 2006. doi: 10.1029/2005JB003629
- [20] Marini J.W., *Correction of satellite tracking data for an arbitrary tropospheric profile*, Radio Science, 7(2), 223-231, 1972.
- [21] Kouba J., *Implementing and testing of the gridded Vienna Mapping Function₁ (VMF₁)*, Journal of Geodesy, 82, 193-205, 2008.
- [22] Byram S., Hackman C., Tracey J., *Computation of a High-Precision GPS-Based Troposphere Product by the USNO*, Proceedings of the 24th International Technical Meeting of the Satellite Division of The Institute of Navigation, 572-578, 2011.
- [23] Schaer S., Dach R., Arnold D., Prange L., Sidorov D., Susnik A., Villiger A., *International GNSS Service CODE Analysis Strategy Summary*, Technical note by Center of Orbit Determination in Europe, 2017. Online: ftp://ftp.unibe.ch/aiub/CODE/0000_CODE.ACN
- [24] Pacione R., Araszkiwicz A., Brockmann E., Dousa J., *EPN-Repro2: A reference GNSS tropospheric data set over Europe*, Journal of Geodesy, 82, 193-205, 2008.
- [25] Lagler K., Schindelegger M., Böhm J., Krásná H., Nilsson T., *GPT2: Empirical slant delay model for radio space geodetic techniques*, Geophysical Research Letters, 40, 1069-1073, 2013. doi: 10.1002/grl.50288
- [26] Saastamoinen J., *Contributions to the theory of atmospheric refraction Part II*, in Refraction corrections in satellite geodesy, Bulletin Géodésique, 107(1), 13-34, 1973.
- [27] Troller M., *GPS based Determination of the Integrated and Spatially Distributed Water Vapor in the Troposphere*, in: Geodätisch-geophysikalische Arbeiten in der Schweiz, vol. 67, 2004.
- [28] MacMillan D.S., *Atmospheric gradients and the VLBI terrestrial and celestial reference frames*, Geophysical Research Letters, 24(4), 453-456, 1997.
- [29] Hernández-Pajares M., Juan J.M., Sanz J., Orus R., Garcia-Rigo A., Feltens J., Komjathy A., Schaer S.C., Krankowski A., *The IGS VTEC maps: a reliable source of ionospheric information since 1998*, Journal of Geodesy, 83, 263-275, 2009. doi: 10.1007/s00190-008-0266-1

- [30] Schaer S., *Mapping and Predicting the Earth's Ionosphere Using the Global Positioning System*, in: Geodätisch-geophysikalische Arbeiten in der Schweiz, vol. 59, 1999.
- [31] Balss U., Cong X.Y., Brcic, R., Rexer M., Minet C., Breit H., Eineder M., Fritz T., *High precision measurement on the absolute localization accuracy of TerraSAR-X*, Geoscience and Remote Sensing Symposium (IGARSS), 2012 IEEE International, 2991-2994, 2012. doi: 10.1109/IGARSS.2012.6351217
- [32] NIMA, *Department of Defense World Geodetic System 1984*, National Imagery and Mapping Agency Technical Report, Third Edition, NIMA TR8350.2, 2000.
- [33] Altamimi Z., Rebischung P., Métivier L., Collilieux X., *Analysis and results of the ITRF2014*, IERS Technical Note No. 38, Verlag des Bundesamtes für Kartographie und Geodäsie, Frankfurt am Main, 2017. Online: <https://www.iers.org/iers/en/publications/technicalnotes/technicalnotes.html>
- [34] Fey A.L., Gordon D., Jacobs C.S. (eds.), *The Second Realization of the International Celestial Reference Frame by Very Long Baseline Interferometry*, IERS Technical Note No. 35, Verlag des Bundesamtes für Kartographie und Geodäsie, Frankfurt am Main, 2009. Online: <https://www.iers.org/iers/en/publications/technicalnotes/technicalnotes.html>
- [35] Hackel S., Montenbruck O., Steigenberger P., Balss U., Gisinger C., Eineder M., *Model Improvements and Validation of TerraSAR-X Precise Orbit Determination*, Journal of Geodesy, 91(5), 547-562, 2017. doi: 10.1007/s00190-016-0982-x
- [36] Peter H., Jäggi A., Fernández J., Escobar E., Ayuga F., Arnold D., Wermuth M., Hackel S., Otten M., Simons W. Visser P. Hugentobler U., Féménias P., *Sentinel-1A – First precise orbit determination results*, Advances in Space Research, Online First, 2017. doi: <http://dx.doi.org/10.1016/j.asr.2017.05.034>
- [37] Milbert D., *Solid earth tide*, FORTRAN computer program, 2011. Online: <http://geodesyworld.github.io/SOFTS/solid.htm>
- [38] Petrov L., Boy J.P. *Study of atmospheric pressure loading signals in very long baseline interferometry observations*, Journal of Geophysical Research, 109, 2004. doi: 10.1029/2003JB002500
- [39] Lyard F., Lefevre F., Letellier T., Francis O., *Modelling the global ocean tides: modern insights from FES2004*, Ocean Dynamics, 56, 394-415, 2006. doi: 10.1007/s10236-006-0086-x
- [40] Argus D.F., Gordon R.G., DeMets C., *Geologically current motion of 56 plates relative to the no-net-rotation reference frame*, Geochemistry Geophysics Geosystems, 12(11), 2011. doi: 10.1029/2011GC003751
- [41] Schubert A., Small D., *Extended Sentinel-1 product annotations supporting enhanced accuracy geolocation*, UZH-S1-APD-TN03, Issue 1.01, Feb. 15, 2016, 51p.
- [42] Balss U., Breit H., Fritz T., Steinbrecher U., Gisinger C., Eineder M., *Analysis of Internal Timings and Clock Rates of TerraSAR-X*, Proceedings of IEEE International Geoscience and Remote Sensing Symposium, pp. 2671–2674, Québec, Canada 2014.
- [43] Stein S., *Algorithms for Ambiguity Function Processing*, IEEE Transactions on Acoustics, Speech and Signal Processing, vol. ASSP-29, no. 3, 1981.

- [44] Balss U., Cong X.Y., Brcic R., Rexer M., Minet C., Breit H., Eineder M., Fritz T., *High Precision Measurements on the Absolute Localization Accuracy of TerraSAR-X*, Proceedings of IEEE International Geoscience and Remote Sensing Symposium, pp. 1625–1628, Munich, Germany 2012.
- [45] Meadows P.J., *Point Target Analysis Algorithm Definition & Detailed Design Document*, ESA Ref. Doc. SARCON-DD-MRC–1003-02, Issue 1.5, 2002.
- [46] Fritz T., Mittermayer J., Schättler B., Balzer W., Buckreuß S., Werninghaus R., *TerraSAR-X ground segment level 1b product format specification*, technical note by the German Aerospace Center (DLR), Ref. TX-GS-DD-3307, Iss. 1.3, 2007.10.12, 2007. Online: <http://sss.terrasar-x.dlr.de>.
- [47] Böhm J., Schuh H. (eds.), *Atmospheric Effects in Space Geodesy*, Springer-Verlag Berlin Heidelberg, 2013. doi: 10.1007/978-3-642-36932-2
- [48] Bourbigot M., Johnsen H., Piantanida R., *Sentinel-1 Product Definition, Technical note by Sentinel-1 Mission Performance Center (MPC)*, Document S1-RS-MDA-52-7440, Issue 2, Revision 6, Date 22.07.2015, 2015.
- [49] Schubert A., Small D., Miranda N., Geudtner D., Meier E., *Sentinel-1A Product Geolocation Accuracy: Commissioning Phase Result*, Remote Sensing, vol. 7, no. 7, pp. 9431–9449, 2015. doi: 10.3390/rs70709431
- [50] Schubert A., Miranda N., Geudtner D., Small D., *Sentinel-1A/B Combined Product Geolocation Accuracy*, Remote Sensing, vol. 9, no. 6, pp. 1–16, 2017. doi: 10.3390/rs9060607
- [51] Schubert A., Small D., Miranda N., Geudtner D., Meier E., *Sentinel-1A Product Geolocation Accuracy: Beyond the Calibration Phase*, Proceedings of CEOS WGCV workshop, Noordwijk, Netherlands, 2015. Online: <http://sarvc.ceos.org/documents/doc/152/>
- [52] Rodriguez-Cassola M., Prats-Iraola P., De Zan F., Scheiber R., Reigber A., Geudtner D., Moreira A., *Doppler-Related Distortions in TOPS SAR Images*, IEEE Transactions on Geoscience and Remote Sensing, vol. 53, no. 1, 2015. doi: 10.1109/TGRS.2014.2313068.
- [53] Kahle, R., *TerraSAR-X / TanDEM-X Mission Operations Segment Orbit and Attitude Product Specification*, technical note by the German Aerospace Center (DLR), Ref. TX-GS-SP-2601, Iss. 3.4, 2012.11.06, 2012.
- [54] Mathews P. M., Buffet B.A., Shapiro I. I., *Love numbers for a rotating spheroidal Earth: New definitions and numerical values*, Geophysical Research Letters, vol. 22, no. 5, 1995. doi: 10.1029/95GL00161.
- [55] Schubert A., Jehle M., Small D., Meier E., *Mitigation of atmospheric perturbations and solid Earth movements in TerraSAR-X time-series*, Journal of Geodesy, vol. 86, no. 4, pp. 257-270, 2012. doi: 10.1007/s00190-011-0515-6
- [56] Panetti A., L'Abbate M., Bruno C., Bauleo A. et al., *Sentinel-1 Spacecraft*, Proceedings of EUSAR 2014, 10th European Conference on Synthetic Aperture Radar, 2014.
- [57] Geudtner D., Torres R., Snoeij P., Bibby D., Rommen B., *Sentinel-1 System*, Proceedings of EUSAR 2014, 10th European Conference on Synthetic Aperture Radar, 2014.

- [58] Bourbigot M., Johnsen H., Piantanida R., *Sentinel-1 Product Specification, Technical note by Sentinel-1 Mission Performance Center (MPC)*, Document S1-RS-MDA-52-7441, Issue 3, Revision 3, Date 14.10.2016, 2016.
- [59] Miranda, N. Definition of the TOPS SLC deramping function for products generated by the S-1 IPF, Document COPE-GSEG-EOPG-TN-14-0025, Issue 1, Revision 2, Date 20.04.2015.